# Modelling of electrode-plasma interactions in Pulsed Plasma Thrusters

by

YONIS LE GRAND

to obtain the degree of Master of Science
at the Delft University of Technology,
and the Eindhoven University of Technology,
to be defended publicly on Wednesday November 24, 2021 at 14:00.



| | | |
|---|---|---|
| STUDENT NUMBER: | 4081633 | |
| CHAIR: | DR. A. CERVONE | TU DELFT |
| SUPERVISOR | IR. B.T.C. ZANDBERGEN | TU DELFT |
| EXAMINER | IR. R. NOOMEN | TU DELFT |
| SUPERVISOR | DR. M. MERINO | UC3M |
| SUPERVISOR | DR. H.J. DE BLANK | TU EINDHOVEN |

# Summary

Electric propulsion generally has propellant saving benefits compared to traditional chemical propulsion. One type of electric propulsion is the Pulsed Plasma Thruster (PPT), which has been flight tested in the 60's and has the advantage of being easy to build and a high thrust to area density compared to other electric propulsion devices. An Ablation-fed PPT (A-PPT) consists of a solid Teflon propellant situated between two electrodes. At each pulse a spark runs between the electrodes. The propellant ablates and ionizes to form a plasma. The plasma forms a current bridge or arc between the electrodes. The current bridge accelerates outwards thanks to the Lorenz force provided by its self-induced field, thereby providing thrust. These devices are compact and produce micronewton level thrust with average exhaust velocities in the 5-12 km/s range. A drawback is that the PPT is characterised by low thrust efficiency (5-15%) compared to other electric propulsion devices[1][2].

Literature describes the plasma arc in a PPT as a thermal arc discharge. These are characterised by high electron densities and currents. There are three types of mechanisms with which electrodes release electrons into the plasma current bridge. The secondary electron emissions are electrons that are knocked out of the conductor by incoming ions. The thermionic electron emissions are electrons that are released due to electrode heating. The field electron emissions are electrons that tunnel through the Fermi barrier at high electric field. In a thermal arc discharge, the latter two dominate.

This project can be seen as an initial exploration of the arc discharge properties of a PPT. The modelling of the arc is presented in this thesis, with a focus on particle flow from cathode to anode and the electron emissions at the electrodes. This is dubbed the transverse model because it investigates the particle flux perpendicular to the outward propagating direction of the propellant. It consists of a set of equations for electron emission from the electrodes, charge continuity and momentum balance. The inputs are the physical dimensions of the thruster; propellant and electrode material properties; electrode potential, electron temperature and density. This code will also contain equations for the secondary, thermionic and field emissions, which had been lacking in previous PPT simulation efforts.

In the future, this model will be integrated within a Quasi-2D simulation code for the PPT. This code will couple the two models: an axial model that uses the method of characteristics to describe the bulk downstream motion of the plasma, and the transversal model that describes plasma wall interaction and the plasma current. Both codes will simulate the PPT plasma flow as a three fluid mixture of ions, electrons and neutrals.

A set of PPT experiments were identified as benchmarks for this study. These were thruster experiments that measured the electron density, temperature and magnetic field. Simulations results of the transverse model calculate current density and magnetic field levels that are in agreement with the literature benchmarks. The current density was mainly determined by electrical resistance and self-inductance. Plasma resistivity due to neutrals was deemed negligible. The maximum current density for electron temperature and density was identified. The effects of including thermionic emissions in the model were investigated. This added complexity to the model due to the non-linear nature of the Richardson equation. It was determined that the range of possible cathode temperatures was a function of electron current density. The main factors determining electron current density were the applied potential drop and the electron temperature. Thermal electrons diffusing from the bulk to both electrodes had the largest contribution to electron density. However thermionic emissions played a significant role by decreasing the cathode sheath potential drop.

# Contents

# List of Figures

# List of Tables

## Nomenclature

| | |
|---|---|
| $A$ | Surface area |
| $A_{xe}$ | Electron momentum transfer due to collisions |
| $a_{iz}$ | Ionization degree |
| $B$ | Magnetic field strength |
| $\mathbf{B}$ | Magnetic field vector |
| C | Capacitance |
| $c_{e0}$ | Electron thermal velocity |
| E | Electric field strength |
| $f$ [Hz] | Frequency |
| $f_i$ | probability distribution function of species $i$ |
| $f_1$ | User defined matlab function 1 |
| $g$, $\Gamma$ | particle flux |
| $h$ | Height |
| $I$ | Total current (per surface area) |
| i (t) | Current as a function of time |
| $j$ | Current density |
| $\mathbf{J}$ | Current density vector |
| $M$ | Mach number |
| $m$ | mass |
| L | Length |
| $L$ | Inductance |
| $L'$ | Inductance change per unit length |
| $n$ | Particle number density |
| $p$ | Pressure |
| $R$ | Resistance |
| $T$ | Temperature |
| $t$ | time |
| $u_B$ | Bohm velocity |
| $V$ | Potential drop in volts |
| $w$ | Width |
| W | Work Function |
| $x$ | Transverse direction coordinate |
| $z$ | Axial (downstream) coordinate |
| $Z$ | Ionization number |
| $\delta$ | Plasma Sheet thicnkess |
| $\gamma$ | Heat capacity ratio for an ideal gas |
| $\eta$ | resistivity |
| $\varepsilon_F$ | Fermi energy |
| $\varepsilon_i$ | Ionization energy |
| $\omega$ | Frequency in rad |
| $\lambda_D$ | Debye Length |
| $\varphi$ | Dimensionless electric potential |
| $\Phi$ | Voltage with respect to ground in Volts |
| $X$ | Dimensionless distance coordinate within sheath |
| $\Theta$ | Ratio between plasma electron temperature and electrode surface temperature |

## Sub- and Superscripts

| | |
|---|---|
| $\star$ | Emitted electrons |
| $+$ | Ionized |
| $++$ | Doubly ionized |
| $A$ | Anode (wall) |
| $B$ | Plasma sheath Edge near Anode, Bohm conditions |
| $b$ | Bulk (non-sheath) Plasma |
| $bolz$ | Boltzmann Transport Equation |
| $C$ | Cathode (wall) |
| $D$ | Plasma sheath Edge near Cathode |
| $e$ | electron |
| $i$ | ion |
| $n$ | neutron |
| $p$ | proton, Planck, Plasma |
| $p/se$ | Pre-sheath to sheath boundary |
| $se$ | Sheath edge |
| $tot$ | total |
| $W$ | Pertaining to the electrode wall |
| $x$ | Transverse coordinate |
| $y$ | Out of plane axis (perpendicular to $x$ and $z$) |
| $z$ | Axial coordinate |

## Acronyms

| | |
|---|---|
| APPT | Ablation-fed Pulsed Plasma Thruster |
| CFD | Computational Fluid Dynamics |
| CSCX | Current Sheet Canting Experiment |
| DIFFER | Dutch Institute For Fundamental Energy Research |
| EoS | Equation of State |
| emf | Electron-motive force |
| FEE | Field Electron Emissions |
| FWHM | Full-Width Half Maximum |
| GPPT | Gas-fed Pulsed Plasma Thruster |
| GTAW | Gas Tungsten Arc Welding |
| MHD | Magneto Hydrodynamics |
| MPDT | Magneto-Plasma-Dynamic Thruster |
| NASA | National Aeronautics and Space Administration |
| NRL | Naval Research Lab |
| PPT | Pulsed Plasma Thruster |
| SCL | Space Charge Limited (sheath) |
| SEE | Sheath Electron Emissions |
| TEE | Thermionic Electron Emissions |

# Physical Constants

| Quantity | Symbol | Value |
|---|---|---|
| Boltzmann constant | $k$ | $1.380{\cdot}10^{-23}$ J/K |
| Elementary charge | $e$ | $1.602{\cdot}10^{-19}$ C |
| Electron mass | $m_e$ | $9.109{\cdot}10^{-31}$ kg |
| Proton mass | $m_p$ | $1.673{\cdot}10^{-27}$ kg |
| Permeability of free space | $\mu_0$ | $1.256{\cdot}10^{-6}$ H/m |
| Permittivity of free space | $\varepsilon_0$ | $8.854{\cdot}10^{-12}$ F/m |
| Planck's constant | $h_p$ | $6.626 \cdot 10^{-34}$ J·s |
| Reduced Planck's constant | $\hbar$ | $1.054 \cdot 10^{-34}$ J·s |
| Temperature associated with 1 eV | | 11605 K |
| Energy associated with 1 eV | | $1.602{\cdot}10^{-19}$J |

Table 1: Adapted from Liebermann [5]

# 1 Introduction

Given the advent of small satellites, electric propulsion is a sought after technology that has propellant saving benefits. Traditionally, most rockets that are used for launching satellites and orbital transfer manoeuvres draw chemical energy from the combustion of propellant fuels. These chemically powered rockets are known to be large devices that generally carry multiple times more propellant than payload. These engines have a theoretical upper limit to their specific impulse (Isp) of around 500s. Alternatively electric propulsion devices can achieve significantly higher Isp's by accelerating a charged fluid, or plasma, using an electrical and or magnetic field. Unlike chemical rockets whose propellants serve as an internal power source, these devices need an external power source (e.g. Solar panels or radio-thermal isotope generators). Their power levels are thus limited to the available power of the satellites' power plant. On the other hand, increasing Isp leads to an exponential decrease of the required propellant mass to achieve a velocity change[23]. Electric propulsion allows substantial propellant mass savings in low thrust space based applications, such as orbital manoeuvres and drag compensation. This category of propulsion has therefore spawned a large variety of design types, such as electrostatic thrusters, Hall effect thrusters and Lorentz-force thrusters. [1][2][24].

Most electric propulsion mechanisms involve some form of charge separation, or require a neutralizer to maintain charge balance in the plasma, which limits the thrust/area density. Lorentz-force thrusters, such as the Magneto-plasma dynamic thruster (MPDT), do not have this issue. MPDTs have high power requirements (100-500kW) which are often not available on satellites [25]. The portion of the voltage that is responsible for thrust, the back-electromotive-force (emf), scales with the cube of the current ($V_{emf} \propto I^3$)[25][26]. At lower current levels ohmic losses ($V_\Omega \propto I$[5]) and the sheath potential drop (can be in the range of 100-300 V[5, p. 488]) dominate the thruster voltage[26][2]. This is why the normal operation is in the kV and KA range.

To mitigate the limitations on available power for satellites, it can be opted to design a MPDT-like advice that operates in pulses. This is called a Pulsed Plasma Thruster (PPT). It stores its energy in a capacitor, to unleash this energy into the propellant for microsecond bursts at a rate of (0.5-2 Hz)[1]. These devices are easy to build and miniaturise. They therefore have an extensive experimental and operational mission history[1][27]. On the other hand, these devices are difficult to model because of their transient and unsteady nature of operation. Modelling efforts have been diverse[1][28], but often using simplifying assumptions (such as steady state approximations) and focusing on certain aspects of flow[29][29][30]. As a result, the details of plasma flow and interaction between the physical processes are still not fully understood. One particular issue is the low thrust efficiency (5%-15%)[1][2]. A better understanding of how the physics affect the performance can potentially enhance the design optimization of PPTs. One particular aspect that has received little attention is the effects of electron emission mechanisms on PPT performance. These were taken into account under simplifications in 3D Particle in Cell modelling by Neudorfer et al [31]. In the current study a more detailed approach will be taken to the modelling of electron emission mechanisms.

## 1.1 Project Context

The aerospace department of Univesidad Carlos III de Madrid (U3CM) has an ongoing design project for micro-sattelites[32]. Such Micro-satellites, with masses in the order of 10 kg, provide opportunities for reduced total project costs. Plasma Propulsion is a popular contender for application on micro-thrusters. The Plasma and Space Propulsion team (EP2) of U3CM has research lines on various electro-magnetic thrusters. For an upcoming CubeSat project, EP2 has chosen to develop a PPT which operates in the electromagnetic as well as the electrothermal regime. The benefit of a PPT compared to other electric propulsions system is that it is compact, lightweight and robust[1]. Historically, it has taken less time from development to application in space missions than other thrust devices, due to its simplicity[1]. On the other hand, PPTs are less efficient than other electric propulsion devices[2].

This thesis project forms part of a larger Pulsed Plasma Thruster research and design effort. Simulation codes exist to simulate two-fluid flows (ions and electrons) in the much larger Magnetoplasmadynamic thruster (MPDT)[33][34][35][36]. For PPTs some CFD Modelling has been done[1][29][37], but the emphasis has been on placed on improving heuristic models [38][17] originally developed by Jahn[9]. EP2 requires a 2D time marching code to study the evolutions of the transient discharges in PPTs. To simulate this a fluid model code is coupled with a circuit model code. While previous models generally have modeled the plasma resistance as a constant, this project deals with the plasma portion of the electrical circuit and its interaction with the electrode material (plasma-wall interaction).

The aerospace department of the TU Delft also has ongoing research projects on micro-thrusters for micro-satellites. It's research is mainly focused on electrothermal thrusters, but there is interest for other electrical propulsion concepts. TU Eindhoven has a research group for nuclear fusion and plasma propulsion. In cooperation with the Dutch Institute For Fundamental Energy (DIFFER), the TU Eindhoven researches plasma wall interaction within a tokamak using an experimental linear accelerator called Magnum PSI[39]. Plasma thrusters are essentially considered linear accelerators as well[9]. In certain regions of a fusion reactor the plasma may display similar characteristics to a PPT plasma. U3CM is also involved in a synergistic project, PROMETEO, with the Spanish national fusion laboratory, CIEMAT, for research on common challenges between fusion and plasma propulsion.[2] Two particularly relevant objectives of PROMETEO is the research of plasma-wall interactions, as well as developing a simulation platforms capable of simulating different plasma thruster designs[40]. These provide an interesting synergy between fusion and plasma propulsion research that will be explored in this project.

## 1.2 Pulsed Plasma Thruster

Pulsed Plasma Thrusters come in different geometric configurations and use different types of propellant, but the method of operation is based on the same principles. The PPT is driven by an inductance-resistance-Capacitance (LRC) circuit. At each pulse an electric spark is ignited between two parallel electrodes and ionizes propellant. A plasma forms a current bridge between the electrodes, closing the circuit[1]. The plasma sheet is propelled due to the Lorentz force of the magnetic field that is enclosed by this circuit as can be seen in figure 1[3].

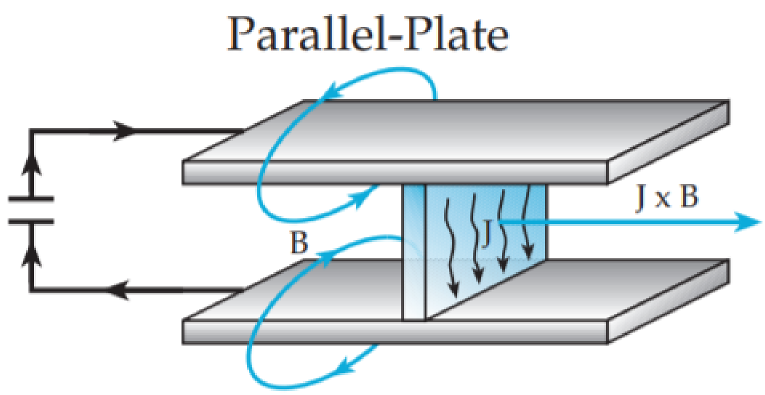


Figure 1: Parallel Plate Geometry PPT. The current sheet formed between the electrode plates is repulsed by the magnetic field **B** of the returning current. The current density vector is represented by **J**.[3]

The most common type is the Ablation fed Pulsed Plasma Thruster (APPT). This thruster uses solid Teflon as a propellant. At each pulse a portion of the Teflon block is ablated. These devices have been implemented in space flight missions since the 60's due to ease of construction. The physics of operation is quite complicated. During the initiation of the discharges a high electric field in the range of 10-100 kV/cm appears between the electrodes [1]. A spark plug between the electrodes introduces an initial amount of electrons into the channel which cause a minor discharge with a far smaller current than the main discharge. As the current density grows, the propellant material at the surface exposed to the hot arc starts to evaporate and ionize, creating a plasma. The discharge then rapidly develops to an arc plasma [1]. The plasma is a diffuse bulk which stretches along the electrodes[41, 42]. The current density is highest upstream during the whole discharge[4].

The ionized particles accelerate outward due to the Lorentz force and achieve speeds in the range of 15-50 km/s. At first the plasma is fully ionized, but towards the end of the pulse, material evaporates that does

[2]PROMETEO project

not fully ionize. A portion of the plasma accelerates electrothermally[3] and reaches speeds (3-8 km/s). The kinetic energy of the ions at these speeds corresponds to the stagnation temperature of the electrons (1-3 eV)[4]. Another portion of the material continues to ablate after the pulse strike and achieves lower "sonic" speeds. This Late-Time Ablation phenomenon or LTA is thought to be the main mechanism causing the PPT's low thrust efficiency.[1]

While the PPT is primarily an electromagnetic thruster, its thermal pressure component of thrust can be significant. It's contribution to the total impulse per pulse, can vary from 10% to 40% [1][43][11]. The electromagnetic component scales linearly with the discharge energy. The scaling of the electrothermal component varies depending on the thruster geometry [1][11]. The current work focuses primarily on the electromagnetic aspects. hence the thruster will be modeled as an electromagnetic thruster, as is common practice[1][44].

There are different ways of classifying PPTs. Other types of PPTs can have a liquid or gaseous propellant. These promise for an increased efficiency as they require less energy to vaporise and ionise the propellant. On the other hand, propellant feed systems are more complex as they require tubing and valves[45]. In contrast the propellant feed-mechanism of an APPT is a mechanical spring[1]. There are also alternative electrode geometries possible, such as coaxial PPTs. These are a set of cylindrical electrodes, a smaller electrode placed concentrically with in a larger hollow electrode[1][10]. Alternative propellant-feeds and electrode geometries were discussed in more detail within the literature study[46].

## 1.3 Past PPT Experiments

The first satellite to use electrical propulsion was the Zond 2, launched by the Soviets in 1964. The US later had successful missions, such as LES-6/8/9 using the same PPT concept as Zond 2.[1]. These PPTs had a system mass in the order of 5 kg. The Zond 2 had a specific impulse of 410s at a thrust of 2 $mN$, at a pulse rate of 1 Hz. The PPTs used on the LES 9/9 had an Isp of 1000s at an average impulse of 297 $\mu N \cdot s$.[1], and had a discharge rate in the range of 1-2 Hz. A modern PPT, such as those designed by Mars Space Limited[5], have a system mass of 350g or 450g with a thrust at 40-90 micro-Newton at an Isp of 600 N. Design sizes can even go as low as a mass of 150g, 0.3 W average power, 28.4 Ns total impulse and a discharge chamber size of $90 \times 90 \times 25mm^3$.

A plethora of of literature data on PPTs were identified and discussed in the literature study[46]. Most of the data was focused on the relation between thruster dimensions, capacitor energy and thrust performance (specific impulse, efficiency etc...). This project is more focused on the arc discharge properties of the thruster, such as electron density and temperature. Five experiments that provided these measurements in within the thruster channel where identified: the Current Sheet Canting Experiment (CSCX)[47], Simplex [48][27], ADD-Simplex[42][4], experiments by Zhou [49] and Zhang[50]. These are presented in table 2.

[3]Electrothermal propulsion signifies that the propellant is heated electrically. It is then expanded through a nozzle to convert it's thermal energy to kinetic energy, just like in chemical rockets.[9]

[4]1 eV = $1.6 \cdot 10^{-19}$ J = 11605 K [5]

[5]https://mars-space.co.uk/ppt

| Thruster | CSCX | SIMPLEX | ADD-Simplex | Zhou et al. | Zhang et al |
|---|---|---|---|---|---|
| w [mm] | 100 | 40 | 24-0 | 12 | 18 |
| h [mm] | 50 | 36 | 21 - 46 | 25 | 20 |
| L [mm] | 600 | 87 | 80 | 14 | 15 |
| C [$\mu F$] | 10x10,8x18 | 40 | 80 | 2 | 10 |
| V [KV] | 5-10 | 2 | 0.9 - 1.3 | 1.5 | 1.5 |
| I [KA] | 60 | 12 | 11-20 | 6 | 15 |
| $n_e$ [$10^{22} m^{-3}$] | 3-10 | | 2.7-37.2 | 12-22 | |
| $T_e$ [eV] | 2.4 | 1.5-3 | 1.7-3.1 | 1-1.2 | |
| B [T] | 0.36-0.7 | 0.7 | 0.8 | | 0.46-0.55 |

Table 2: Benchmarks Thrusters. The first three rows are the design specifications: width (w), distance between electrodes (h) and electrode length (L). The second group are circuit parameters: capacitance (C), power source (initial) voltage (V) and peak current (I). The final group are measurements of electron density ($n_e$), temperature ($T_e$) and magnetic field B. The role of current parameters is discussed in more detail in section 2.2

All of these devices have a parallel plate geometry, as illustrated in figure 1. CSCX is a gas-fed PPT meaning that a gaseous propellant is pumped into the channel at each pulse. The other thrusters have a solid propellant that is situated at the capacitor-side of the parallel plates. ADD-Simplex has electrodes that are flared outwards (figure 2). This effects the downstream particle density and acceleration. Besides the propellant feed mechanism, the capacitance also influences the discharge current and frequency, together with resistance and inductance (discussed in section 2.2). The inductance and resistance of a circuit can be estimated on the basis of experimental discharge measurements. The capacitance is determined by the designers' choice of capacitor. It is listed to give an indication of thruster behaviour.

PPTs are typically a few centimeters in width and height. CSCX was a relatively larger sized device compared to the others listed in table 2 or described in Burton's review of PPT literature[1]. The focus of this experiment was to visualize the plasma and investigate non uniformities[51]. In any case, the plasma properties are in similar ranges. Electron temperature is typically between 1 and 3 eV while the peak electron density can be in the order of $10^{22} - 10^{23} m^{-3}$. The next section discusses how this categorizes the discharge regime.

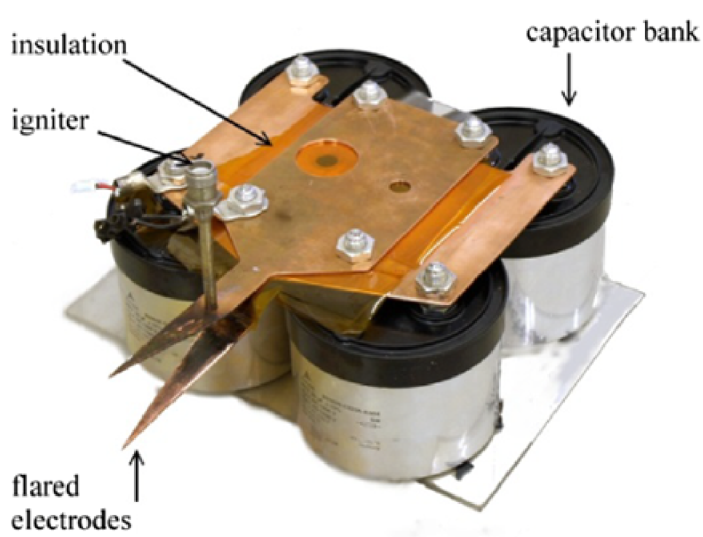


Figure 2: ADD-Simplex Thruster [4]

## 1.4 Plasma Physics Basics

Plasma are often referred to as the "fourth state of matter". Matter undergoes a phase transition as the temperature rises and the molecules become more energetic. A solid melts to form a liquid and a liquid evaporates to form a gas. When a gas is energized by temperature increase or an electric discharge, it will disassociate into a form of freely moving charged particles (ions and electrons). Due to these charge carriers, a plasma is electrically conductive [52]. A plasma is sensitive to long range electric and magnetic forces. Which makes it challenging to control for engineers to control but also gives it several interesting applications in the fields of manufacturing, nuclear fusion and space propulsion [52][5][8].

A plasma can be a a partially ionized gas or fully ionized. The ionization degree ($\alpha$) represents the ratio between the ion density $n_i$ and the density of neutral particles $n_n$:

$$\alpha = \frac{n_i}{n_i + n_n} \tag{1}$$

Even though charged particles can float freely in a plasma, for a volume of a certain size there generally is an equal amount of ions and electrons. Spontaneous charge separation can occur on length scales on the order of the Debye length. For larger distances these rapidly neutralize due to long range Coulomb force. This leads to the condition know as ***quasi-neutrality*** [5][8]:

$$n_e = \sum_i Z_i n_i \tag{2}$$

Where $Z_i$ is the ionization number and $n_i$ is the density of ions. The Debye length $\lambda_D$ is given by [5]:

$$\lambda_D = \left(\frac{\epsilon_0 T_e}{e n_0}\right)^{1/2} \tag{3}$$

For the operation parameters ($T_e = 1 - 3eV$ and $n_e = 10^{19} - 10^{23} m^{-3} s^{-1}$) within the main discharge mode (thermal-arc) of the PPT, the Debye length is in the order of micrometers. This is far smaller than the typical dimensions of the PPT channel which range from a few millimeters to a few centimeters, hence the plasma is considered quasi-neutral on this scale.

There are two situations for PPTs when this condition does not hold. The conditions of quasi-neutrality does not hold within the initial phase of the discharge while the electron density is low[52]. Neither does it hold in the proximity of conducting surfaces because electrons diffuse at a higher rate than ions. Hence a space charge develops at the walls that is dubbed the plasma sheath[5].

### 1.4.1 Plasma Sheath

When a plasma comes in contact with a conducting wall, the electrons will diffuse at a higher rate than the heavier ions. A negative voltage is established between the wall and the main plasma that repels electrons and electrostatically accelerates ions. This region is called the plasma sheath. Here the electron density drops relative to the ion density, as can be seen in figure 3. To maintain flux balance between electrons and incoming ions, the ions need to accelerate in a region called the pre-sheath. The ions enter the sheath with a minimum velocity equal to the Bohm velocity $u_B$. [5]:

$$u_{si} \geq u_B = \sqrt{\frac{eT_e}{m_i}} \tag{4}$$

Where the ion mass is given by $m_i$ and $T_e$ is the electron temperature in eV. The kinetic energy of an ion travelling at the Bohm velocity is equivalent to the electron temperature [52]. As ions accelerate in the pre-sheath, their density drops because of mass conservation as can be seen in figure 3. An approximation for the plasma density $n_0$ at the sheath edge in relation to the plasma density $n_b$ in the bulk can be assumed:[6]

$$n_{se} = n_b/2 \tag{8}$$

[6] To derive this start with the momentum conservation equation:

$$p_e + p_i + mnv^2 = \text{constant} \tag{5}$$

Where the plasma is quasi neutral throughout the bulk and sheath ($n = n_i = n_e$ and $n_0 = n_{i0} = n_{e0}$). The ion flux towards the wall $g_i$ is determined by multiplying the ion density at the sheath edge $n_{i0}$ with $u_B$.

$$g_i = n_{i0}\sqrt{eTe/m_i} \tag{9}$$

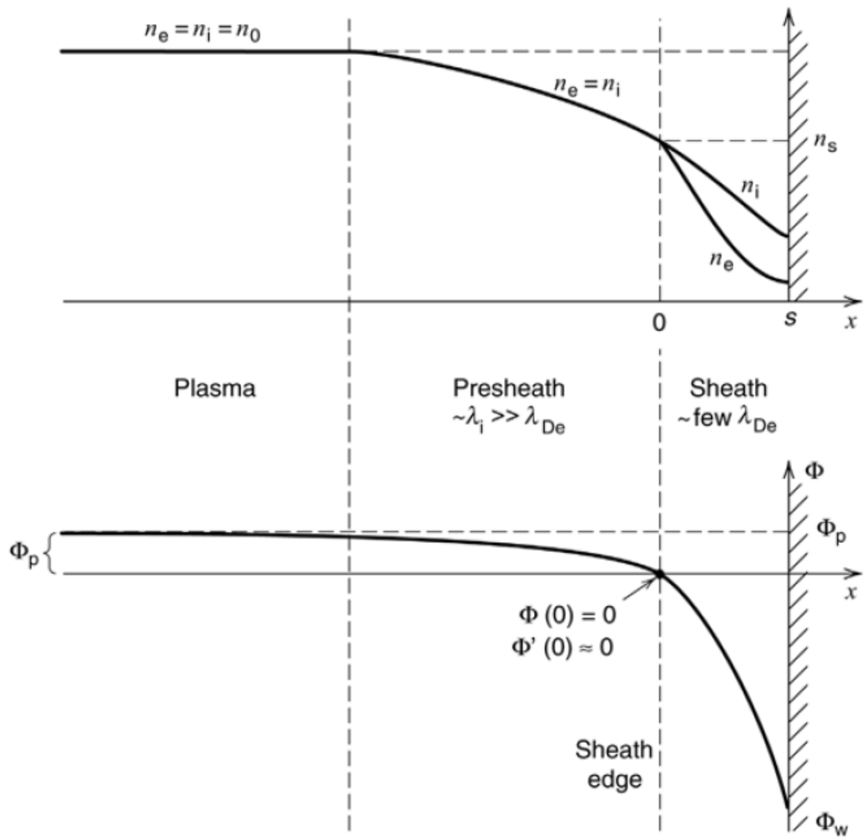


Figure 3: Qualitative behavior of sheath and pre-sheath in contact with a wall. Density of the electrons and ions are represent end by $n_e$ and $n_i$ respectively. The potential drop within the plasma, $V_f$ (depicted here as $\Phi_p$ ) , constitutes the pre-sheath E-field that accelerates the ions to speed $v_{se}$ at the sheath edge (se). The aim is to determine the value of $\Phi_p$. Image from Liebermann[5].

The thickness of the sheath is generally on the order of a few $\lambda_D$. The conditions of the sheath change when a voltage bias is placed on the conducting walls. For high voltages it is on the order of tens of $\lambda_D$[5]. Particle collisions also influence the sheath properties. However, in a typical PPT plasma the mean-free-path is still an order larger than the $\lambda_D$, therefore the sheath can be considered non collisional [53]. Taking all of this and equation 3 into account, the sheath thickness in a PPT would be on the order of 0.01 mm or less. This is significantly smaller than the thruster dimensions $\sim 1-5$ cm of a typical PPT[1].

The electron to wall flux $g_{bolz}(V)$ in a plasma sheath can be calculated using the Boltzmann relation[5,

Where $p$ is particle pressure. Assuming $T_i \approx 0$ and $T_e =$ constant, one can equate the momentum before the pre-sheath and at the sheath edge:

$$n_b T_e = n_{se} T_e + m_i n_{se} u_B^2 \tag{6}$$

Where ions have accelerate to the Bohm velocity $u_B$ at the sheath edge. This can be rewritten to define the density at the sheath edge:

$$\frac{n_b}{n_{se}} = 1 + \frac{m_i u_B^2}{T_e} = 2 \tag{7}$$

p. 168, 172]:

$$g_{bolz}(V) = n_{e0}\sqrt{\frac{eT_e}{2\pi m_e}}\exp(\frac{eV}{T_e}) \tag{10}$$

where $n_{e0}$ is the electron density at the sheath edge and V is the voltage drop over the sheath in Volts. The potential drop can also be written in the dimensionless form $\varphi$:

$$\varphi = \frac{eV}{T_e} \tag{11}$$

Which shortens equation 10 to:

$$g_{bolz}(V) = n_{e0}\sqrt{\frac{eT_e}{2\pi m_e}}\exp(\varphi) \tag{12}$$

### 1.4.2 Plasma Discharges

In the case of the PPT, the plasma is generated by an electrical discharge. A large voltage between the electrodes causes a breakdown of the Teflon vapor. The Teflon vapor becomes a conductor and the capacitor discharges. The term "gas discharge" is used to define such a system where a gas is ionized by an electric field[52]. There are several ways to classify plasma discharges, with each type having different properties. One such way is the distinction between Direct-Current (DC) (e.g. glow, arc and pulsed corona discharges) and non-DC (e.g. radio frequency or microwave discharges) [52]. A non-DC plasma is characterized as a discharge oscillating at a frequency significantly higher than the "plasma frequency". Plasma frequency indicates the characteristic times for which spontaneous charge densities can exist in a plasma[5]:

$$f_p = \frac{1}{2\pi}\sqrt{\frac{e^2 n}{m\epsilon_0}} \qquad [Hz] \tag{13}$$

where $n$ is the particle density (for ions or electrons), $m$ is the particle mass, $e$ is the elementary charge and $\epsilon_0$ is the vacuum permittivity. The ion ($\geq 10^4$ MHz) and electron ($9 \cdot 10^5$ MHz) plasma frequencies [54] in a PPT plasma are significantly higher than the PPT discharge frequency (an underdamped transient response with a resonance frequency typically in the 100 MHz range[1][27]). This means that the voltage oscillation of the PPT discharge is much slower than the natural oscillations that may occur in the plasma. Hence the PPT discharge can be approximated by a DC discharge model[5].

Two broad and commonly used categories of DC discharges are glow discharges and arc discharges. Arc discharges are characterised as high pressure $\sim$ 1 bar, high current $\geq$ 1 A, low voltage $\sim$ 10 V[52, 6-7]. On the other hand, glow discharges are characterised as low pressure $\sim$ 100 Pa, high voltage, low current and weakly ionised plasma[52, 6-7]. These can be seen in figure 4; along side the "dark discharge" which is covers the initial plasma break down. In most aspects the PPT discharges is similar to a thermal arc discharge given that the electron temperatures found in a PPT plasma are in the $\geq$ 1 eV range and the density is in the $10^{22}m^{-3}$ range [1]. The voltage is higher than that of a typical arc discharge[52]. The plasma likely transitions through the different discharge regimes illustrated in figure 4. The PPT discharge only resides in the glow regime for a small fraction of the pulse, likely at the beginning and end.

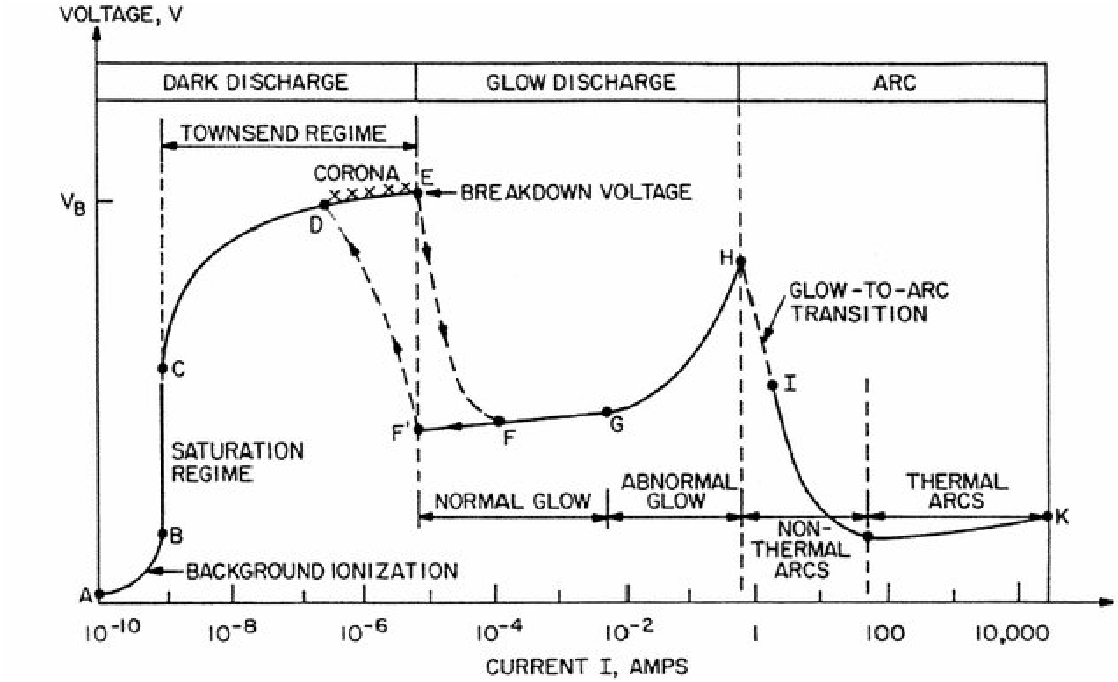


Figure 4: I-V characteristic for DC gas discharge regimes[6]

Based on the density and temperatures in table 2, the PPT discharge is well within the high pressure (thermal) arc regime according to the typical parameter space characterised in figure 5.

### 1.4.3 Electron Emissions

Arc discharges are dominantly characterised by thermionic electron emissions and field electron emissions. Secondary electron emissions generally play a small role (with the exception of gliding arcs). In arc discharges the cathode receives significant amounts of heating from the ion current [28][52]. Hot thermionic cathode arcs provide high current through thermionic emissions when the cathode surface temperature to reaches temperatures of 3000 K [52]. When using high melting temperature materials (such as carbon, tungsten, molybdenum, zirconium and tantalum) for the cathode material these temperatures can be pursued. When low melting point materials (like copper, iron or silver) are used, the high temperature cannot be sustained.

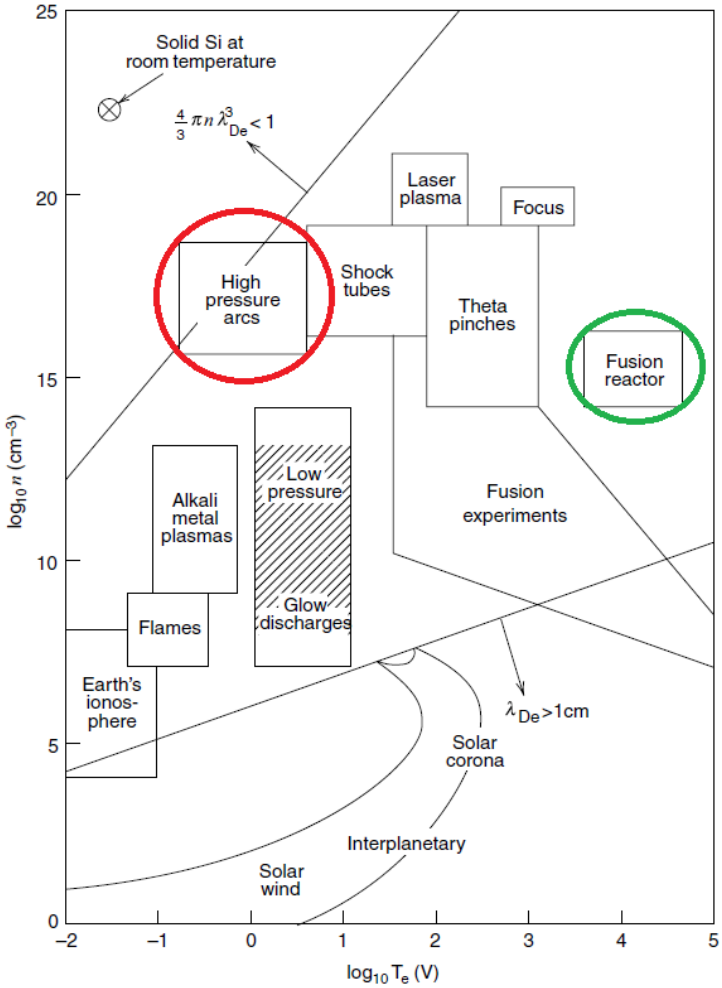


Figure 5: Discharge regimes on a logarithmic density vs temperature plot. High pressure (thermal) arc discharges (red) is the typical regime of a PPT. The core of a fusion reactors such as tokamak is in the area encircled in green. Temperature is given in volt which can be used interchangeably with electronvolt[5].

Electric current then flows through "cathode spots" which are small hot spots of evaporating material that move quickly over the surface. Cathode spots are regions of high localized temperature. The conductor material evaporates providing the necessary electrons while the rest of the electrode stays relatively cold. [52] Several experiments have provided measurements of trace amount of copper found in charred deposits on the electrodes. These spots come into existence due to heating by the plasma ion bombardment [28]. Cathode spots appear for intervals of $10^{-4}s$ and have sizes of $10^{-4} - 10^{-2}cm$ [52]. These spots start out small and fast travelling ($10^3 - 10^4$ cm/s) before merging into slightly larger. The larger spots move more slowly over the cathode (10 - 100 cm/s). The minimum current $I_{min}$ of a cathode spot is [52]:

$$I_{min} \approx 2.5 \cdot 10^{-4} T_{boil}(\mathrm{K})\sqrt{\lambda, \mathrm{W/cm\ K}} \tag{14}$$

Where $T_{boil}$ is the boiling temperature of the electrode material and $\lambda$ is the thermal conductivity. For copper which has a boiling temperature of 3200 K, this is a minimum current of 1.6 A per spot. The current can go up to 300 A and the local current density is in the range of $10^4 - 10^8 A/cm^2$. In the cathode spot, the local temperature exceeds 3000 K, allowing thermionic emissions to be dominant. [52]

Under certain conditions anode spots can appear and contribute charged particles to the current[28], when the anode is small compared to the arc current[52]. Generally the potential drop near the anode region is very small or negative, hence the ion current in this region is diminished[52]. Generally the cathode is the source of particles, while the anode behaves as a passive collector[21].

### 1.4.4 Plasma Sheath Configurations for discharges

Generally when the plasma comes in contact with a surface, the solid surface has a negative space charge which repels electrons and accelerates ions. This creates a positive space charge in the plasma close to the surface. For a classical sheath, the electrode surface has a lower potential than the bulk plasma as visualized in figure 3[5]. In a thermal arc discharge, most of the applied potential is taken up by the cathode sheath[52][21][7]. The blue line in figure 6 illustrates this situation. When the electrode surface is highly emitting a "space charge limited sheath" or SCL may form. The electron emissions at the cathode cause a negative space charge at the surface which leads to a potential bump (green line in figure 6).

In general, the anode potential is lower than the bulk plasma because the loss of electrons to the anode would exceed the global loss rate of ions[7] and thus break charge conservation. In the case that the anode is relatively small[52], the plasma is electron rich or the cathode emits a significant amount of electrons, this no longer is an issue[7][21]. In such case case the anode sheath enters "inversed mode". The anode potential is positive relative to the plasma bulk and the anode accelerates electrons while repelling ions[21]. The cathode can either be in classical mode or SCL in this case.

When emissions are sufficiently high the negative space charge region near the cathode grows and the cathode sheath may invert as well. Campanell formulates a (double) inverse mode where the potential of both cathode and anode are higher than the plasma potential[7]. This occurs when the electron emissions of the cathode surface crosses a certain threshold. In this case there is no electrical resistivity in the bulk plasma, while in SCL and classical mode a small resistive field is present[7]. A comparison can be seen in figure 6. It is hypothesized that the doubly inversed sheath may occur in PPT discharges[28]. However, it is likely that only the anode sheath is inversed[28][21]. Given the complexity of calculating the transition towards an inversed sheath, in this project it will be assumed that both anode and cathode sheath are in the classical mode.

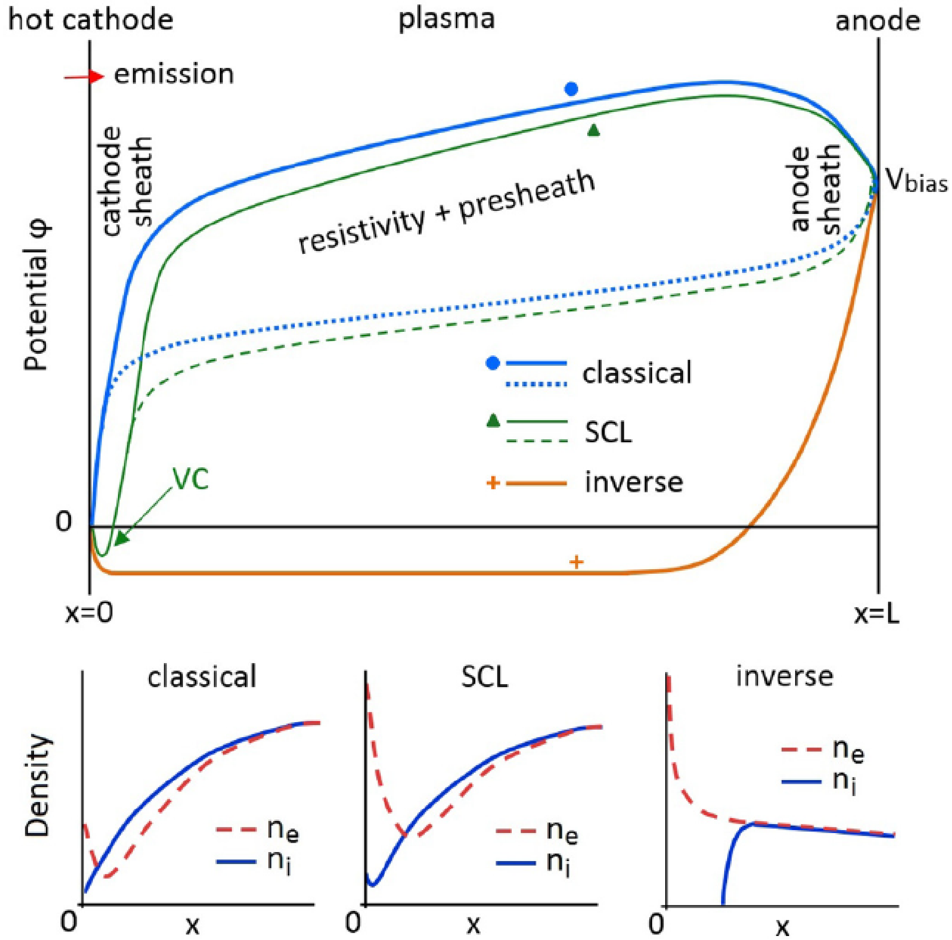


Figure 6: Possible potential and density profiles in a thermal discharge [7].

### 1.4.5 Magnetized Plasma

Up to now the electrical interaction in a plasma has been discussed. Plasma are also sensitive to magnetic fields. For one a particle with charge $q$ moving perpendicular to a magnetic field $\mathbf{B}$ with velocity $\mathbf{u}$ will experience a force perpendicular to both velocity and magnetic field[8]:

$$F_L = q \cdot \mathbf{B} \times \mathbf{u} \tag{15}$$

This Lorentz force $F_L$ is the primary force driving acceleration in PPT [1]. If undisturbed a charged particle will make gyrations around the magnetic field lines as the component of the random thermal motion that is perpendicular to the field is deflected into circular motion[5]. The angular frequency of these gyrations ($\omega_c$) is called the gyrofrequency or cyclotron frequency:

$$\omega_c = \frac{qB}{m}[rad/s] \tag{16}$$

Which rotate with gyroradius $r_c$:

$$r_c = \frac{mv_\perp}{qB} \tag{17}$$

where $v_\perp$ is the component of particle velocity that is perpendicular to the magnetic field. This can typically be assumed to be equivalent to the random thermal motion of a plasma[8]:

$$v_\perp = v_{th} = \sqrt{\frac{2\hat{T}}{m}} \tag{18}$$

where $\hat{T}$ is the temperature of the particle species in joules. Generally the gyrations are interrupted by inter particle collisions. A plasma is considered " magnetized" when the particles are able to complete their gyrations as seen in figure 7. This holds when characteristic dimension of the plasma $L$ is is significantly larger than the gyrofrequency.

$$L \gg r_c \tag{19}$$

Furthermore the gyrofrequency needs to be higher than the coulomb collision rate $\nu$ [7]:

$$\omega_c \, 2\pi\nu \tag{20}$$

The ratio between the gyrofrequency and the collision frequency is called the hall parameter ($\beta$), which indicates how large a hall current component ("i.e. perpendicular to the magnetic field and applied electric field") component of a total discharge current may be[47]:

$$\beta = \frac{qB}{m\nu} \tag{21}$$

## 1.5 Comparison to Fusion devices

As discussed in the project context, certain regions of a fusion reactor may display similar properties to a PPT. This section describes the general working of a magnetic confinement fusion reactor and region within the reactor (the divertor) where the plasma comes into contact with the wall. Several fusion power concepts are being researched to provide fossil-free energy for the future. These technologies rely on nuclear fusion, which is the process that powers the sun. Two lighter atomic nuclei, such as hydrogen isotopes, fuse and release significant amounts of energy[8]. The positively charged nuclei repel each other due to electrostatic forces. Only when they come close enough does the short range strong nuclear force over power the relatively long range electrostatic force. The electrostatic energy needed to be overcome so that the nuclei can fuse is called the "coulomb barrier". Fusion reactions therefore occur at a high temperature plasma state. As figure 4 shows, fusion experiments are done at temperatures in the range between 10 eV and 100 KeV [5]. This is because the nuclei need significant kinetic energy to overcome the coulomb barrier.

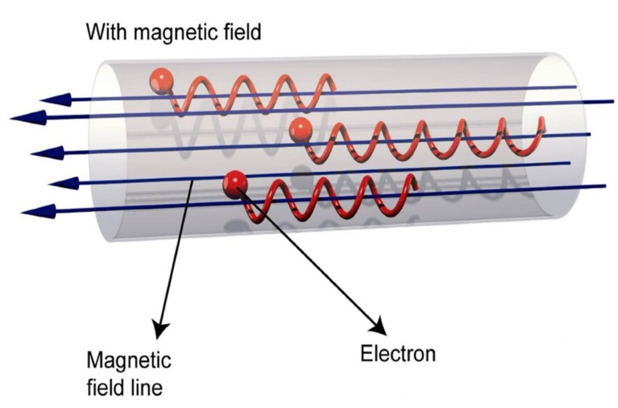


Figure 7: The principle of magnetic confinement fusion. Charged particles in a plasma gyrate around magnetic field lines due to the Lorentz force. Image source: Iter.org

[7]This is the rate of collisions between particles in the plasma. The equation is given in section 3.4.6

The most researched fusion concept is magnetic confinement fusion, where by the plasma is constrained using electromagnetic forces [8]. Particles gyrate around magnetic field lines due to the Lorentz force as seen in figure 7. To prevent the particles from going out of the end of such a solenoid, the magnetic field is twisted into a toroidal shape. For a normal toroid, the magnetic field at the outer edge of a symmetrical toroid is weaker than the field inside. This would lead to the particles drifting outwards and striking the wall. The solution is to twist the magnetic field as in figure 8. There a two leading concepts for this: stellarators and tokamaks. A stellarator has twisted coil shapes. While a tokamak drives current through the plasma which generates the poloidal component of the helical field.

The largest fusion experiment in the world, ITER, is a tokamak. The plasma is confined in a toroidal shaped magnetic field. The plasma is highly magnetized. Radial diffusion of particles and heat is greatly reduced by the helical magnetic field, allowing the core to reach temperatures of 15 KeV (160 million degrees Celsius). Plasma conditions can vary strongly throughout the reactor. Temperatures in the plasma closer to the reactor wall is lower. Figure 9 illustrates the last closed magnetic flux surface, called the "seperatrix", which prevents plasma from coming in contact with the reactor wall [8][18].

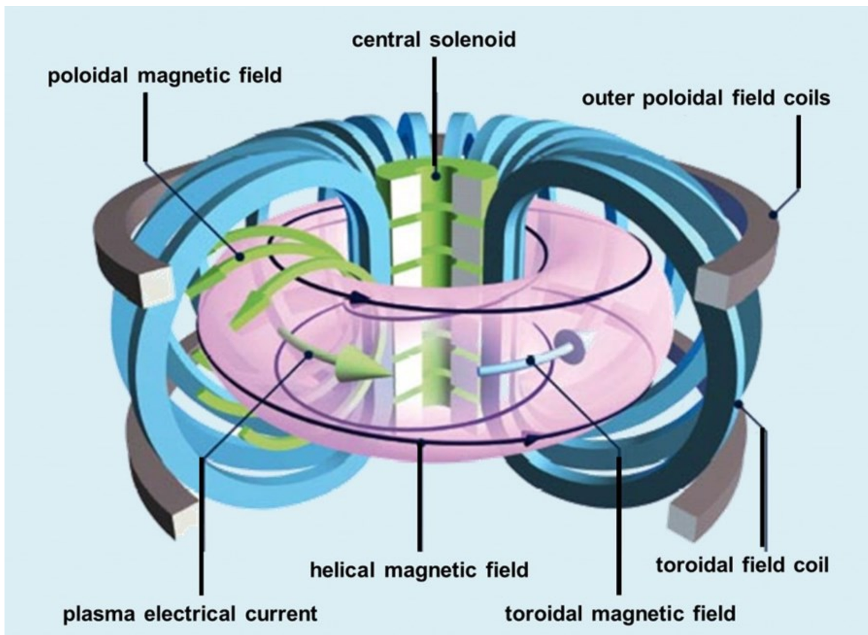


Figure 8: The tokamak concept. Particles are trapped in a toroidal field. Image source: Iter.org

The divertor is a region in the tokamak where the plasma is intentionally allowed to come in contact with the wall. Extra coils at the divertor create a magnetic "null point" where the field lines cancel out and the plasma can diffuse through the separatrix towards the wall. The divertor is used to remove the impurities from the plasma and isolate the rest of the wall from the plasma. The plasma is cooled down to the 1-5 eV temperature range and electron density raises to $10^{21}m^{-3}$[55], before coming in contact with the wall. The plasma needs to be cooled down to avoid direct deposition of the exhaust heat on the divertor surface through conduction. When the plasma temperature decreases to the eV range, black-body radiation becomes an effective energy sink allowing the total heat flux to depose on a larger area. Generally it is proposed to achieve the injection of neutral fuel particle or higher Z impurities[56].

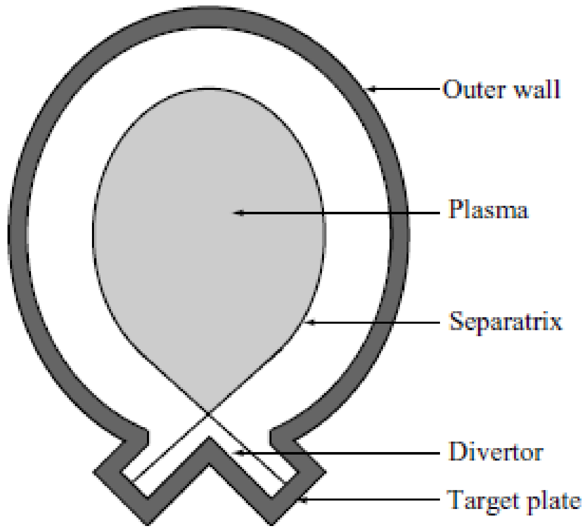


Figure 9: Schematic of the magnetic field in a cross-section of the tokamak[8].

## 1.6 Research questions

To design more efficient PPTs it is beneficial to improve the understanding of the physics of PPTs. This can be done by identifying the dominant physical mechanisms and investigating the influence of design and operational parameters on these mechanisms. This project investigates the role of electron emission mechanisms in the plasma sheath and their influence on plasma current. The project objective is stated as :

*"to improve the understanding of the dominant physical mechanisms within the plasma sheath affecting the plasma current of the PPT, and investigate the influence of design and operational parameters on these mechanisms."*

Design parameters are defined as the physical dimensions of the device, as well as the material properties of the electrode and propellant material. Operational parameters are defined in this project as the operational conditions of the PPT. This includes the applied voltage across the electrodes, the electron temperature, density, ionization degree, downstream velocity and magnetic field. With the exception of the voltage across the electrodes, these parameters are a function of the other parameters listed before. Given that this project only treats a partial model, these parameters are assumed to be known. These are essentially treated as black box parameters.

For this research, design and operational parameters are taken as inputs. Given these parameters, the mechanisms that are studied in this project are the electron emissions from the electrodes, momentum exchange collisions and sheath potential drop. This leads to the primary research question which investigates the dominant physical mechanisms in the plasma discharge. The secondary question investigates the synergies between the current research and nuclear fusion research as this project is a collaboration between aerospace and fusion research groups.

1. **What are the dominant physical mechanisms in the plasma discharge?**
   (a) Which physical processes, when included in simulation, have a significant effect on transverse plasma flow properties?
   (b) How are these processes influenced by the design and operational (electrode voltage, propellant type, electron density, electron temperature, geometry) parameters?
   (c) How is plasma resistance influenced by design and operational parameters (including ionization degree)?
   (d) Can various distinct operating regimes, (i.e. with different scaling laws) be identified?

2. **Which crossover applications do PPT modelling and Fusion have?**
   (a) How do the physical conditions in a PPT and certain regions of a fusion reactor compare?
   (b) How does the magnetic geometry between a PPT and certain regions of a fusion reactor compare?
   (c) How do the plasma parameters between a PPT and a fusion reactor compare?
   (d) What adaptations would the PPT model need to simulate conditions in a fusion reactor?

The specific physical processes that are investigated question 1.a are the different electron emissions mechanisms[8] and the self inducting magnetic field[9]. It will be gauged if these have a significant effect on the output (current level and sheath potential). The presence of neutral particles in the plasma may influence plasma resistance through particle collisions. These have no direct influence on magnetic field and electron emissions. Hence, ionization degree is only included in the analyses of question 1.c. Finally, question 1.d looks for trends, in the output of the model, that are indicative of operating regimes and scaling laws. By answering questions and improving the understanding of the PPT physics, a solid foundation will be provided for future studies on the design optimisation of PPTs.

Question 2.a refers to a comparison of the physical properties such as electron temperature, and electron density between the two devices. As discussed in section 1.5, the conditions vary in different regions of a tokamak. A search will be done for the region with the most physical similarities to compare. This comparison should also be done for the magnetic geometry (question 2.b). Magnetic geometry influences the dynamics of charge particles[8]. Depending on the orientation of the magnetic field and the bulk motion of charged particles, certain dimensions can be neglected. The question is whether the relevant dimensions for simulation between a PPT and certain regions of a tokamak overlap. The physical conditions and magnetic geometry effect characteristic parameters such as Debye length, collision rate, gyration frequency and hall effect number. This influences the dynamics of the plasma. After assessing these differences and similarities, it will be possible to make recommendations on which changes would be needed to make the simulation model applicable for fusion research as well as PPT research.

## 1.7 Research Plan

As part of an effort to simulate the plasma flow in a pulsed plasma thruster it has been opted to build a quasi-2D multifluid code. This code will consist of a coupling of an axial fluid code, which simulates the downstream flow of the plasma using Method of characteristics, with a transversal fluid code, that simulates the electron current that is perpendicular to the bulk flow. This current work is focused exclusively on the development of the transverse model in numerical form, while the output of the axial model is assumed to be known. This model, described in section 3, focuses on sheath interactions and particle collisions and attempts to make a self-consistent simulation of the axial current density distribution.

The transverse model, object of the present work, considers thin slices of the plasma. A set of equations will calculate electrode emissions, sheath potential drop, charge continuity and equations of motions considering the Lorentz force and particle collisions. This model will be developed into a Matlab script that uses an iterative non-linear solver. A parametric analysis will be performed in terms of design and operational parameters to examine how the output scales. The model will be verified using literature data and older models. On the basis of this it will be determined which input parameters for the model are significant. In the future, the transverse model will be integrated with the axial code to form the proposed quasi-2D multifluid code. However this is beyond the scope of the present work.

## 1.8 Thesis Structure

First a description on the state of the art of PPT plasma modelling will be given in section 2. The model, that was developed and used in this project, is described in section 3. This includes a description of the macro structure of the transverse model within the context of the quasi 2D simulation code (section 3.1); a list of symbols, function names and parameters (section 3.4). The functions, of the transverse model, are further described in section 3.4, followed by a short overview of the set of equations to be solved by this code (section

[8] These mechanisms are elaborated in section 3.4.2

[9] Different ways of modelling the self induced magnetic field are discussed in sections 2 and 3.

3.4.6). To kick start the numerical solver some initial guesses of the output is required. This is given in section 3.4.7. The verification and validation of the model using benchmark scenarios are discussed in section 4 and 5 respectively. The process to validate the model included extensive analyses of its behaviour. Some further analysis beyond the benchmark scenarios is discussed in section 6. An analyses of how applicable this research is for nuclear fusion research and what modification of the codes would potentially be needed is discussed in section 7. Finally the conclusions and recommendation are presented in sections 8.1 and 8.2 respectively.

# 2 Historic PPT Plasma Flow and Circuit Models

While the physics of plasma acceleration in PPTs are not yet fully understood, various models have provided reasonable performance predictions for these devices[1][38]. The first and still most commonly used PPT models were reported by Jahn in 1968 [9]. The essential function of a pulsed plasma thruster is to accelerate propellant mass by the self-applied magnetic and thermal forces[1][9]. The acceleration of the plasma bridge is a function of the electrical current passing through the plasma arc. The plasma current strength is a function of the position and velocity of the moving element. The dynamics of this system is nonlinear. Therefore it is often approximated with several heuristic models[9]. Models describing the fluid dynamics from a macroscopic perspective are described in section 2.1. To calculate the Lorentz force, the current in the circuit must be determined. PPTs are considered underdamped LRC circuits[10], which is further discussed in section 2.2. The macroscopic model assumes the plasma bridge to be a homogeneous slab. The more complex multifluid plasma models, described in section 2.3, can investigate more details on the fluid motion of the plasma such as the momentum and energy exchange between different species of particles (ions, electrons and neutrals) at different temperatures[1][9]. The object of the current work, the transverse model will mainly be based on multifluid models and incorporate some aspects of circuit elements, which will be described in section 3.

## 2.1 Macroscopic Dynamic Models

The acceleration of the plasma in a PPT channel can be described in terms of Lorentz force and gasdynamic acceleration. The accelerating plasma can be modeled as a monolithic slab of a fixed thickness while ignoring internal structure[9].

### Slug Model

The slug model simplifies the ejection mass as a monolithic, impervious and conducting slab of plasma that travels down the axis $z$. The current is confined to a thin outer layer of the plasma due to the skin effect and the interior structure of this plasma is ignored. This entails that non-downstream flow of plasma is neglected. The plasma does not change mass during its trajectory downstream [9]. The basic underlying equation relates the acceleration ($\ddot{z}$) of propellant mass ($m$) to current and induction:

$$m\ddot{z} = hw \int_0^{\delta} \mathbf{J} \times \mathbf{B} dz = \frac{\mu_0 h}{2w} i^2 = \frac{1}{2} L' i^2 \tag{22}$$

where $\delta$ is the current zone thickness, $\mu_0$ is the permeability of free space, $h$ is the distance between electrodes, $w$ is the width of the electrodes, and L' is the change in channel inductance per unit length ($\nabla L$). The current density and magnetic vector are represented by **J** and **B**. The total circuit current is represented by $i$. As the plasma arc travels downstream the length of the circuit increases, changing the inductance. For a rectangular circuit the L' can be calculated as [1, 44, 57]:

$$L' = \nabla L = 0.4 + 0.6 ln \frac{h}{w + t_{el}}, (\mu H/m) \approx \mu_o \frac{h}{w}, (H/m) \tag{23}$$

where $t_{el}$ is the thickness of the electrodes.

Integrating the acceleration over the pulse duration one derives the impulse per pulse $I_{bit}$ [1]:

$$I_{bit} = \int_0^{t_{pulse}} \frac{1}{2} L' i(t)^2 dt \tag{24}$$

The Electric Propulsion and Plasma Dynamics Laboratory at Princeton (EPPDyL) had built and tested two gas-fed coaxial PPTs, the PT5 and PT9. Ziemer and Choeuri had demonstrated that the the Impulse bit of PT5 and PT9 was scaled linearly with the integral of the current squared ($\int i^2$) [3]. According to equation 24, the impulse should be proportional to $L'/2 \int i^2$. However few of Ziemer's experiments showed these trends, indicating that certain loss mechanisms are not taken into account by the slug model[3].

[10] A circuit containing inductive, resistive and capacitor elements. For an underdamped circuit, the closing of the circuit results in an oscillation with an amplitude that decays over time.

**Snow Plow Model**

The slug model neglects the sweeping of ambient gas as the current sheet sheet progresses along the electrodes. The snow plow model adds this phenomenon to the model. The advancing plasma is seen as an impenetrable sheet pushing out the ambient gas in a manner similar to a snow plow pushing snow. In contrast to the slug model which is only applicable in specific situations, the snow plow model can predict plasma sheet motion in a broad range of operational parameters[9]. A term is added to the left hand side of equation 22 to allow mass accumulation of the ambient gas by the advancing "snow plow" current sheet.

$$m\ddot{z} + \dot{m}\dot{z} = \frac{1}{2}L'i^2 \tag{25}$$

**Gas Dynamic Model**

One refinement that can be made to the snow plow model is to acknowledge the compressibility of the entrained ambient gas. The advancing current, which is still treated as impermeable, now acts as a piston pushing a shock front of ambient gas in front of it. The velocity of the current sheet $u_p$ and the shock front $U$ can be approximated by the following equation[9]:

$$U = \frac{\gamma+1}{2}u_p \tag{26}$$

The width of the shocked gas zone, as well as its density and temperature, are dependent on the heat capacity ratio $\gamma$. The snow plow can be seen as a simplification of the gas dynamic model for a completely compressible gas ($\gamma = 1$). The shock wave relations for density $\rho$, pressure $p$ and temperature $T$:

$$\frac{\rho_2}{\rho_1} = \frac{\gamma+1}{\gamma-1} \tag{27}$$

$$\frac{p_2}{p_1} = \frac{\gamma(\gamma+1)}{2}\left(\frac{u_p}{a_1}\right)^2 \tag{28}$$

$$\frac{T_2}{T_1} = \frac{\gamma(\gamma-1)}{2}\left(\frac{u_p}{a_1}\right)^2 \tag{29}$$

where $a_1$ is the sound velocity in the ambient gas.

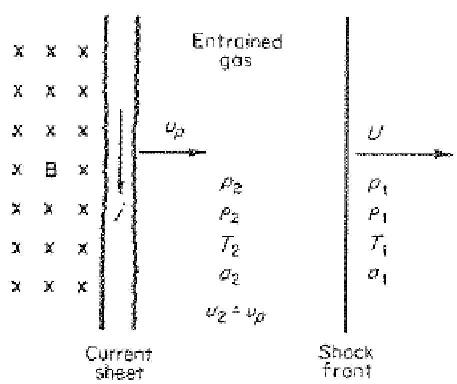


Figure 10: From Jahn[9]: "One-dimensional constant speed shock wave model"

The gas captured between the shock front and the advancing "piston" is only uniform in the case of constant piston speed. The Method of Characteristics can be applied to the situation of an accelerating piston. This method is considered to be one of the most accurate methods for solving the partial differential equations relevant to shock waves in compressible fluids[58]. The down-side is that it requires complex iterative evaluation[9].

During the development of the LES 6 thruster, Solbes and Vorbes measured the gasdynamic contribution to thrust and had proposed the following analytical equation for the impulse per pulse (impulse bit or $I_{bit}$) as a sum of an Electromagnetic (EM) and a Gasdynamic component (GD) [1][59]:

$$I_{bit} = (I_{EM} + I_{GD}) = \frac{1}{2}L' \int i^2 dt + \Delta m U_0 \tag{30}$$

where the velocity $U_0$ and inductance were determined by a curve fit to the experimental data. The ablated mass per pulse is represented by $\Delta m$. This is essentially the slug model with an added gasdynamic component. The predictive value of this model is limited as the gasdynamic component is determined experimentally.

Guman proposed the following analytical formula for the combined electromagnetic and gas dynamic contributions[1][60]:

$$I_{bit} = I_{EM} + I_{GD} = \frac{1}{2}L' \int i^2 dt + \Big[\frac{8(\gamma-1)}{\gamma^2(\gamma+1)} \cdot \Delta m \cdot E\Big]^{0.5} \tag{31}$$

where the gasdynamic component is a function of the capacitor energy $E_0$ and the heat capacity ratio *gamma* ($\gamma = 1.3$ for Teflon. This expression is only valid if the pulse length is very short, on the order of 1 $\mu s$ because it assumes that all the energy was added to the arc before any propellant mass ablates. However it has been use full to predict that the impulse bit is improved if a nozzle is added to the PPT[1].

## 2.2 Circuit Analysis

The dynamic models discussed in the previous section, all described the plasma acceleration as a function of a circuit current. To determine the current the system can be idealized as a set of discrete but movable circuit elements as seen in figure 11. The movement of the elements in turn is calculated by the dynamic models[9].

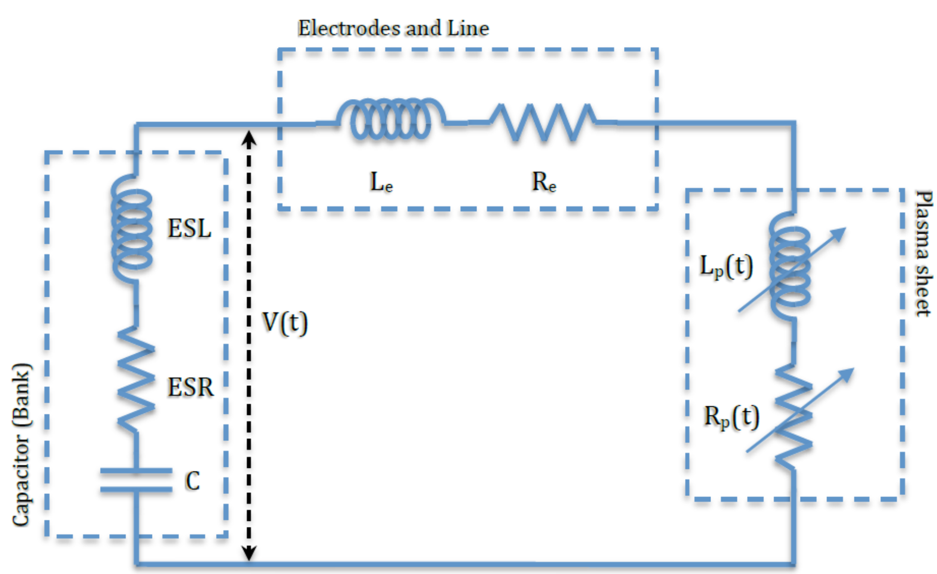


Figure 11: PPT equivalent electric circuit [10, p. 37]

PPTs are generally provided power by an LRC[9][27][1] circuit as seen in figure 11. The plasma is represented as a homogeneous sheet with a constant thickness that travels down stream. Three groups of electrical elements are represented. C is the capacitance. ESR and ESL are the electrical resistance and inductance of the power system respectively. The electrodes and other circuit components have their own inductance $L_e$ and resistance $R_e$. In contrast to the other elements, the plasma bridge is not static, but moves downstream during the discharge. Hence the plasma inductance $L_p(t)$ and resistance $R_p(t)$ are time dependant.[10]

Applying Kirchoff's law renders the following equation for the voltage measured across the electrodes $V(t)$[10][29]:

$$V(t) = \Big[R_e + R_p(t) + \frac{dL_p(t)}{dt}\Big] i(t) + \Big[L_e + L_p(t)\Big]\frac{di(t)}{dt} \tag{32}$$

This equation can be rewritten in terms of capacitance and plasma sheet position: [10]:

$$\begin{cases} \Big[\frac{1}{C} + R'\dot{z} + L'\ddot{z} + L"\dot{z}^2\Big] i + \Big[R + 2L'\dot{z}\Big]\dot{i} + L\ddot{i} = 0 \\ m_{bit}\ddot{z} = \frac{1}{2}L'\int_0^{t_d} i^2 \end{cases} \tag{33}$$

Where R and L are the circuit equivalent resistance and inductance. The physical down stream position of the plasma bridge is indicated by $z$. The first equation is the circuit representation of the PPT. The second equation is the dynamic representation of the plasma bridge. In this case the slug model is used. Equation 32 can be simplified by assuming that the resistance and inductance are constant elements. Experimental current wave forms for experiments do not deviate significantly from analytical models that ignore the transient nature of plasma properties[11][48][61][38]. This can be seen in figure 12. This circuit can now be represented as:

$$V(t) = i(t)R + \dot{i}(t)L \tag{34}$$

The current represents an LRC underdamped sinusoidal oscillator for $CR^2/4L < 1$[9]:

$$i(t) = \frac{V_0}{\omega L} e^{(-R/2L)t}\sin(\omega t) \tag{35}$$

Where the oscillation frequency is:

$$\omega = \sqrt{(1/LC) - (R^2/4L^2)} \tag{36}$$

The constants used in these equations equations can be determined on experimental basis. $C$ is the capacitance of the chosen capacitor bank. Average inductance $L$ is related to $C$ and the oscillation time period $T$[48]:

$$T = 2\pi\sqrt{LC} \tag{37}$$

R can be deduced from the maximum current measured $I_{max}$[27]:

$$I_{max} = \sqrt{\frac{2E_0}{L}}\exp\Big(-R\frac{\pi}{4}\sqrt{\frac{C}{L}}\Big) \tag{38}$$

Where $E_0$ is the energy stored in the capacitor[10, p, 55]:

$$E_0 = \frac{1}{2}CV_0^2 \tag{39}$$

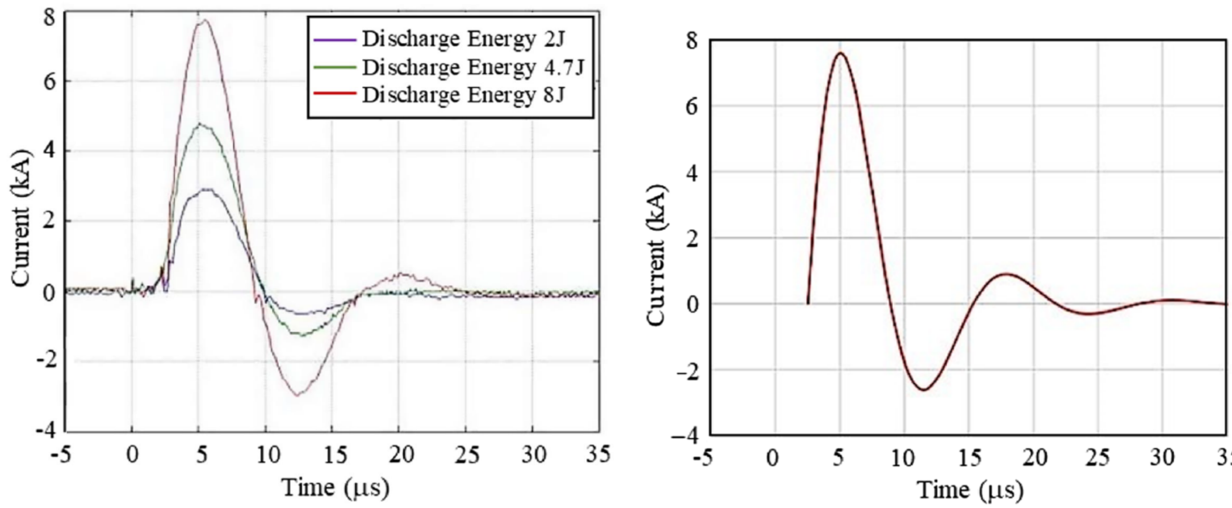


(a) PPT circuit current waveforms measured during experiments of the ARC thruster[61][38]. The distortions caused by varying plasma resistance and inductance have a low amplitude and high frequency.

(b) Theoretical current wave form for the 8j ARC thruster, calculated by assuming constant resistance (45 mΩ) and inductance (150 nH).[61][11]

Figure 12: Comparing the experimental waveforms on the left with the theoretical idealization on the right, one observes that the omission of the transient nature of plasma resistance and inductance has a negligible effect on the current waveform[11].

## 2.3 Multifluid Plasma Modeling

In section 2.1 three heuristic models were presented for the dynamics of the plasma bridge. These models lack certain complexities that have been observed in thruster experiments such as the the different density distribution for the different species of particles (electrons, ions and neutrals)[9]. To investigate the momentum and energy exchange between the different kinds of particles these particle species can be treated as separate fluids. Traditional fluids are influenced influenced by thermal and vicious forces. A plasma consist of charge particles that are also influenced by long range coulomb forces. Studying the behaviour of such conducting fluids is called magnetohydrodynamics (MHD)[8]. The equations of motion in MHD are determined by integrating the Maxwell-Boltzmann distribution, which describes the velocity and position probability distribution for a particle species [18][5]:

$$\frac{\partial f_i}{\partial t} + \mathbf{v} \cdot \nabla_{\mathbf{r}} f_i + \frac{\mathbf{F_i}}{m_i} \cdot \nabla_{\mathbf{v}} f_i = \left(\frac{\partial f_i}{\partial t}\right)_c \tag{40}$$

The first term on the left hand side represents the time dependant change of the distribution, the second term is the change due to spatial gradients and the third term gives the distribution change due to forces (viscous or electromagnetic) acting on the species. The gradient operators in position and velocity space are represented by $\nabla_{\mathbf{r}}$ and $\nabla_{\mathbf{v}}$. The conservation relations for bulk fluid properties; such as conservation of mass, charge, momentum and energy; are derived by taking integral moments of the Boltzmann transport equation[5]. These conservation equations are presented in this section.

### 2.3.1 Particle conservation

This is the classic continuity of mass equation, taking into account the creation of ions and electrons through ionization and the creation of neutrals through recombination [5].

$$\frac{\partial n_j}{\partial t} + \nabla \cdot (n_j \mathbf{u}_j) = G - L \qquad j = i, e, n \tag{41}$$

where $n$ represents the density of particle species $j$, which can be either ions $i$, electrons $e$ or neutral particles $n$; the average velocity of particles species $j$ is $\mathbf{u}_j$; G and L represent particle population gains and losses respectively.

### 2.3.2 Conservation of momentum

In magnetohydrodynamics the particle momentum is affected by electromagnetic as well as thermal forces. The conservation momentum equations are set up by combining the Navier-Stokes equations with Maxwell's electrical equations[8]. The first term on the right hand is the electromagnetic force term. The second term is the pressure term. After this are the particle collision (friction) terms.

$$0 = -en_e(\mathbf{E} + \mathbf{u}_e \times \mathbf{B}) - \nabla p_e + m_e n_e \nu_{ei}(\mathbf{u}_i - \mathbf{u}_e) - m_e n_e \nu_{ne}(\mathbf{u}_e - \mathbf{u}_n) \tag{42}$$

$$m_i n_i \Big(\frac{\partial}{\partial t} + u_i \cdot \nabla\Big) u_i = en_i(\mathbf{E} + \mathbf{u}_i \times \mathbf{B}) - \nabla p_i - m_i n_i \nu_{ni}(\mathbf{u}_i - \mathbf{u}_n) - m_i n_i \nu_{ii}(\mathbf{u}_i - \mathbf{u}_n) \tag{43}$$

$$m_n n_n \Big(\frac{\partial}{\partial t} + u_n \cdot \nabla\Big) u_n = \nabla p_n - m_i n_i \nu_{ni}(\mathbf{u}_n - \mathbf{u}_i) \tag{44}$$

The three equations are for electrons, ions and neutrals respectively. For the electron momentum equation the electron mass (on the left hand side) is neglected because the electron response times are very high relative to the time an ion to transit the the plasma at thermal velocity, which is the time scale considered in MHD simulations[8].

### 2.3.3 Conservation of Energy

In MHD, the generalized conservation of energy equation is described as[8]:

$$\frac{3}{2} n_j \Big(\frac{\partial}{\partial t} + \mathbf{u}_j \cdot \nabla\Big) T_j + p_j \nabla \cdot \mathbf{u}_j + \nabla \cdot \mathbf{q}_j = S_j \qquad j = i, e, n \tag{45}$$

Where the first term on the left hand side is the rate of change of internal energy of a fluid element. The second term is the compression work within a non-homogeneous flow field. The third term is the heat conduction within a plasma element that is not in local thermal equilibrium (LTE) [8]. On the right hand side is the sum of heat sources and sinks for the plasma element. For a pulsed plasma thruster these can be described as the sum of ohmic (electrical resistance) heating, convection and radiation loss. With radiation heat exchange playing a minor role in the total energy output[62][63].

The conservation of energy equations are not considered within this project as the particle temperature $T_j$ and density $n_j$ are selected as user inputs. This values can be chosen based on measurement data in literature (typical values were presented in section 1.3). This approach reduces the complexity of the model. Energy conservation equations can be added in future iterations of the Quasi-2D model.

## 2.4 Comparison of Models

The models presented in this section represent different aspects of PPT dynamics. The macroscopic models simplify the internal structure of the plasma to a monolithic slab, but at different levels of complexity. The slug model represents the PPT pulse as a single slab moving in a vacuum. The snow plow adds a surrounding gas which can accumulate. Results using the snow plow model show more rapid acceleration at the start of the pulse then at the end, when more ambient mass has accumulated[9]. In either case, one observes that the acceleration of the plasma slug is dependant on the square of the plasma current $i^2$. Gas dynamic models take the compressibility of the ambient gas into account. This allows for the simulation of the plasma density and temperature over time. According to simulations with the slug and snow plow model, the plasma slab continuously accelerates over the channel.

Ziemer had shown that the slug model overestimates the impulse produced by the thruster[44] due to the neglect of energy loss mechanisms. Burton describes several models that include a gasdynamic component in his review of the state of PPT technology [1]. These models have limited validity due to their underlying

[10] $\sqrt{eT_i/m_i}$, with $T_i$ as the ion temperature in eV and $m_i$ as the ion mass in kg.

assumptions and experimentally determined parameters. Burton points out that a model that these types of models that assume a homogeneous plasma, utilize limped circuit representations and empirical scaling laws are limited when it comes to incorporating physical processes. The current in a plasma discharge does not necessarily flow perpendicular to the electrodes, nor is the flow purely axial. Electron density may vary from region to region. Electrons and ions interact they may recombining and cause friction to each others flow. MHD modelling allows the representation of these processes[1]. MACH 2 is an example of an MHD code that that has been used for plasma accelerators, MPDTs and PPTS [1] and is capable of providing the density and temperature distributions within the plasma discharge as a function of position and time. The code solves the equations of mass continuity and momentum by assuming a single compressible fluid. It can use two energy equations for the ions and electrons which are not in thermal equilibrium. The code can be complemented by tables from the SESAME library for the equation of state [29][1]. However this does not necessary secure better results. Henrikson had taken an MHD approach to predict thrust and efficiency performance in 2008[29]. The results of this analyses over predicted thrust by an order of 1.25 to 2 when compared to experimental measurements. Henrikson concludes that this may be the result of the sesame data being incomplete[29]. A later model by Henrikson and Mikellides in 2019 for parallel electrode plasma thrusters using the slug model with gasdynamic effects obtained better results[38]. Here the gas dynamic component is a function of the current. Which essentially describes the resistance energy transfer by the discharge. This model reported a maximum discrepancy with experimental values of 15% for ablated mass and 10% for impulse bit.

Another approach not yet taken used is the method of characteristics. This captures the dynamics of an advancing shock front[58]. It will be employed by the axial component of the quasi-2D model, that this current study will contribute to. It will be combined with the transverse model, discussed in the next section, which investigates the electrical current flow through the plasma, using aspects of circuit modelling and MHD. As mentioned in the introduction, at lower current levels the sheath potential drop can dominate the thruster voltage, decreasing the electromagnetic force[26]. Hence the transverse model will take sheath interaction into account. There are mechanisms by which the electrodes release electrons to the discharge, thereby contributing to current. These have received little attention within PPT modelling efforts with the exception of Neudorfer et al [31]. Neudorfer had modelled the electron emissions with a stochastic model. The current work takes three different electron emission mechanisms (secondary, thermionic and field-electron emissions) into account using analytical equations. These will be discussed in section 3.4.2.

# 3 Transverse Plasma Model

The previous chapter described three types of models for PPTs that are often used in combination with each-other. The focus of the current work is the the application of plasma modelling to simulate the electron flux moving from cathode to anode (transverse direction). In contrast to previous PPT models, it will incorporate analytical equations for the flux emissions at the electrodes. This model will be a component of a future Quasi-2D code which is introduced in section 3.1. This introduction also discusses the flow of information transverse model and other components of the Quasi-2D model. A focused description of the transverse model is given in 3.2. This is followed by a description of input and output parameters used in this report (section 3.3) and a description of the governing equations of the transverse model (section 3.4).

## 3.1 Introduction: Coupled Quasi-2D plasma model

Consider a parallel planar PPT with a width $w$ is far larger than the distance between the electrodes $h$. The z-axis is the downstream or *axial* direction. The x-axis is the *transverse* direction which goes from the positive lower electrode (anode) to the negative upper electrode (cathode). A schematic of this model can be seen in figure 13.

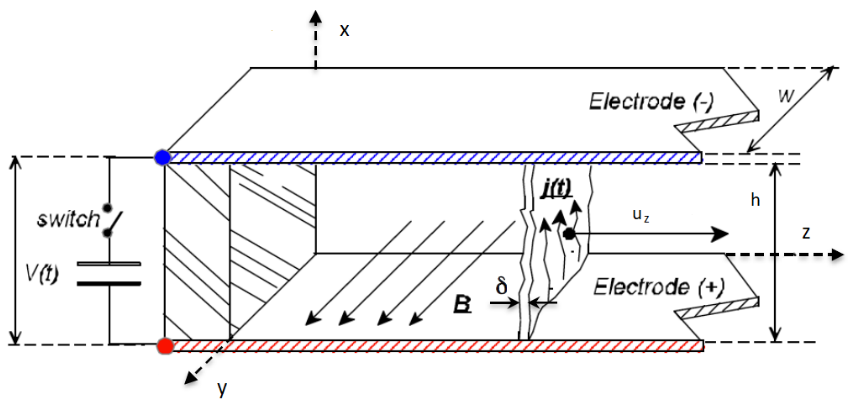


Figure 13: Schematic of the parallel plate accelerator, with magnetic field **B** and a perpendicular current sheet, of thickness $\delta$ and current density $\mathbf{j}(t)$, travelling outward at velocity $u_z$. Taken from [10][9] and adapted for the model used in this project.

The power supply is treated as a black box in this work. In other words the externally applied voltage ($V(t)$ in figure 13) is a considered a user-defined input. The magnetohydrodynamic plasma equations, as described in 2.3, are applied to the accelerating current sheet. The plasma consists of ions, neutrals and electrons which are considered to have a Maxwellian-distribution, (except for the sheath region) and be in local thermal equilibrium. The electron inertia is neglected and the ions are assumed to be frozen. Quasi-neutrality is assumed in the bulk.

This multifluid model is than split into two concurrent 1-D models: an axial fluid flow model and a transverse current model. The axial model deals with the transient supersonic plasma flow using the Method of Characteristics. The transverse model, which is the subject of this thesis, deals with the plasma current, resistance and sheath properties as well as the electrode emission mechanisms (which are discussed in section 3.4.2). The plasma resistance is calculated based on momentum transfer collisions.

The balance of the circuit loads (resistance, inductance) and electrode electron emissions are calculated within the transverse model code. By iterating between the two codes (transverse and axial) the Quasi 2D will provide a self consistent calculation of plasma current and axial acceleration. The inductance load in the transverse model is dependant based on the magnetic field. The magnetic field $B_y$ is calculated in the axial model by integrating the current density **J** according to ampere's law [5][8]:

$$\nabla \times \mathbf{B} = \frac{\partial B_y}{\partial z} = \mu_0 \mathbf{J} \tag{46}$$

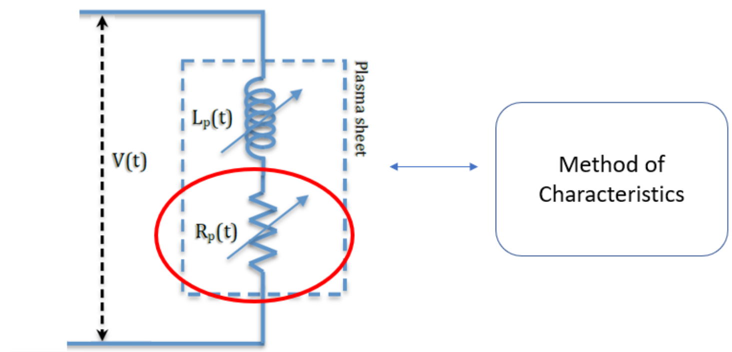


Figure 14: The blue dashed box, "Plasma sheet" is the transverse model. The inductance of the plasma sheet is calculated based on the magnetic field which is calculated in the axial model. The red circle is exclusively calculated within the transverse model. The box on the right hand sight is the axial model which uses the Method of Characteristics.

The scope of the transverse code is illustrated in figure 14. The flow of information between the transverse code and axial code is represented in figure 15. The process goes as follows: design parameters and energy supply circuit parameters are determined by the user. To kick start the transverse model estimates of the output variables, i.e. initializing values, are needed. After the first time step, the output of the previous state is used as initial estimate.

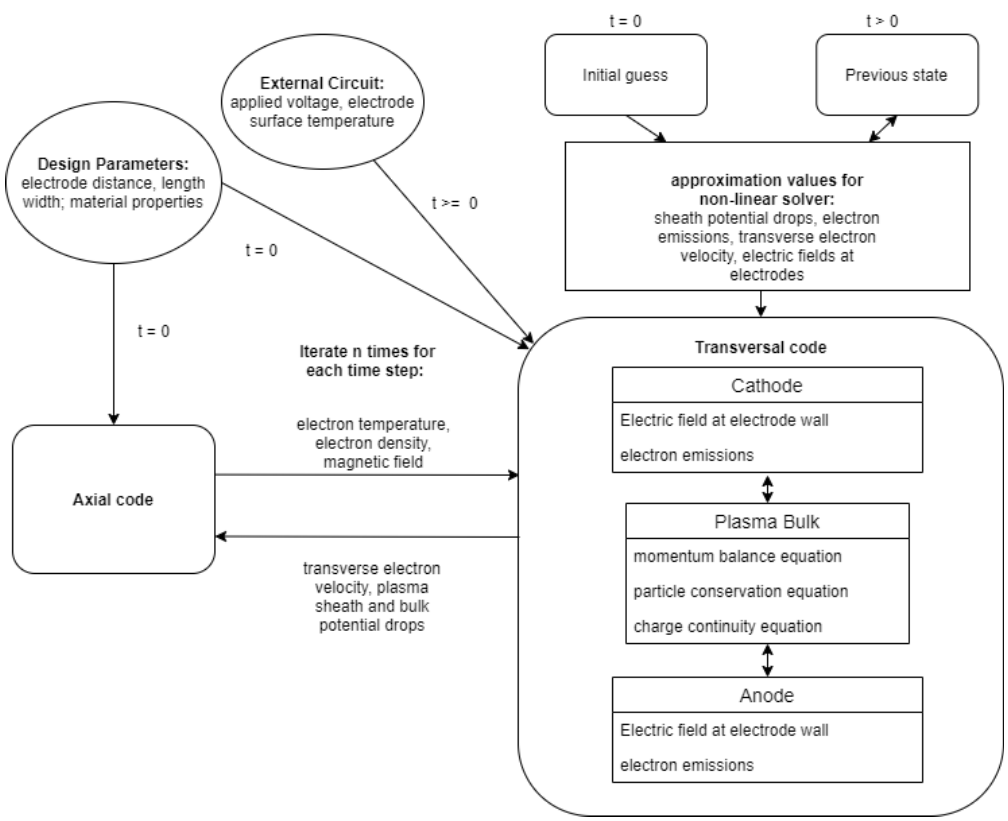


Figure 15: Flow diagram of parameters and sub-processes

The axial code provides values for the electron temperature, electron density, axial flow speed and magnetic field to the transverse code. The transverse code in turn provides the average transverse electron velocity and sheath potential drops back to the axial code. The transverse electron velocity is used to calculate the plasma current and the sheath potential drops are used to calculate the bulk plasma resistance. These inputs and outputs are described in section 3.3.

The axial code is treated as a black box in the current work. In the future Quasi-2D code, at each time step of the model an iteration between the axial code and transverse code will take place. The exact iteration scheme for this still has to be designed. The best option would be to start the time iteration step using axial and transverse states from the previous time step. Then iterate between the two codes until the corresponding variables in both states converge.

## 3.2 Overview of the Transverse Model

The flow chart presented in figure 15, describes how the transverse code consists of seven governing equations. Together these calculate the potential drop profile in the transverse direction, illustrated in figure 16. For this project the classical sheath mode, discussed in section 7.3, was assumed. In this profile the horizontal axes represents the x axis of the model, in other words the direction perpendicular to the plasma flow. The vertical axis represents voltage.

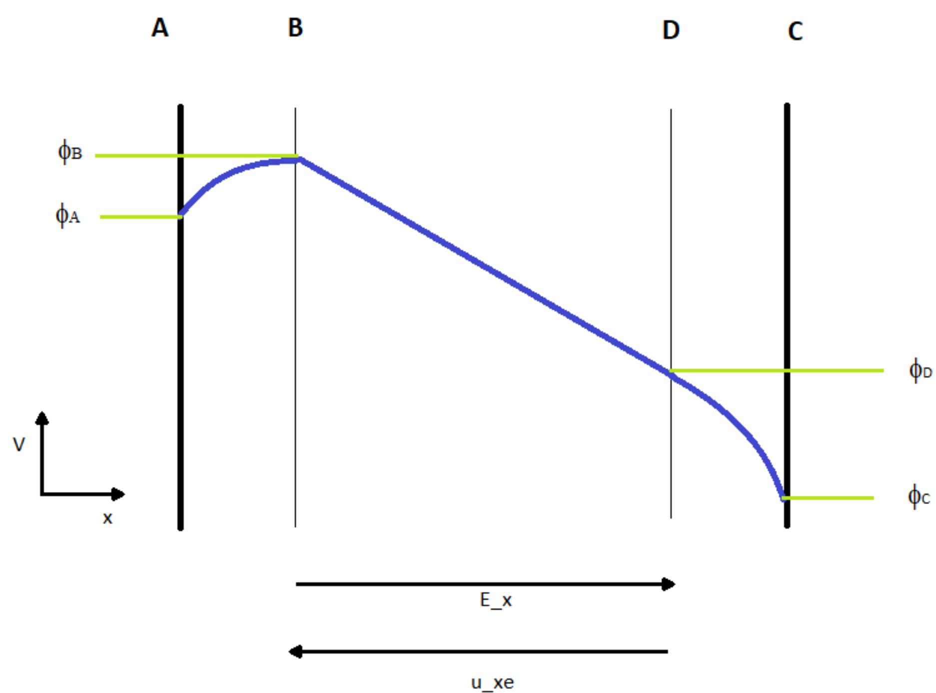


Figure 16: Sketch of the voltage potential profile (classical mode) at a cross section of the PPT channel. The plasma in this model is cut up in to three regions: the bulk and the two electrode sheaths. The A and C lines represent the Anode and Cathode respectively. B and D represent sheath-bulk boundaries. The Anode sheath is the space between A and B. The plasma bulk is the region between B and D. The cathode sheath is the space between D and C. This figure is not to scale as the sheath thickness is on the order of micrometers. The symbols $\phi_A$,$\phi_B$,$\phi_C$,$\phi_D$ represent the electric potential at those respective points.

There are two sets of sheath equations, one for the anode the other for the cathode. These determine the electrode emissions to the sheath, and the electric field at the electrode surface. The emissions are dependant on this wall electric field, which in turn is dependant on the sheath potential drop. In this model both sheaths drops are assumed to be negative. In other words the potential of the electrode is lower than the sheath edge. A positive sheath drop at the anode is possible [52] but is out of the scope for the current work and will be the subject of future research. Furthermore the sheath has been assumed to be collisionless, meaning that the mean free path of the ions is significantly larger than the Debye length [5].

The bulk equations consists of: the electron momentum equation, the charge continuity equations and the particle conservation equation for the electron flux in the bulk. Within this system of equations, the electron flux, the sheath potential drop and the transverse electron velocity are independent variables, which is discussed in section 3.3. The equations of this system are discussed in section 3.4.

### 3.3 Input and Output Parameters

This section gives an overview and categorization of the parameters used in this report. Table 3 describes the parameters that are regarded as fixed during each simulation by the transverse code. In table 6 the variable parameters or "unknowns" of this model are listed. This includes seven independent variables, of this models governing system of equations (discussed in section 3.4.6), and variables that are dependent on these. The left most column in each of these tables are the mathematical symbols used in this report. The second column is the description of these quantities. If present, the third column describes the unit.

The parameters that are fixed for the duration of one time step in simulation (table 3) are divided in four categories: axial code output variables, external circuit parameters, design parameters and material properties. Furthermore several equations used by this model contain physical constants, such as the Boltzmann constant $k_b$ or elementary charge $e$. These are listed, with the values and units used in this project, in the Nomenclature section of this report. The first category of parameters, the axial code output variables, are the variables calculated in the axial code at each time step. The external circuit parameters are dependent on the time varying voltage pulse supplied by the capacitor. These are the voltages of the electrodes. The anode potential peaks at the max voltage at a few microseconds and then has an attenuated oscillation. The electrode wall temperature $T_w$ is the surface temperature of the material of the electrode. A heat transfer model will be developpped in a future iteration, of the coupled 2-D model, to determine the cathode and anode temperature based on the plasma to wall flux and radiative heat balance of the arc. This is beyond the scope of the current work. For now the wall temperature can be selected by the user. Typical values discussed in section 3.4.2. The design and material parameters are fixed during the entire simulation. These are passed on to the axial- and transverse models at the start of the simulation. Design parameters are the physical dimensions of the device. Material properties are determined by the propellant and electrode material choice.

| Axial Code Output Variables | | |
|---|---|---|
| $T_e$ | Bulk electron temperature | eV |
| $\hat{T}_e$ | Energy associated with bulk electron temperature | J |
| $n_e$ | Bulk electron density | $m^{-3}$ |
| $u_z$ | Axial velocity | m/s |
| $\overline{B}_y$ | Magnetic field (averaged over the bulk) | T |
| **Transverse-Plasma Sheet Parameters** | | |
| $\delta$ | Plasma Sheet Thickness | m |
| **External Circuit Parameters** | | |
| $\phi_A$ | Anode Voltage | V |
| $\phi_C$ | Cathode Voltage | V |
| $T_{w,A}$ | Anode Wall Temperature | K |
| $T_{w,C}$ | Cathode Wall Temperature | K |
| **Design Parameters** | | |
| $h$ | distance between electrodes | m |
| $w$ | width of plasma | m |
| **Material Properties** | | |
| $m_i$ | Ion mass | kg |
| $\mathcal{E}_F$ | Fermi energy | eV |
| $W$ | Work function | eV |
| $\mathcal{E}_i$ | Ionization energy | eV |
| $A_G$ | Schottky constant | $\mathrm{Am^{-2}K^{-2}}$ |

Table 3: Input parameters for the transverse code.

Typical electron temperatures, electron densities, current, voltages and magnetic fields for PPTs were discussed in section 1.3. The axial velocity of ions can be in the 3-50 km/s range[1]. The transverse velocity, listed in 6, is used to estimate the current density:

$$J = en_e u_{xe} \tag{47}$$

This can also be related to total current:

$$I = JA = Jw\delta \tag{48}$$

Where $A$ is the cross-section area of the plasma arc. The discharge spans the width of the electrodes and a finite thickness $\delta$. Based on visualization experiments, this thickness is estimated to be in the 1-2 cm range[51][4].

The material properties depend on the electrode material and propellant choice. Typical materials are copper and tungsten[1][45], their properties are given in table 4. Table 5, lists the properties of propellant elements. Teflon consists of a chain of a carbon fluoride chain[1]. Experiments have been done with hydrogen propellant as well [47]. Hydrogen is used in this work as a proof of concept for the model. How the electrode material and propellant properties influence electron emissions is discussed in section 3.4.2.

| Property | Copper | Tungsten | unit |
|---|---|---|---|
| W | 4.5 - 4.6 | 4.55 | eV |
| $\mathcal{E}_F$ | 7 | - | eV |
| $A_G$ | 60 - 120 | 60 - 80 | $10^4\mathrm{Am^{-2}K^{-2}}$ |

Table 4: Electrode Material Properties [21]

| Property | Hydrogen | Carbon | Fluorine | unit |
|---|---|---|---|---|
| $m_i$ | 1 | 12 | 19 | $1.610^{-27}$ kg |
| $\mathcal{E}_i$ $0 \rightarrow 1$ | 13.6 | 11.26 | 17.42 | eV |
| $\mathcal{E}_i$ $1 \rightarrow 2$ | - | 24.38 | 34.97 | eV |

Table 5: Propellant Properties[21]. Ionization energies for loosing the first two electrons are given

In table 6 the variables of the transverse code are listed. Five dependent variables can be written as linear functions of seven independent variables. The remaining variables have implicit and non-linear couplings between which are discussed in section 3.4.6, including a motivation of why these variables are assumed to be independent.

| Independent Variables calculated in transverse code | | |
|---|---|---|
| $V_A$ | Anode sheath potential drop (between points B and A) | V |
| $\varphi_A$ | Ratio of anode sheath potential drop to electron temperature | dimensionless |
| $V_C$ | Cathode sheath potential drop (between points D and C) | V |
| $\varphi_C$ | Ratio of cathode sheath potential drop to electron temperature | dimensionless |
| $g^{\star}_{e,A}$ | Anode electron emissions | $m^{-2}s^{-1}$ |
| $g^{\star}_{e,C}$ | Cathode electron emissions | $m^{-2}s^{-1}$ |
| $E_{w,A}$ | Electric field at the wall (anode) | V/m |
| $E_{w,C}$ | Electric field at the wall (cathode) | V/m |
| $u_{xe}$ | Bulk transverse electron velocity | m/s |
| **Dependent variables calculated in transverse code** | | |
| $g_i$ | Ion Sheath to wall flux | $m^{-2}s^{-1}$ |
| $g_e$ | Electron Sheath to wall flux, calculated using ge_sw and V_A,C | $m^{-2}s^{-1}$ |
| $\phi_B$ | Anode sheath boundary voltage | V |
| $\phi_D$ | Cathode sheath boundary voltage | V |
| $E_x$ | Bulk electric field | V/m |

Table 6: Variables of the transverse code. There are seven independent variables. The sheath potential drop appears in voltage and dimensionless units. In the former case it is denoted by $V$ and in the latter by $\varphi$. There are five dependent variables in the code that are calculated based on the independent variables and other parameters.

## 3.4 Primary Functions

As seen in figure 15, there are five types of governing equations for this model because the sheath equations are applied twice. These five types of equations are classified as primary functions in this report. This section discusses the five primary functions, together with their respective sub-functions, that are used to determine the voltage profile illustrated in figure 16. Table 7 lists the all of the functions used in this work, along side the section number where they are discussed.

| Built-in Functions | | |
|---|---|---|
| Fsolve | Matlab's non-linear solver function | |
| **Primary Functions** | | |
| f1 (x2) | Electric field at the Wall | 3.4.1 |
| f2 (x2) | Electron Emissions | 3.4.2 |
| f3 | Particle Conservation Equation | 3.4.3 |
| f4 | Charge continuity Equation | 3.4.4 |
| f5 | Momentum Balance Equation | 3.4.5 |
| **Sub-functions** | | |
| SEE | Secondary Electron emissions | 3.4.2 |
| TEE | Thermal Electron emissions | 3.4.2 |
| FEE | Field Electron emissions | 3.4.2 |
| $E_w$ | Electric field at the wall | 3.4.1 |
| $g_e$ | Sheath to wall flux/back diffusion flux | 3.4.4 |
| Axe | Electron Momentum transfer due to collisions | 3.4.5 |

Table 7: Functions applied in the transverse code. The first category is built-in Matlab functions. The second category are the primary functions of the model to be solved. The third category are sub-functions of the primary functions. Functions f1 and f2 are applied twice (once for each electrode) in the system of equations.

Together these will form the governing equations of this model, described in section 3.4.6. This set of equations was implemented in Matlab and are solved by using the built in non-linear solver Fsolve. Fsolve uses the Levenberg-Marquardt algorithm, a non-linear least squares method[64]. This method requires initializing values. The method to select these values is described in section 3.4.7.

### 3.4.1 f1: Wall electric field

This function determines the electric field at the surface of each electrode. It is needed for the electron emissions equation (f2). For this equation the dimensionless form of sheath to wall potential drop $\varphi_w$ is used:

$$\varphi_w = \frac{eV}{\hat{T}_e} \tag{49}$$

Where $V$ is the potential drop from the sheath edge to the electrode in volt and $\hat{T}_e$ is the electron temperature in joules. For the anode sheath this potential drop is:

$$V_A = \phi_A - \phi_B \tag{50}$$

and for the cathode sheath:

$$V_C = \phi_C - \phi_D \tag{51}$$

According to Maxwell's equations the charge density is proportional to the gradient of the electric field and thus the second derivative of the electric potential ($\Phi$):

$$-\frac{e}{\varepsilon_0}(n_i - n_e) = -\nabla E = \nabla^2\Phi \tag{52}$$

To derive equation 63 from this, the following assumptions were made:

1. Ions are accelerated in the pre-sheath to Bohm velocity $u_{i0} \geq \sqrt{T_e/m_i}$
2. The electrons entering the sheath from the plasma bulk have an isothermal Maxwell-Boltzmann distribution
3. The wall electrons emit an electron flux $g_e^\star$ with a characteristic velocity $\sqrt{\hat{T}_w/m_e}$ dependent on energy associated with the wall temperature $\hat{T_w} = k_b \cdot T_w$

Due to the first assumptions the ion density is described as the following:

$$n_i(X)u_i(X) = n_{i0}u_{i0} = g_i \tag{53}$$

$$\frac{1}{2}m_i u_i^2(X) = \frac{1}{2}m_i u_{i0}2 + e\phi_0 - e\phi(X) \tag{54}$$

The local distance coordinate $X = (x_w - x_{se})/\lambda_D$ represents the distance from the sheath edge to the wall divided by the Debye length $\lambda_D$. The density of the plasma bulk electrons $n_e(X)$ entering the sheath follow the Boltzmann's relation under assumption 2:[11]

$$n_e(X) = n_{e0}\exp\Big(\frac{e(\phi(X) - \phi_0)}{\hat{T}_e}\Big) \tag{55}$$

and the flux of plasma electrons reaching the wall is

$$g_{ew} = n_{e0}\exp\Big(\frac{e(\phi_w - \phi_0)}{\hat{T}_e}\Big) \tag{56}$$

For emission electrons:

$$n_e^\star(X)u_e^\star(X) = g_e^\star \tag{57}$$

$$\frac{1}{2}m_e \cdot (u_e^\star(X))^2 = \hat{T_w} - e\phi_w + e\phi(X) \tag{58}$$

Substituting the latter energy equation into the former density equation, the density of emitted electrons in the vicinity of the wall could be described as a function of wall temperature and potential drop:

$$n_e^\star(X) = g_e^\star\sqrt{\frac{m_e}{\hat{T_w}}}\Big(1 + 2\frac{\hat{T}_e}{\hat{T_w}}\frac{e(\phi(X) - \phi_w)}{\hat{T}_e}\Big) \tag{59}$$

The charge density for this plasma sheath is the following:

$$\nabla^2\phi = \frac{e}{\varepsilon_0}(n_e + n_e^\star - n_i) \tag{60}$$

Before substituting the equations into the charge density equations we use the following dimensionless numbers:

$$\varphi = \frac{e(\phi - \phi_0)}{\hat{T}_e}, \qquad \Theta = \frac{\hat{T}_e}{\hat{T_w}}, \qquad c_{e0} = \sqrt{\frac{\hat{T}_e}{m_e}} \qquad M_{i0} = u_{i0}/\sqrt{\hat{T}_e/m_i} \tag{61}$$

where $\varphi$ is the dimensionless sheath potential drop, $\Theta$ is the ratio of the temperatures of bulk electrons to emitted electrons, $c_{e0}$ is the RMS thermal velocity of electrons travelling in any single direction[65], and $M_{i0}$ is the Mach number of ions entering the sheath. Under the Bohm criteria, the assumption $M_{io} = 1$ is made.

$$\frac{\varepsilon_0}{\hat{T}_e n_{e0}}\nabla^2\varphi = \exp(\varphi) + \frac{g_e^\star}{n_{e0}c_{e0}}\sqrt{\Theta}(1 + 2\Theta(\varphi - \varphi_w))^{-1/2} - (1 - 2\frac{\varphi}{M_{i0}^2})^{-1/2} \tag{62}$$

Multiplying this equation by $d\varphi/dX$ and taking $d\varphi/dX|0 = 0$ at the sheath edge, this equation is integrated to derive equation 63. This model assumes that $-\varphi_w > T_e$ and $n_{e0}^\star \ll n_{e0}$. As such the tail of the Electron Velocity Distribution Function can be neglected. [66][67]

$$E_w = \sqrt{\frac{2\hat{T}_e n_{e0}}{\varepsilon_0}}\Big[\exp(\varphi_w) - 1 + \frac{g_e^\star}{n_{e0}c_{e0}}\Theta^{-1/2}[1 - (1 - 2\Theta\varphi_w)^{1/2}] + M_{i0}^2\big((1 - 2\frac{\varphi_w}{M_{i0}^2})^{1/2} - 1\big)\Big]^{1/2} \tag{63}$$

So in essence:

$$E_W = f_1(g_e^\star, V) \tag{64}$$

This equation is applied twice in the model. Once for the cathode and once for the anode.

[11] The electron density at sheath edge is assumed to be half of the bulk plasma density ($n_{e0} = n_b/2$) as discussed in section 1.4.1

### 3.4.2 f2: Electron emissions

Three types of electron emission mechanisms have been identified for arc discharges[52, p. 507-515]: thermal electron emissions (TEE), the field electron emissions (FEE) and the secondary electron emissions (SEE). These are summed up to calculate the total surface emission:

$$g_e^{\star} = TEE + FEE + SEE \tag{65}$$

**TEE** Thermionic electron emissions is the phenomena of thermally energetic electrons getting ejected from the surface of a high temperature metal. Under the influence of an electric field close to the surface these electrons are pushed further away from the surface[8, p. 507]. It is calculated using the following equation:

$$TEE = \frac{A_G}{e} T_w^2 \exp\left( -\frac{W - \sqrt{e^3 E_w/(4\pi\varepsilon_0)}}{K_b T_w} \right) \qquad [m^{-3}s^{-1}] \tag{66}$$

The Schottky decrease $\Delta W = \sqrt{e^3 E_w/(4\pi\varepsilon_0)}$ represents decrease of the work function $W$ due to the electric field $E_w$, in joules[12]. $K_b$ is the Boltzmann constant $1.38 \cdot 10^{-23} J/K$. The unit of the wall temperature $T_w$ is Kelvin in this equation. $A_G$ is given by[68][13]:

$$A_G = \lambda_R A_0 \tag{67}$$

Where $A_0 = 120 Acm^{-2}K^{-2}$ is the universal constant[69] and $\lambda_R$ is the material specific constant[13]. $\lambda_R$ is typical in the range of 0.5 - 1 [21].

Within PPT literature, there is little reporting of the wall temperature. The adjacent propellant block is estimated to reach temperatures between 700 and 1000 K [30]. In thermal-arc discharge literature, tungsten electrodes can reach temperatures of 3000-4000 K [52][13][70]. As discussed in section 1.4.2, for materials with lower melting temperatures (e.g. copper) the thermal emissions are limited to small high-temperature spots[52][28].

**FEE** In very high surface electric fields (in the range of $1 - 3 \cdot 10^9$ V/m), field electron emissions become significant. This is the the direct extraction of electrons from a cold-metal surface through quantum-tunneling[52, p. 510][71]:

$$FEE = \frac{e}{(4\pi)^2 \hbar} P_F E_w^2 \exp\left( -\frac{4\sqrt{2m_e} W^{3/2} \xi}{3e\hbar E_w} \right) \qquad [m^{-3}s^{-1}] \tag{68}$$

Where $\hbar = h_p/2\pi$ is the reduced Planck constant. The prefactor $P_F$ for an idealized potential barrier is [71]:

$$P_F = \frac{4}{W + \mathcal{E}_F} \sqrt{\frac{\mathcal{E}_F}{W}} \tag{69}$$

where $\mathcal{E}_F$ is the Fermi energy of the electrode surface. $P_F$ is generally on the order of 1-2.

The work function $W$ and Fermi energy are in electronvolts in this equation. The exponential correction term $\xi$ is dependent on the relative Schottky decrease ($y = \Delta W/W$) and can be approximated as[72]:

$$\xi \approx 1 - y^2 + (1/3) y^2 \ln y \tag{70}$$

The exponential factor can have a 100-fold multiplier effect on the FEE flux[71].

[12] The value of the work function $W$ is noted in eV for brevity, in this report. To convert to joules, multiply this with the elementary charge $e = 1.6 \cdot 10^{-19} c$

**SEE** Ion bombardment in the sheath can cause electron emissions from the surface. If the ionization energy $\mathcal{E}_i$ of the impacting ion is larger than the work function $W$ it can neutralize by ripping of an electron from the surface. If it is larger than the double of the work function it can rip of extra electrons, giving rise to SEE. SEE is not a relevant phenomenon in arc discharges but is significant in glow discharges[52, p. 513-514]. SEE is calculated using the number of emitted electrons per incident ions $\gamma_{se}$. The following equation uses a linear approximation for $\gamma_{se}$[52][5].

$$SEE = \gamma_{se} g_i \approx 0.016(\mathcal{E}_i - 2W) g_i \qquad [m^{-3}s^{-1}] \tag{71}$$

The ions are assumed to enter the sheath at sound speed (eq. 4). Hence the ion to wall flux $g_i$ is assumed to be equal to $n_{i0}\sqrt{\hat{T}e/m_i}$ (eq. 9)

The previous functions calculate the electron emission fluxes in terms of particle flux ($m^{-3}s^{-1}$). For current density, multiply these numbers by the elementary charge $e$. The dependence of the total electron emissions on other independent variables of this model can be described as:

$$g_e^\star = f_2(E_W, g_i) = TEE(E_W) + FEE(E_W) + SEE \tag{72}$$

### 3.4.3 f3: Particle Conservation Equation

Conservation of momentum dictates that the electron flux passing through the bulk is equal to the net electron flux at the anode and cathode:

$$n_e u_{xe} = g_{eA}^\star - g_{eA} = g_{eC} - g_{eC}^\star \tag{73}$$

However measurements have indicated that the area where the plasma comes in contact with the anode is larger than at the cathode [4][9][51][54]. In this model the bulk current density is estimated by averaging the electron fluxes leaving and entering at points C and D.

$$n_e u_{xe} = \frac{g_{eA}^\star - g_{eA} - g_{eC}^\star + g_{eC}}{2} \tag{74}$$

where the electron to wall flux (also called the back-diffusion flux) is determined by equation 10:

$$g_e = g_{bolz}(V) = n_{e0}\sqrt{\frac{\hat{T}_e}{2\pi m_e}} \exp\left(\frac{eV}{T_e}\right) \tag{75}$$

This dependence is thus best summarized as:

$$u_{xe} = f3(g_{eA}^\star, V_A, g_{eC}^\star, V_C) \tag{76}$$

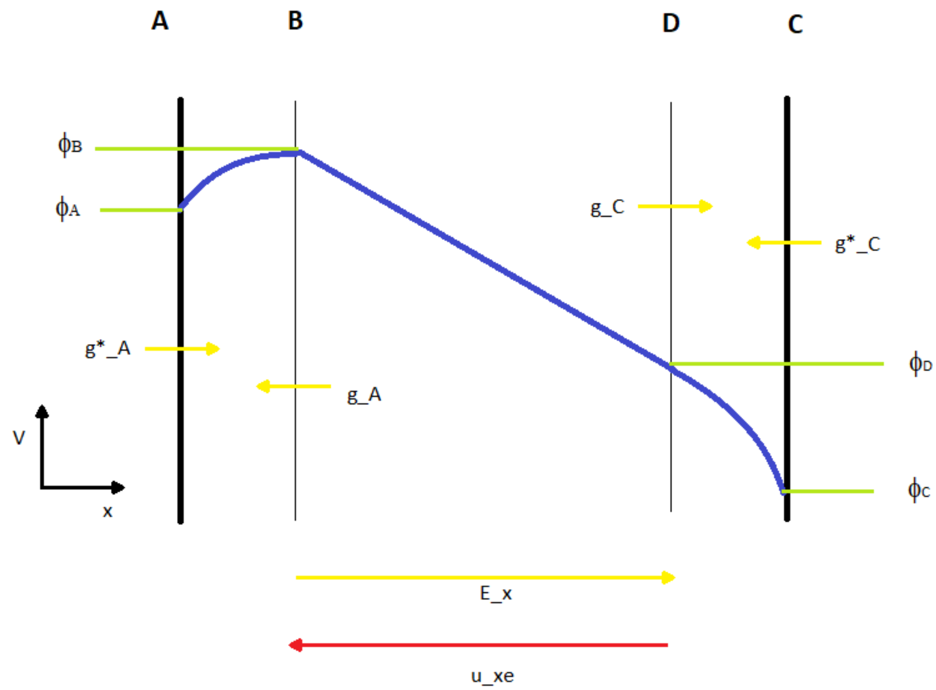


Figure 17: A graphic representation of the electron fluxes in equation 74. Left pointing arrows are negative values within the global axis while right pointing arrows are positive. The yellow arrows are quantities that are positive within the local axes of their respective equations[13]. Equation 74, and by consequence u_xe, are defined within the global axis. For the total electron flux $n_e u_{xe}$ to flow left, $u_{xe}$ needs to be negative, hence it is indicated in red here.

As we see from figure 17, one expects the sum of the left flowing fluxes (g_A and g*_C) to be larger than than the right flowing fluxes (g*_A and g_C). The potential drop in the D-C sheath is expected to be larger than the A-C sheath, as equation 10 indicates a larger negative sheath prevent more electrons from reaching the wall.

#### 3.4.4 f4: Charge continuity equation

This equation is derived by adding the electron and ion particle continuity equations:

$$n_{e0}\sqrt{\hat{T}_e/m_i} = \frac{g_{e,C} + g_{e,A} - g^\star_{e,C} - g^\star_{e,A}}{2} \tag{77}$$

This dependence is thus best summarized as:

$$0 = f_4(g^\star_{eA}, V_A, g^\star_{eC}, V_C) \tag{78}$$

#### 3.4.5 f5: Momentum balance equation

The electron momentum balance equation consists of three contributions: the electric field, magnetic field and collisional friction.

$$0 = -en_eE_x + en_eu_{zi}B_y + A_{xe} \tag{79}$$

[13]These are eq. 10 for g_A and g_C, eq. 65 for g*_A and g*_C, eq. 80 for E_x and eq. 74 for u_xe.

**Electric field and Magnetic field** The electric field in the plasma bulk is defined as the gradient of the potential drop between B and D in figure 16. Assuming that this gradient is constant in the transverse direction, it can be calculated as follows:

$$E_x = (\phi_B - \phi_D)/h \tag{80}$$

Where h is the distance between electrodes. Using the definitions of $\phi_B$ and $\phi_D$ given in section 3.4.1 and figure 16 this equation can be rewritten as follows:

$$E_x = (\phi_A - V_A - (\phi_C - V_C))/h \tag{81}$$

The magnetic field $B_y$ and axial speed $u_{zi}$ are calculated by the axial code. The magnetic field is calculated as follows:

$$\frac{\partial B_y}{\partial z} = en_e\mu_o(u_{xe} - u_{xi}) \tag{82}$$

**Particle collision term** The momentum transfer for electrons is calculated based on the particle collision rates $\nu_{ei}$, $\nu_{en}$ and differences between electron transverse velocity $u_{xe}$ and ion and neutral velocities $u_{xi}$,$u_{xn}$:

$$A_{xe} = m_e n_e \nu_{ei}(u_{xi} - u_{xe}) + m_e n_e \nu_{en}(u_{xn} - u_{xe}) \tag{83}$$

The ion and neutral particles are assumed to be immobile $u_{xi} = u_{xn} = 0$. The collision rate $\nu$ is calculated based on the thermal velocity of the particles $v_{th}$, the momentum transfer cross-section $\sigma$ and the density of the target particles $n_T$

$$\nu = v_{th}\sigma n_T \tag{84}$$

The 1D RMS equation is used for the thermal electron velocity $v_{th}$:

$$v_{th} = \sqrt{\hat{T}_e/m_e} \tag{85}$$

The neutral particle cross-section $\sigma_{en}$ can be approximated as $10^{-20}m^2$[73, p. 166], for the electron-ion collision rate $\nu_{ei}$ the following equation is used[73, p. 172][74][14]:

$$\nu_{ei} = \frac{2^{1/2}n_i Z^2 e^4 \ln(\Lambda)}{12\pi^{3/2}\varepsilon_0^2 m_e^{1/2}\hat{T}_e^{3/2}} \tag{86}$$

Summing this equation it becomes:

$$A_{xe} = u_{xe}m_e n_e\Big(\frac{2^{1/2}n_i Z^2 e^4 \ln(\Lambda)}{12\pi^{3/2}\varepsilon_0^2 m_e^{1/2}\hat{T}_e^{3/2}} + n_n\sqrt{\frac{\hat{T}_e}{m_e}}\cdot 10^{-20}\Big) \tag{87}$$

With $n_e = Z_i n_i = Z_i n_n \alpha/(1-\alpha)$. Where $Z_i$ is the effective ionization and $\alpha$ is the ionization degree. This leads to:

$$A_{xe} = u_{xe}m_e n_e^2\Big(\frac{2^{1/2}Z e^4 \ln(\Lambda)}{12\pi^{3/2}\varepsilon_0^2 m_e^{1/2}\hat{T}_e^{3/2}} + \frac{1-\alpha}{\alpha Z_i}\sqrt{\frac{\hat{T}_e}{m_e}}\cdot 10^{-20}\Big) \tag{88}$$

Plugging all of this into equation 79:

$$0 = -en_e\frac{\phi_A - V_A - (\phi_C - V_C)}{h} + en_e u_{zi}B_y - u_{xe}m_e n_e^2\Big(\frac{2^{1/2}Z e^4 \ln(\Lambda)}{12\pi^{3/2}\varepsilon_0^2 m_e^{1/2}\hat{T}_e^{3/2}} + \frac{1-\alpha}{\alpha Z_i}\sqrt{\frac{\hat{T}_e}{m_e}}\cdot 10^{-20}\Big) \tag{89}$$

Which as a shorthand will be written as:

$$0 = -en_e\frac{\phi_A - V_A - (\phi_C - V_C)}{h} + en_e u_{zi}B_y - u_{xe}m_e n_e^2 v_{th}(\sigma_{ei} + \sigma_{en}) \tag{90}$$

The dependency of this equation is described as:

$$0 = f_5(V_A, V_C, u_{xe}) \tag{91}$$

[14]The coulomb logarithm for electron ion collisions $\ln(\Lambda)$ is set to 10 using the equation $23 - \ln(n_e^{1/2}Z_i T_e^{-3/2})$, based on the assumption that $T_i m_e/m_i < T_e < 10Z^2 eV$ [65]

### 3.4.6 System of Equations

The previous section 3.4 discusses the five primary functions used to determine the model in figure 17. Of these function the electric field equation (f1) and the electron emission equation (f2) are applied twice: once for the cathode and once for the anode. Between f1 an f2 there is an implicit non linear relationship. TEE and FEE have a non-linear dependence on the electric field and vice versa. Hence this model is a set of seven equations with seven independent variables (table 6.)

For values of the electric field in the range of $10^6 - 10^8$ V/M , the influence of TEE and FEE is negligible and these latter two can be approximated as dependent variables. However when the electric field reaches $10^9$ V/M, this relationship becomes significant. Hence the emissions are assumed to be independent for now. In appendix B the equations are described in long form. Here below the 7 relevant equations are compacted in terms of independent variables:

**EoS 1:**

$$0 = -E_{w,C} + f_1(g^\star_{e,C}, V_C) \tag{92}$$

**EoS 2:**

$$0 = -g^\star_{e,C} + TEE(E_{W,C}) + FEE_C(E_{W,C}) + SEE \tag{93}$$

**EoS 3:**

$$0 = \frac{g^\star_{e,A} - g_{bolz}(V_A) - g^\star_{e,C} + g_{bolz}(V_C)}{2n_{e0}} - u_{xe} \tag{94}$$

**EoS 4:**

$$0 = \frac{-g^\star_{e,A} + g_{bolz}(V_A) - g^\star_{e,C} + g_{bolz}(V_C)}{2n_{e0}} - \sqrt{\hat{T}_e/m_i} \tag{95}$$

**EoS 5:**

$$0 = -g^\star_{e,A} + TEE(E_{W,A}) + FEE_C(E_{W,A}) + SEE \tag{96}$$

**EoS 6:**

$$0 = -E_{w,A} + f_1(g^\star_{e,A}, V_A) \tag{97}$$

**EoS 7:**

$$0 = -en_e\frac{\phi_A - V_A - (\phi_C - V_C)}{h} + en_e u_{zi} B_y - u_{xe} m_e n_e v_{th,e}(n_i\sigma_{ei} + n_n\sigma_{en}) \tag{98}$$

### 3.4.7 Initializing values

To start the simulation an initial guess of the output variables is needed to determine where the numerical algorithm starts its iterations. At first a guess is made for the sheath potential drop in a voltage free plasma:

$$\varphi_{sf} = 0.5\ln\left(2\pi\frac{m_e}{m_i}\left(1 + \frac{T_i}{T_e}\right)\right) \tag{99}$$

Assuming cold ions, this reduces to:

$$\varphi_{sf} = 0.5\ln\left(2\pi\frac{m_e}{m_i}\right) \tag{100}$$

Because there is a voltage bias over the plasma the following equation is used to determine $\varphi_A$:

$$\varphi_A = \ln\left(\frac{2\exp(\varphi_{sf})}{1 + \exp(e(\phi_C - \phi_A)/T_e)}\right) \tag{101}$$

This equation is based on the assumption that the sum of the sheath potential drops is equal to the voltage bias (applied by the external power source). When $(\phi_C - \phi_A) \to -\infty$ then $\varphi_C \to -\infty$ and $\varphi_A \to \varphi_{sf} + \ln 2$ as the electron current saturates and the cathode sheath takes up the non-anodic voltage drop.

Using this value a series of three iterations are used to calculate the electric field at the walls and the electron emissions.

The next step is to iterate over the sheaths. For each electrode this goes in the following sequence:

1. Assume $g^\star_e = 0$

2. Calculate $E_w$
3. Calculate $g_e^\star = TEE + SEE$
4. Calculate $E_w$ using this estimate
5. Calculate $g_e^\star = TEE + SEE + FEE$
6. Calculate $E_w$ using this estimate
7. Repeat steps 5 and 6 until convergence

Finally these values for $g_{e,C}^\star$ and $g_{e,A}^\star$ are used to make a guess for $u_{xe}$:

$$u_{xe} = \sqrt{T_e/m_i} + \frac{g_{e,A}^\star - g_{e,A}}{n_{e0}} = \frac{g_{e,C} - g_{e,C}^\star}{n_{e0}} - \sqrt{\hat{T}_e/m_i} \tag{102}$$

This equation is derived by adding equations 74 and 77.

# 4 Verification

In the context of CFD, verification aims to discern whether the computational model is a correct representation of the conceptual model[75]. Using guidelines provided by NASA's National Program for Applications-Oriented Research in CFD (NPARC)[15] and by Sandia National Labs[75], the current section will discuss the verification of the model. The implemented sub functions listed in table 7 were tested to eliminate bugs and coding errors. After this, the sub-functions were verified by comparing their outputs to literature sources describing analytical solutions or simulations from existing tools that have been validated. The system as a whole was verified by confirming iterative convergence (i.e. the residual of the solver decreases below a certain number of orders of magnitude). Fsolve has a default tolerance of $10^{-6}$. In this project $10^{-5}$ was chosen to allow for faster convergence without effecting the end result.

Table 8 displays the verification method of the different sub functions and the section in which they are discussed. Most sub functions where verified by comparison to analytical solutions in literature. The secondary electron emission, sheath to wall flux and electron collision equations were relatively trivial and are therefore discussed in the appendix A. The former is a linear function while the latter is a simple exponential. These were verified using a "sanity check" whereby the functions were plotted to confirm the expected linear/exponential behavior.

| Sub-functions | | Verification Method | section |
|---|---|---|---|
| SEE | Secondary Electron Emissions | Sanity check and literature comparison | A.2 |
| TEE | Thermal Electron Emissions | Literature comparison | 4.2 |
| FEE | Field Electron Emissions | Literature comparison | 4.3 |
| $E_w$ | Electric Field at the wall | Literature comparison | 4.4 |
| $g_e$ | Sheath to wall thermal electron | Sanity Check: plot variation against $n_{e0}, T_e, V$ | A.1 |
| $A_{xe}$ | Collisional electron momentum transfer | Literature comparison | 4.1 |

Table 8: Verification status for sub-functions

## 4.1 Momentum Transfer verification

A survey of six different literature sources on coulomb collision parameters found the following equation for the ion-electron collision rate [74]:

$$\nu_{ei} = \frac{2^{1/2} n_i Z^2 e^4 \ln(\Lambda)}{12\pi^{3/2}\varepsilon_0^2 m_e^{1/2} \hat{T}_e^{\,3/2}} \tag{103}$$

An alternative form is presented in the Naval Research Lab Plasma Formulary [65] under the assumptions $T_i \approx T_e$ and $Z_i = 1$:

$$\nu_e = 2.9 \cdot 10^{-6} n \ln(\Lambda) T_e^{-3/2} \quad [\text{Hz}] \tag{104}$$

Where $T_e$ is in eV and $n$ is in $cm^{-3}$.

Both equations were implemented in Matlab and delivered the same results. To verify the proper implementation of these equations in Matlab, comparison was done with Markusic and Choueiri's report on CSCX for the US Air Force[54]. When using the same input parameters as described in the CSCX report, the Matlab code delivered the same outputs as the report. The neutral ion collision rate is a linear term and was trivial to verify.

## 4.2 Thermionic Electron Emissions

First step in verifying the thermal electron equation (eq. 66) was done using a calculation example with the electrical field set to zero.[16] In this example the comparison was made with a Tungsten surface at 2400 K. After this a second comparison was done with a numerical example from the Handbook of Charged particle Optics[76, p. 3-5], for electric fields in the range of $10^8$ to $10^{10}$ V/m. This can be seen in figure 18. The graph calculated by this sub function corresponds to the literature example. One minor discrepancy is that the

[15] https://www.grc.nasa.gov/WWW/wind/valid/tutorial/overview.html
[16] From Encyclopedia Brittanica

literature example takes into account a tunneling current in the regime of $q = 1.656 \times 10^{-4} \frac{E_w^{3/4}}{T_w} \geq 0.3$ [76]. However for the baseline regime ($q \leq 0.3$)the plots correspond. For the scenarios discussed in the report, 1000 k is on the lower end of expected $T_w$ (section 5.2) while $10^8$ V/m is on the higher end of expected $E_W$ (discussed in sections 5.4, 5.5 and 6 ). Hence the highest q expected would be approximately 0.1656 and well within the baseline.

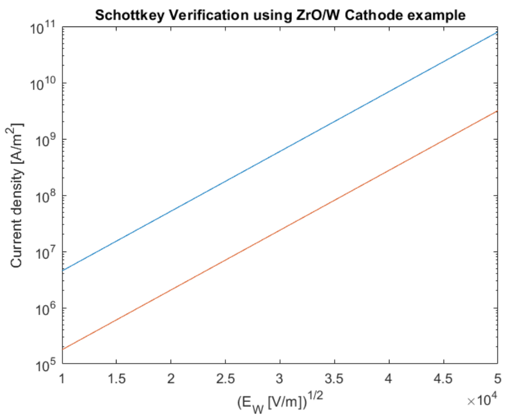


(a) Matlab Schottky calculations

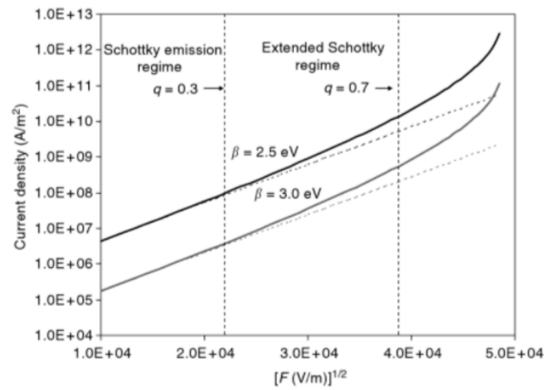


(b) literature example. F and $\beta$ represent the electric field $E_W$ and the work function in eV respectively[76]

Figure 18: TEE verification

### 4.3 Field Electron Emissions

According to literature the combined thermionic and field emissions effects[52][21][13][70] (also called thermo-field emissions) are dominant in arc-discharges. Murphy and Good[77] give some calculation examples for the thermo-field emissions (sum of TEE and FEE) using equations 68 and 66 in figures 19. The output of the functions implemented in this project (right) shows good correspondence with Murphy and Good's plot (left). At 300 K TEE is negligible. Hence this blue curve demonstrates the isolated FEE effect. The red and green curves in figure 19b represent the sum of the FEE and TEE fluxes at 1000 K and 1700 K respectively.

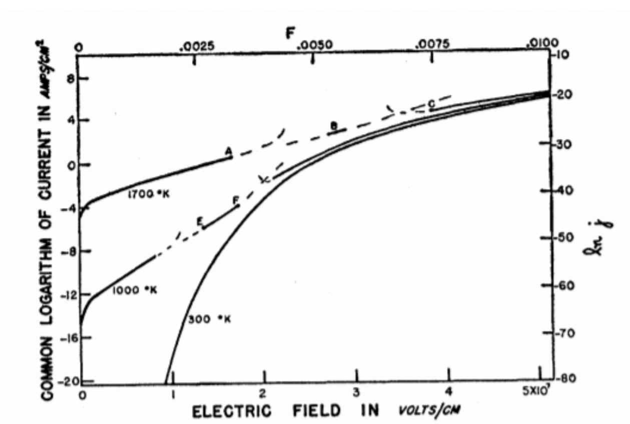


(a) From Murphy and Good[77]. The y axis on the left is the common logarithm of the current in $A/cm^2$. The x-axis is the electric field in $10^7$ V/cm.

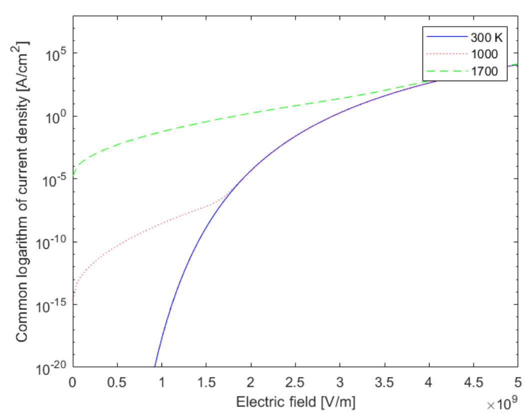


(b) Verification of thermo-field emission equations implemented in code.

Figure 19: Thermo-field emissions equations verification, for $A_G = 120$ A cm$^{-2}$k$^{-2}$, $P_F = 1$, $W = 4.5eV$.

## 4.4 Wall Electric Field

The equation for the electric field at the wall employed in this model (eq. 63) is a standard derivation[52][5]. As mentioned in sections 3.1 and 3, the ions have been assumed to be cold and the sheath has been assumed to be collisionless. The ions enter at a velocity equal to the Bohm speed (eq. 4). One deviation from the derivation presented in [52][5], is that the influence of electron emissions on the space charge at the wall are taken into account. For comparison a 1-D model of an argon plasma by Javidi Shirvan et al.[12] was used. The electron density, electron temperature, cathode wall temperature were extracted from plot figures in Javidi's work using a python script[17]. This data was used as input for the current model to calculate the electric field. The results of this are compared with Javidi's work in figure 20

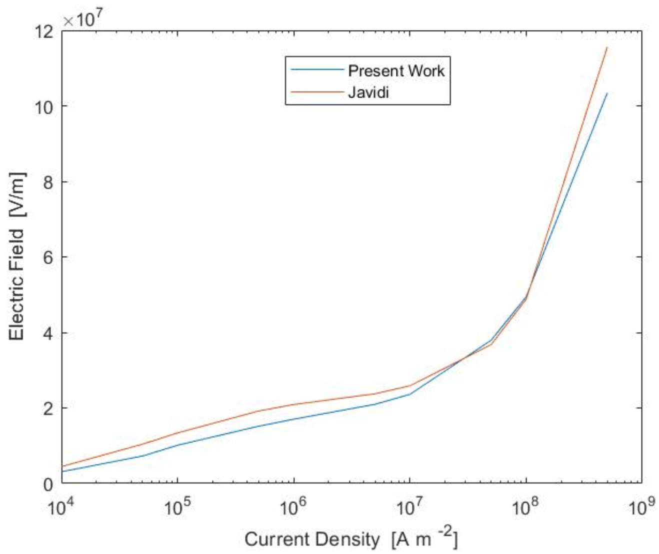


Figure 20: Comparison of cathode field magnitude calculated by equations used in this project and those used by Javidi Shirvan et al.[12]

One sees a corresponding trend between the two results. Electric field increases with current density as both electron density and electron temperature increases. However at the lower current densities ($j \leq 10^6\mathrm{A/m^{-2}}$), this increase is more subtle. At higher current densities there is good correspondence between the outputs of both equation, less than 10% deviation. At lower current densities the difference is in the 15 to 20% range. Javidi Shirvan et al. use the generalized formulation developped by Riemann[78]. The ions in this model can have a non negligible thermal velocity when entering the presheath and are thus accelerated to velocities higher than the Bohm velocity[13]. Thus altering the ion distribution in the sheath and as a result the space charge. However the minor differences between both curves is largely the result of inaccuracies in the data extracted from the source material. Calculations using Javidi Shirvan's equation for the electric field rendered a curve that was closer to the present work than Javidi's results.

The impact of the emitted electrons on this electric field near the wall was found to be negligible. For the tested conditions in the PPT model (cathode temperature = 700 K, $T_e = 3eV$, $n \leq 10^{24}m^{-23}$, $2 \leq \varphi \leq 1000$), the influence of the second term, of equation 63, is less than 1% of the total $E_W$ value. However cathode temperatures may be far higher. For higher temperatures such as 2500 K or 3000 K the effect of these emissions remain similarly negligible according to the equation provided above. Modelling by Shirvan also confirms that the influence of the emitted electrons on the space charge near the wall is negligible[13]. Hence this second term can be dropped, rendering:

$$E_{w,C} = \sqrt{\frac{2n_{e0}\hat{T}_e}{\varepsilon_0}}\Big[\exp(\varphi_{w,C}) - 1 + M_{i0}^2\big[\Big(1 - 2\frac{\varphi_{w,C}}{M_{i0}^2}\Big)^{1/2} - 1)\big]\Big]^{1/2} \tag{105}$$

[17] WebPlotDigitizer by Ankit Rohatgi

## 4.5 Summary

The equations that have been implemented in the model code were verified by comparing them individually to literature sources. The momentum transfer equation was compared to calculations by Markusic[51] (section 4.1). The thermionic emissions equations was compared to numerical examples from the handbook of Charged Optics[76] and deemed valid for range of electric field values that are expected in PPTs (section 4.2). The field electron emissions were compared to fundamental research by Murphy and Good[77], which had calculations for the combined thermionic and field emissions (section 4.3). For all of the previous equations, a perfect correspondence was found between the Matlab code results and the literature data.

For the equation of the electric equation at the wall however, some slight deviations in results was found with the source material (section 4.4). In this case, data was taken from arc welding modelling preformed by Javidi Shirvan which employed slightly different equations[14]. The difference in the result is caused by the inaccuracy of extracting data from plots. This was confirmed by implementing the equations used by Javidi, which produced results more similar to this models simulations. All in all this verification step showed that the influence of emitted electrons on the electric field strength are negligible. Hence equation 63 can be simplified to 105.

# 5 Validation

Validation determines to what degree the model is an accurate representation of the real world problem[75]. For this model it was done in three phases. First the model was tested to see whether certain physical mechanisms taken that were included in the model had a significant effect on the output. For example, as mentioned in section 3.4.1, the influence of electron emissions on the electric field at the electrode surface are negligible. Similarly the electron-neutral friction force included in the momentum transfer equation can also be neglected. The electron-neutral collision frequency is small compared to the electron-ion collision rate for ionization degrees higher than $10^{-3}$. The momentum balance describes physically sound behaviour when the magnetic field term is excluded. The effect of including the magnetic field term is discussed in section 5.1.

The PPT literature, that had been surveyed for this project, did not report values for the cathode wall temperature. As demonstrated in the previous section, this parameter can have a significant effect on the thermionic emissions flux. Testing different assumptions of this temperature was therefore imperative. Initially a wall temperature of 700-1000 K was assumed as this were the values reported for Teflon temperature during operation[30]. Under this assumption initial calculations showed FEE and TEE were negligible in comparison to SEE. These results are discussed in section 5.2. This contradicts what literature says about arc discharges[52][21]. For glow discharges (low pressure and current, high voltage) SEE is dominant. For thermal arc discharges (high current, low voltage) the thermionic and field emissions are dominant. To remedy this, comparisons with other models that examined the boundary coupling of a plasma with the walls was needed. A test case was selected from thermal arc welding literature. These simulations go into more detail on the plasma boundary conditions than PPT data. This second phase of validation is discussed in section 5.3. After improving the assumptions of this mode, comparison was done with PPT benchmark cases in the final validation phase. Two selected benchmarks experiments, CSCX[54] and ADD-Simplex[4][42] are discussed in sections 5.4 and 5.5 respectively.

## 5.1 Momentum Equation: Magnetic field Assumptions

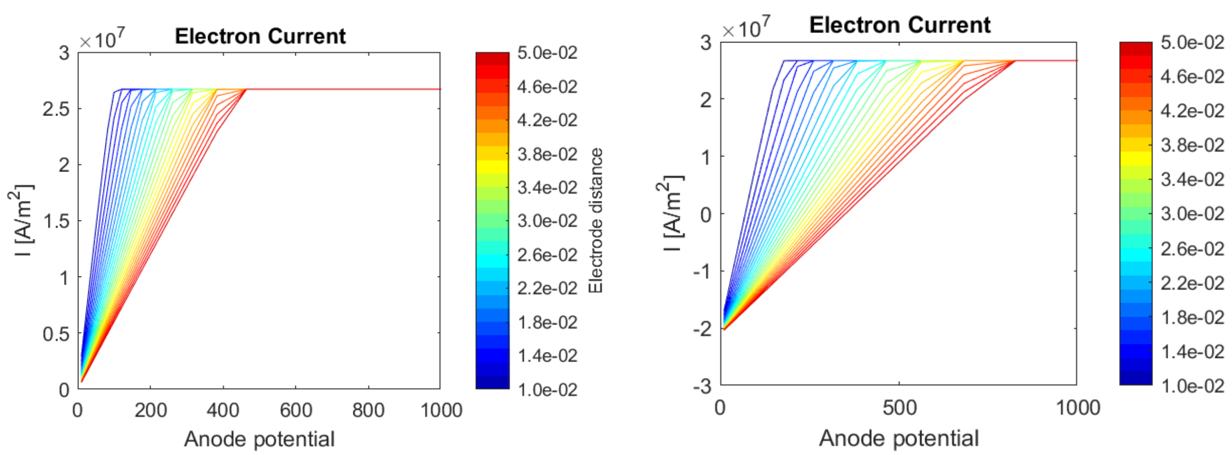


(a) $B_y = 0\,T$ (b) $B_y = 0.7$

Figure 21: Initial estimates for the effect of Electrode distance (h) and anode potential on Electron current. The magnetic field behaves as an externally applied magnetic field. $n_e = 10^{22}\,m^{-3}$, $T_e = 2.5\,eV$

First a set of calculations were done while assuming no magnetic field. Figure 21a shoes the influence of distance and anode potential on current. As expected a higher anode potential leads to higher current. Smaller inter-electrode distance also increases the current in this model because the electric field in the bulk is stronger and electrical resistance scales with plasma resistivity and distance. However at a certain potential level, the current saturates in because insufficient electrons are provided at the cathode end. Adding thermionic emissions to the model alleviates this, which will be discussed in sections 6.2 and 6.3.

Adding a constant magnetic field term downshifts the curves as seen in figure 21b. In other words this means a current reversal for low potential. This is not what one would expect in the PPT. In the current model, the magnetic field is uncoupled from the current, essentially simulating an externally applied magnetic field. While in a PPT the magnetic field is self-induced.

In the future coupled model, this would be resolved as the magnetic field would be calculated by integrating the transverse current values. For the purpose of simulating the transverse model in isolation, a rough estimate of the magnetic field strength induced by the current can be calculated. As stated in section 2.1, according to the slug model the Lorentz force acting on the plasma sheet is calculated in the following way[9]:

$$F_d = \iiint_V \mathbf{J} \times \mathbf{B} \, dV = \frac{1}{2} L' \mathbf{I}^2 \tag{106}$$

Assuming that the current and magnetic field are constant and unidirectional throughout the thin plasma sheet with width $w$, height $h$ and thickness $\delta$, the force density $f_d$ can be estimated as:

$$f_d = J_x B_y = \frac{1}{2} L' J_x^2 \frac{w\delta}{h} \tag{107}$$

Where $B_z$ is estimated as (ion current assumed negligible):

$$B_y = \frac{1}{2} L' J_x \frac{w\delta}{h} \approx -\frac{1}{2} \mu_0 e n_e u_{xe} \delta \tag{108}$$

Insert this into equation 79:

$$0 = -en_e \frac{\phi_A - V_A - (\phi_C - V_C)}{h} - \frac{1}{2}\mu_0 (en_e)^2 u_{zi} u_{xe} \delta - u_{xe} m_e n_e v_{th,e} (n_i \sigma_{ei} + n_n \sigma_{en}) \tag{109}$$

For the same parameters listed in figures 21a and 21b this gives:

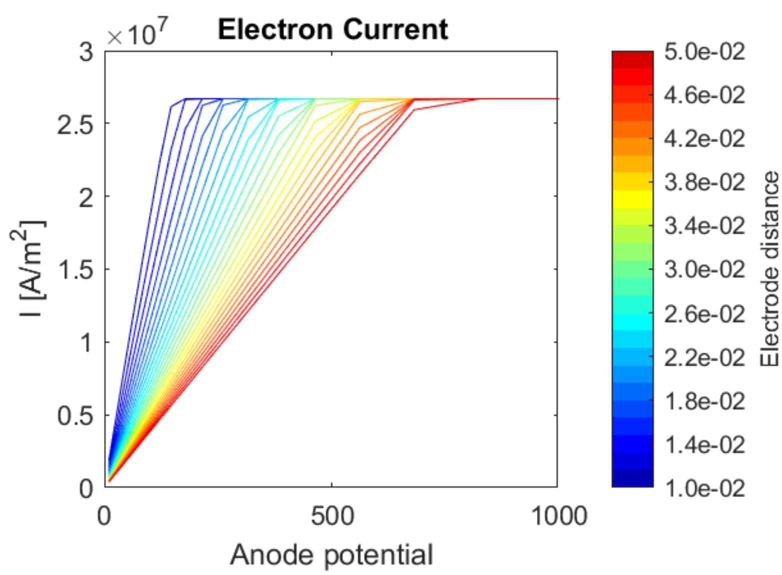


Figure 22: The effect of Electrode distance (h) and anode potential on Electron current with the magnetic field estimated using equation 108. $n_e = 10^{22}\, m^{-3}$, $T_e = 2.5\, eV$

With the new method of estimating the magnetic field based on current density, no current reversal occurs at lower potentials. The magnetic field term behaves as an extra resistance to the current, adding an extra feedback to the system. Compared to figure 21a, current density rises slower with increasing potential, indicating that the simulated self induced field acts as a load. Using this estimation method, the magnetic field strength is linear proportional to the current (albeit negative). The maximum magnetic field seen in this figure is 0.5 T which is in the order of magnitude of the maximum magnetic field values measured in literature [47][27][50].

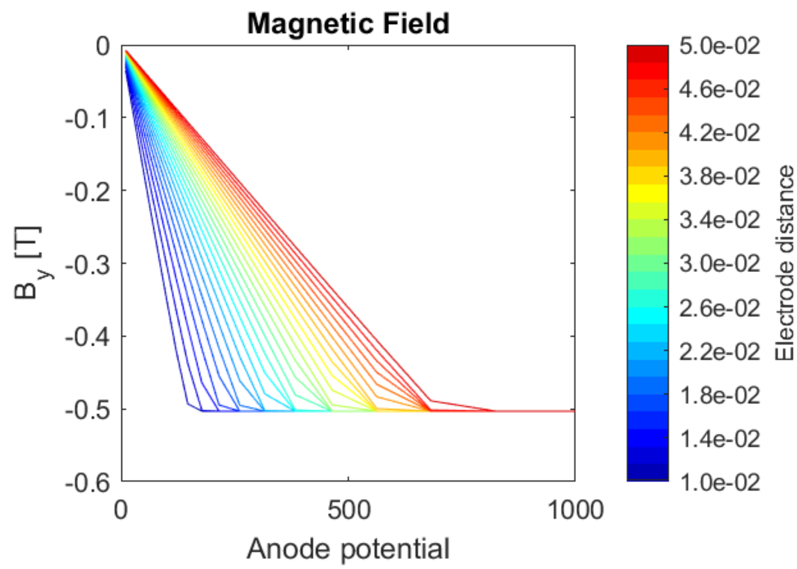


Figure 23: Magnetic field estimated using equation 108

## 5.2 Electron Emissions: Cathode Wall Temperature Assumptions

According to literature for thermal arc discharges, as found in a PPT, the secondary electron emissions are negligible compared to thermo-field emissions [52][21][13][13]. Figure 24 presents initial simulation results of this model for the assumed electrode temperature ($\leq$1000 K). This assumption was made because Teflon propellant block reaches a temperature between 700 and 1000 K during ablation [30].

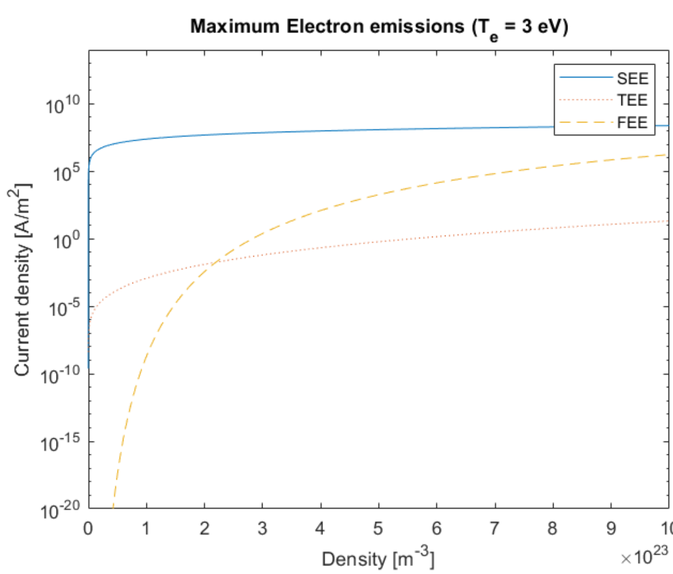


Figure 24: Comparison of maximum expected TEE and FEE with minimum expected SEE, for hydrogen propellant and copper electrode at a temperature of 1000 K.

Field electron emissions become relevant at wall electric fields higher than $10^8$ V/m[52]. The PPT cathodes do attain such fields when the density approaches $10^{24}$ m$^{-3}$. However the SEE flux is still several orders higher in that case. This can be seen in figure 24, which shows the maximum FEE and TEE compared with the minimum SEE expected for sheath voltages between 1 and 2000 $e \cdot V/\hat{T}_e$, a wall temperature of 1000 K, a work function of 4 eV and an FEE exponential correction factor of 0.7. The propellant in this simulation is hydrogen with an ionization energy of 13.6 eV. It should be noted that $10^{24} m^{-3}$ is the higher end of electron density that one would expect in the PPT. Hence one can assume that FEE is negligible for a PPT. For these initial temperature assumptions, the calculated TEE flux is negligible compared to SEE. This contradicts thermal arc discharge literature, which states that the TEE is significantly higher than SEE[52]. Hence the cathode temperature must be higher than the previously assumed 1000 K.

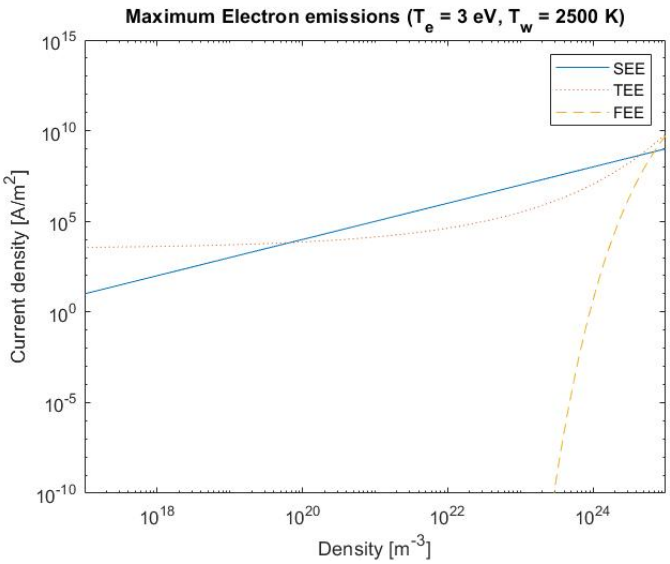


Figure 25: Comparisons of emissions at a wall temperature of 2500 K

Figure 25 compares the different emission mechanism fluxes for a cathode wall temperature of 2500 K. Here SEE remains the dominant emissions mechanism throughout the expected electron density range. Only at the highest densities above $10^{24}$ $\mathrm{m}^{-3}$ do the thermo-field emissions over take SEE. TEE really starts to dominate at higher temperatures than 3000 K[52], as can be seen figure 26. This is below the melting point of tungsten but exceeds the boiling point of copper. In cathode spots, the local temperature exceeds 3000 K. At these small short lived spots, metal evaporates and provides electrons for current [52][28]. These spots have not been included in this projects model and may explain the discrepancy between current results and literature. Extensive modelling on cathode spots in PPT's has been performed by Shaw in 2011[28].

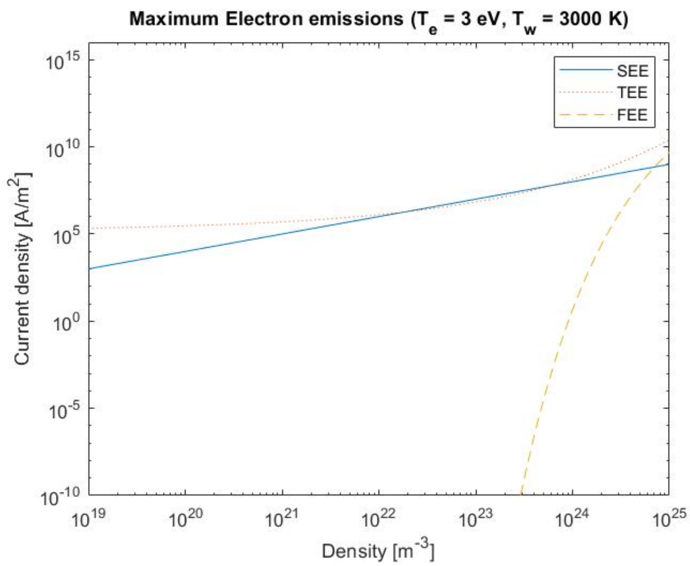


Figure 26: Comparisons of emissions at a wall temperature of 3000 K

However, even at 3000 K SEE and TEE appear to be of the same order for the densities that one expects in an arc discharge ($10^{21}m^{-3} - 10^{24}m^{-3}$). The ratio of SEE to ion flux is approximately 0.01 electrons per ion, while Fridmann predicts the ratio for TEE to the ion flux to be in the range of 2-9 emitted electrons per incident ions[52, p. 515 -516]. TEE is thus 2 to 3 orders of magnitude higher than SEE. The cathode wall temperatures must be higher than previously assumed to achieve this ratio. It should be noted that the cathode temperature does not affect FEE, which is demonstrably negligible when compared to TEE in figure 26.

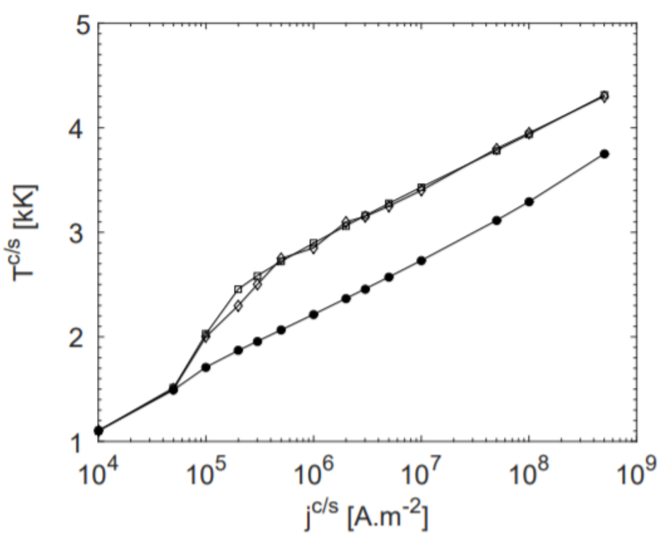


Figure 27: From Shirvan[13]: "Cathode surface temperature as functions of the current density at the cathode surface. (•) thoriated tungsten, (▫) tungsten"

PPT literature does not give estimates on electrode temperatures but one can take a look at welding literature for an indication. Figure 27 shows the relationship between cathode temperature and electron density for a tungsten welding tip [14]. Welding literature will be discussed in more detail in the next section.

Given that the PPT benchmarks have currents in the KA ampere regime and surface area's are in the orders of $cm^2$, one could expect the current density to reach a range of $10^7 - 10^8 A/m^2$. For non-thoriated tungsten the cathode temperatures exceed 3200 K. As TEE increases exponentially with temperature, it should be an order of magnitude larger than what is shown in figure 26.

Furthermore as electron density and current density correlate[42], higher wall temperatures also correlate with higher electron densities. A thermal element model should be implemented to predict the wall temperatures. With the inclusion of a thermal balance equations the current density to electron density plots would look different from what is presented in figures 25 and 26 because the cathode wall temperature and electrode density both change with the current density instead of the wall temperature being constant[12]. Given the added complexity of such a model, it has been opted to simply assume higher temperature levels and investigate whether these converge. In sections 5.4 and 5.5, simulations are performed for several assumptions of cathode temperatures in the range of 3000 to 4000 K.

It should be noted that for copper cathode, the expected temperatures would likely be higher as copper's heat capacities are lower. This electron current concentrates in the cathode spots, which evaporate and keeps the rest of the cathode relatively cool. For the current work, the cathode spots effect will be neglected and the erosion of electrodes is assumed to be negligible. Copper and tungsten have the same work function, it will thus be assumed a copper cathode will emit the same thermionic electrons flux as a tungsten cathode of the same temperature.

### 5.3 Test Case 1: Thermal Arc Welding literature

PPT modelling efforts place little emphasis on the effect of electron emissions mechanisms on sheath interactions. To validate the sheath components of this model, a comparison will be done with the work of Javidi Shirvan et al. on Gas Tungsten Arc Welding (GTAW)[12]. GTAW is a welding process whereby a Tungsten cathode produces a thermal arc discharge while shielded by an inert gas such as Argon. The plasma arc heats the material that is to be welded and smelts pieces together. Javidi Shirvan had reviewed the modeling on Cathode Arc-coupling modelling in GTAW[22]. These are models that provide self consistent calculations of temperature and density in the plasma bulk coupled to the conditions in the cathode sheath, rather than prescribing the latter. The equations employed by Javidi Shirvan et al. are largely similar to the equations employed in the current work[14]. With the exception that ions are assumed to be cold in the current work. This leads to a deviation in the electric field equation.

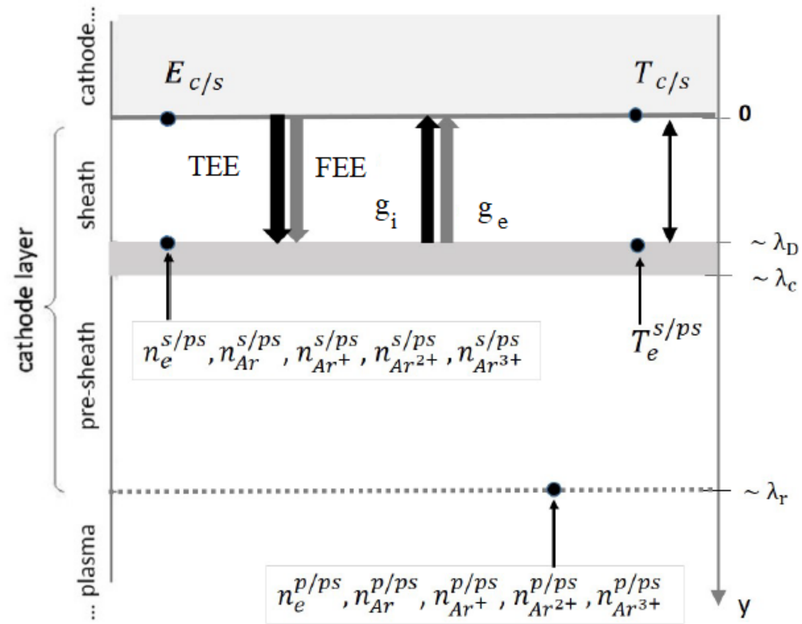


Figure 28: Cathode layer model. Schematic adapted from Javid et al.[14]

The experimental literature that Javidi Shirvan had surveyed examined two alloys for the welding cathode. The first one is pure tungsten which is characterised by a high melting temperature $T_m = 3653K$ and evaporation temperature $T_v = 6203K$. The work function $W$ and Richardson constant for tungsten are approximately the same as the corresponding values for copper. The second alloy is doped with 2% wt of Thorium-Oxide ($ThO_2$), which is characterised by a lower work function. One sees in figure 27, that the thoriated tungsten cathode is characterised by a lower temperature in comparison to pure tungsten at the same cathode current density. This is partially due to more thermionic electron emissions as a result of the lower work function [13]. The material properties of tungsten and $ThO_2$ are summarised in table 9.

| | W | $ThO_2$ | Cu |
|---|---|---|---|
| $W$ [eV] | 4.5 | 2.6 | 4.4 |
| $A_G$ [$10^4$Am$^{-2}$K$^{-2}$] | 80 | 3 | 80 |
| $T_m$[K] | 3653 | 3323 | 1357.8 |
| $T_v$ [K] | 6203 | 4670 | 3200 |

Table 9: Properties of thermionic cathode emitters adapted from[22][21]

A comparison with 1-D model results is done to see if differences in assumptions and equations between the current work and Javidi Shirvan et al. lead to significantly different results. Using data on cathode temperature, electron density and sheath potential drop, results were produced for the sheath emissions. Figures 29a and 29b show the electron density and temperature parameters taken from Javidi Shirvan et al.[13][12] for validating this model. The cathode temperature is taken from figure 27. The wall electric field values calculated by Javidi Shirvan (figure 20) are used. The x-axis of these plots, the current density, can be compared to the output of this projects' model.

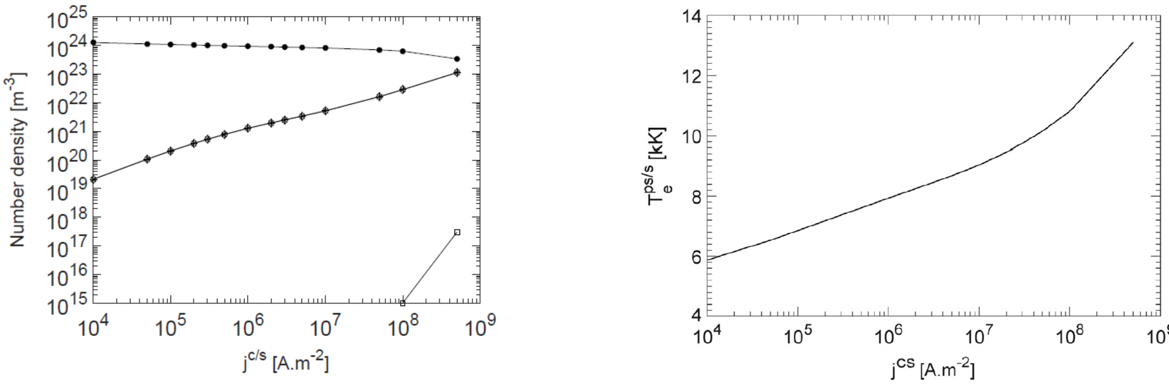


(a) Electron and argon density for an Argon Plasma: $n_{Ar}$ ($\bullet$), $n_e$ ($\diamond$), $n_{Ar^+}$ ($\star$), $n_{Ar^{2+}}$ ($\square$) [13]

(b) Electron temperature at the pre sheath - plasma sheath interface.[12]

Figure 29: Input values test cases

A first step is to take a look at the particle flux levels at the cathode, ignoring the coupling equations mass, momentum and charge conservation). For a thoriated tungsten cathode and argon plasma the calculated particle fluxes for both models show a general agreement in trends (figure 30. For lower current densities, Javidi et al. use a different more complicated equation for calculating the thermionic emissions[12][77]. The output of this equation converges with the Schottkey equation for $j \geq 10^5$. For the ion flux (eq. 9), cathode thermionic electron emissions (eq. 66) and electron sheath-to wall flux (eq. 40) (or "back diffusion flux") both models show good correspondence (figure 30). The current results show TEE to be at least two orders of magnitude higher than SEE in contrast to the results of the previous section where the two were within the same order. This is a better representation of the expectations put forward by literature that SEE is relatively negligible. In the results presented here and in section 5.2, FEE is demonstrable negligible for the parameters considered.

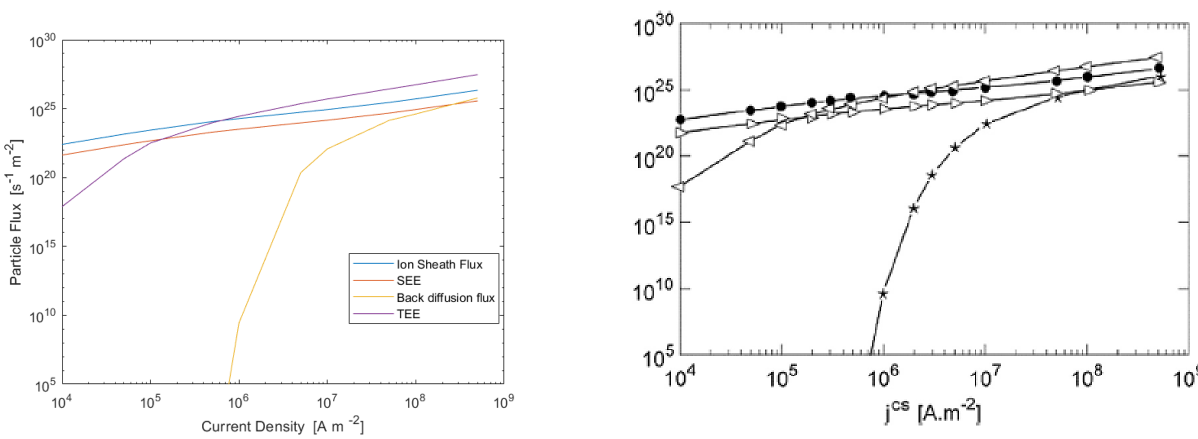


(a) Sheath particle fluxes in $s^{-1}m^{-2}$ calculated used equations in current work

(b) Sheath particle fluxes in $s^{-1}m^{-2}$ calculated by Javidi Shirvan et al.[12]: ion flux ($\bullet$), SEE ($\triangleright$), TEE ($\triangleleft$), back diffusion flux ($\star$)

Figure 30: Comparison of current model results and Javidi et al.[12] for thoriated tungsten.

Next step is to validate the full model, whereby all equations are coupled. For a comparison of the full model, several candidate validation cases such as the work of Javidi[79], Sansonnens [80], Baeva [81] and Haider [82]. All of these selected cases were modelling or experimental efforts using a similar setup. A tungsten cathode with a sharp tip is brought at about 5 mm from a flat anode surface while an argon plasma carries the current between the two. The cathode is either made from pure tungsten or thoriated tungsten. The total current is varied between 50 and 200 A. However the voltage stays between 5 and 15 V according to Haider's experimental measurements [82]. The higher current levels correspond to higher cathode temperatures.

| Design Parameters | | Tungsten | Thoriated Tungsten | unit |
|---|---|---|---|---|
| $h$ | distance between electrodes | 0.005 | 0.005 | m |
| $m_i$ | Ion mass (Ar) | 40 | 40 | $m_p$ |
| $W$ | Work function | 4.5 | 2.6 | eV |
| $\mathcal{E}_i$ | Ionization energy (H) | 15.76 | 15.76 | eV |
| $A_G$ | Material Schottky constant | 80 | 3 | $10^4 \mathrm{Am}^{-2}\mathrm{K}^{-2}$ |

Table 10: GTAW test paramters Ion mass is expressed in terms of proton mass $m_p$ or $1.672 \cdot 10^{-27}$ kg

The plasma Temperature is in the range of 1-2 eV and the density is in the order of $10^{22}$ to $10^{23}$ $\mathrm{m}^{-3}$. Along side with other simulation results from these studies, these parameters are presented in table 11.

| Externally Set Parameters | | test set 7[79] | test set 8[79] | test set 9[79] | Sansonnens[80] | unit |
|---|---|---|---|---|---|---|
| $T_p$ | Bulk electron temperature | 1.3 | 1.6 | 2.8 | 1.29 | eV |
| $T_{ps/s}$ | Sheath electron temperature | 0.85 | 0.89 | 1.08 | 1.9 | eV |
| $n_e$ | electron density at sheath edge | 2.5 | 4 | 16.5 | 17-20 | $10^{22}m^{-3}$ |
| $n_e$ | electron density in bulk | | | | 20 | $10^{22}m^{-3}$ |
| $\phi_A$ | Anode voltage[82] | 10-15 | | 15 | 0 | V |
| $\phi_C$ | Cathode voltage | 0 | 0 | 0 | -10 | V |
| $u_s$ | Pre-Sheath Potential drop | 0.3- 0.6 | | | | V |
| $T_{w,C}$ | Cathode Wall Temperature | 3075 | 3250 | 3600 | 4000 | K |
| Output | | | | | | |
| $j$ | Current density | 3.5 | 6.5 | 3.5 | | $10^7\mathrm{A/m}^2$ |
| $u_C$ | Cathode Sheath Potential drop | 4.6 | 4.8 | 6.4 | 4 | V |
| $u_A$ | Anode Sheath Potential drop[80] | | | | 2 | V |
| $I_A$ | Total current | 100 | 200 | 100 | 200 | A |

Table 11: Externally determined input variables GTAW

Unfortunately the solver did not resolve when taking these parameters as inputs. The solver isn't able to converge when the distance between the electrodes are small ($< 0.03$ m). The residual for the force balance equation remains quite high in such cases. The inability to converge for these inputs is likely due to a difference in simulation geometry. In the PPT model, the assumption is made that the electron flux density in the vicinity of the cathode is the same as the density near the anode. By contrast, in the welding set up, the plasma can diverge radially. The current attachment is larger at the anode than at the cathode and as a consequence the anode current density is possibly lower than the cathode current density.

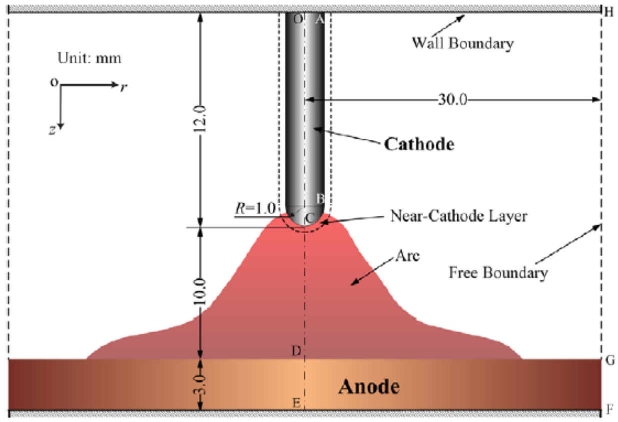


Figure 31: Diagram of a GTAW discharge [15].

The full transverse-model hereby remains invalidated. However the sub-functions for the ion flux, back-diffusion flux, secondary electron emissions and thermionic emissions where validated as shown in figure 30. It has been shown that TEE is far larger than SEE under the right temperature assumptions, which had been an open question in the previous section. What no remains to be shown is that the coupled equations in the transverse model give results that correspond to literature. For this end, two new validation test cases, taken from PPT literature, will be discussed in the next to sections. PPT literature does not provide data on cathode temperature and individual emission mechanisms (SEE and TEE), but does provide for data on current density, voltage, electron density and temperature.

### 5.4 Test Case 2: Current Sheet Canting Experiment (CSCX)

The CSCX was a gas-fed PPT experiment aimed to study the current sheet behavior when acceleration is dominated by electro-magnetic forces[54]. The device is relatively large for a PPT with a length of 60 cm and a width of 15 cm. The distance between the parallel copper electrodes is 5 cm. Temperature and density data was collected though high-speed photography, laser interferometry, emission spectroscopy and magnetic probe measurements. A differential voltage probe measured the plasma (terminal) voltage. Terminal voltage specifically contains only the sheath potential drop and bulk plasma resistance. The magnetic flux of the circuit is largely concentrated behind the current sheet and mostly absent at the front. Hence the probe does not detect the voltage load caused by the the self-induced magnetic field. [16]

Experiments were performed with seven gaseous propellants (i.a.: hydrogen, krypton, argon and xenon) fed in at three different pressures: 75 mTorr (10 Pa), 200 mTorr (27 Pa) and 400 mTorr (53 Pa). The discharge was powered by a pulse forming network that was powered to 9 KV. At the start of the discharge, a high voltage spike is measured in the plasma as the gas breaks down. After this initial transient, the terminal voltage experiences a relatively steady increase as the plasma propagates downstream.

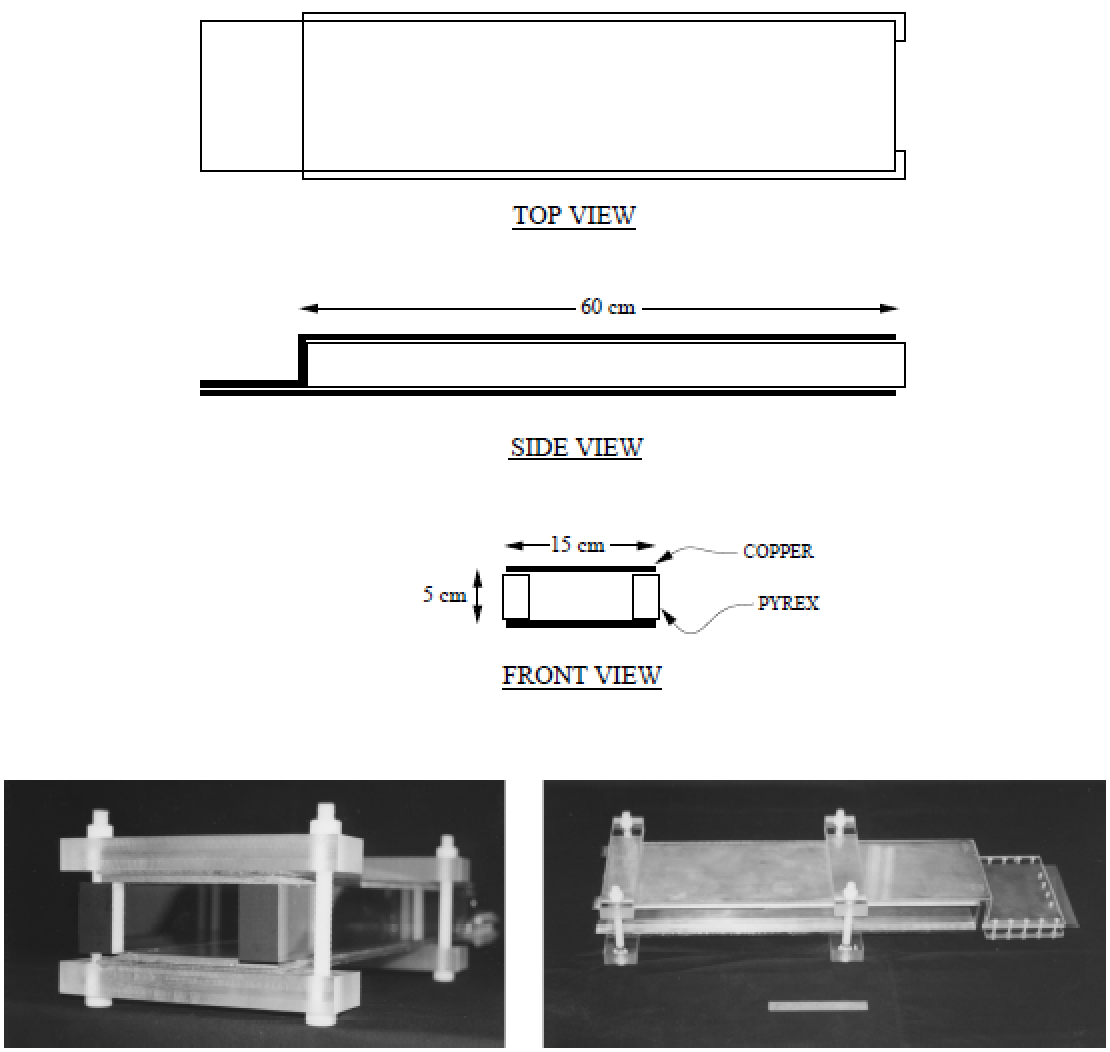


Figure 32: CSCX experimental thruster[16]

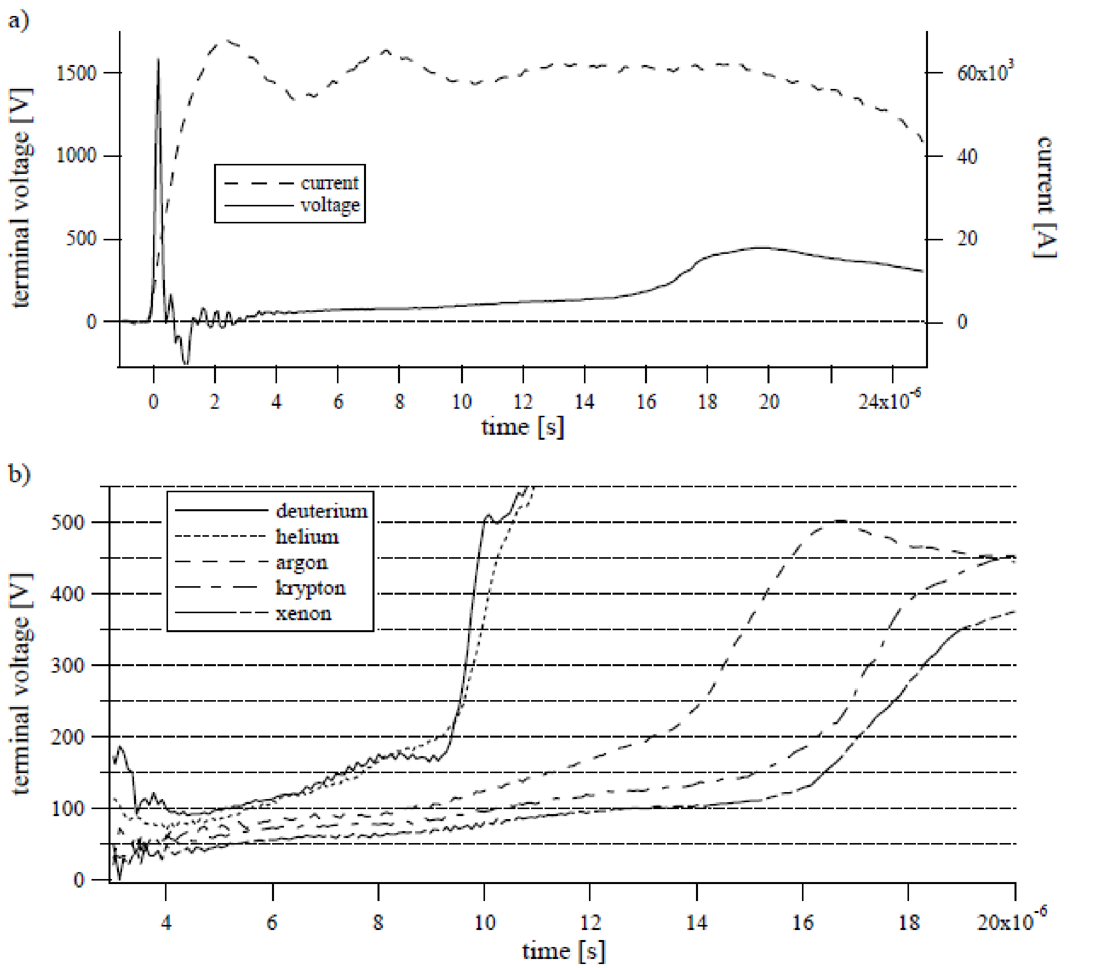


Figure 33: Terminal voltage (sheath and plasma bulk voltage, inductive load is excluded) measurements for propellant feed pressure of 75 mTorr. a) terminal voltage and plasma current measurement krypton discharge. b) Terminal voltage measurements for several different propellants excluding the initial voltage spike. [16]

The measured peak and average currents varied depending on the propellant and pressure applied. A higher total propellant mass (proportional to feed pressure) as well as a higher mass were associated with higher current levels. This is because the dynamic impedance (voltage drop associated with $IdL/dt$) dominates over ohmic resistance. Hence the current is largely tied to current sheet propagation speed. The inertia of the ambient gas, slows down the current sheet as it moves downstream. Lower current sheet speeds were measured for higher propellant masses. Inversely, higher current levels were measured, as can be seen in figure 34.

Plasma (ohmic) resistivity is assumed not to vary much as a result of propellant choice. Resistivity is proportional to electron temperature ($\eta \propto T_e^{-3/2}$)[8]. The study by Markusic was only able to determine statistically significant measurements of electron temperature for experiments with Argon. For the analysis of the other propellants, the same value of 2.4 eV was assumed.

Interferometry data provided time resolved results for the maximum electron density. For 75 mTorr, the density peaks at 2-3 $10^{22}\mathrm{m}^{-3}$ and decreases as the current sheet propagates down stream. A sheet thickness $\delta$ was defined by the Full-Width-Half-Maximum of the measurements. It was generally on the order of 1 cm. Together with an assumed width of 10 cm, this can be used to estimate current density based on total current measurements.

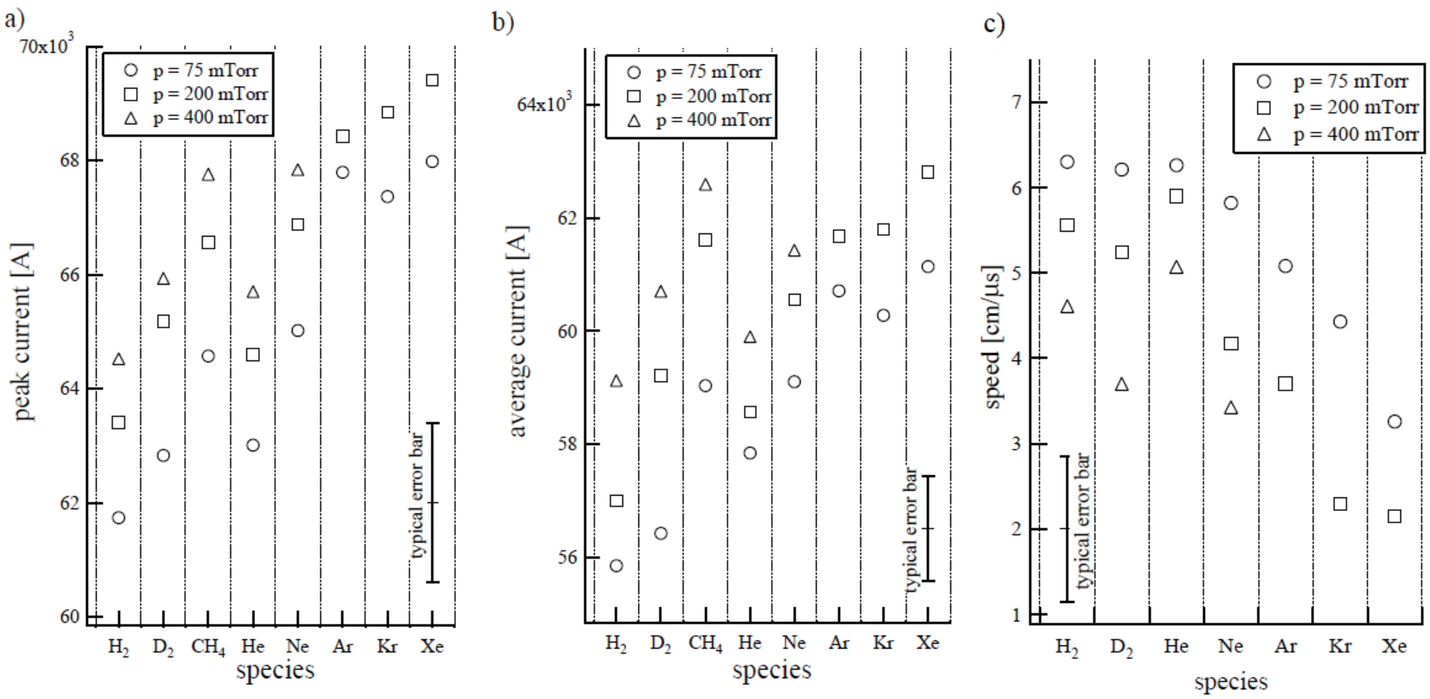


Figure 34: Influence of propellant mass and pressure on a) peak current b) average current c) current sheet propagation speed[16]

Time resolved measurements of magnetic field would either provide a small negative or magnet field in front of the advancing sheet. Rapidly increasing to a maximum field of 0.3 T behind the sheet for most propellants. For some combinations of propellant and pressure a slightly higher magnetic field of 0.4 T was detected.

Two data sets from Markusic's experiments are used to validate the model in the current work. Hydrogen would be used for its relative simplicity. But given that the terminal voltage measurement hasn't been reported, the data set for deuterium will be used instead. The second data-set used will be Argon, as this is the only propellant for which the electron temperature measurements are certain. The design data of the CSCX including propellant properties is summarised in table 12.

| Design Parameters | | CSCX | unit |
|---|---|---|---|
| $h$ | distance between electrodes | 0.05 | m |
| $L$ | Length of electrodes | 0.8 | m |
| $m_i$ | Ion mass (D) | 2 | $m_p$ |
| $m_i$ | Ion mass (Ar) | 40 | $m_p$ |
| $W$ | Work function (Cu) | 4.4 | eV |
| $\mathcal{E}_i$ | Ionization energy (H/D) | 13.6 | eV |
| $\mathcal{E}_i$ | Ionization energy (Ar) | 15.75 | eV |
| $A_G$ | Material Schottky constant | 80 | $10^4 \mathrm{Am}^{-2}\mathrm{K}^{-2}$ |

Table 12: Design and material parameters for the CSCX experiments[16]. Ion mass is expressed in terms of proton mass $m_p$ or $1.672 \cdot 10^{-27}$ kg. Material properties are indicated with the corresponding elements: Deuterium (D), Argon (Ar), Copper (Cu), Hydrogen (H).

Cathode wall temperature was not measured by Markusic et al. A guess on the cathode wall temperature range is done based on the earlier discussed modelling by Javidi Shirvan. Tungsten and Copper have approximately the same work function and would thus have the same thermionic emissions as a function of cathode temperature. Recall that the boiling temperature of copper is significantly lower and thus copper cathodes primarily emit electrons through cathode spots[52]. For the current analysis, the thermionic emissions are assumed to be homogeneous throughout the plasma sheet cross section.

The model has a non-linear dependence to cathode temperature when it exceeds 3000K. This is because the thermionic emissions begin to dominate over secondary emissions and thermionic emissions have an exponential relationship with cathode temperature. In the current model cathode temperature is a user defined input. A parameter space search over the expected temperature range is performed.

| Externally Set Parameters | | test set D 1 | test set D 2 | test set Ar 1 | test set AR 2 | unit |
|---|---|---|---|---|---|---|
| t | time | 10 | 11.5 | 14 | 16.5 | $\mu s$ |
| $T_e$ | Bulk electron temperature | 2.4 | 2.4 | 2.4 | 2.4 | eV |
| $n_e$ | electron density | 2 | 2 | 2.5 | 1.5 | $10^{22}m^{-3}$ |
| $\overline{B}_y$ | Magnetic field (bulk) | 0.3 | 0.3 | 0.35 | 0.35 | T |
| $\phi_A$ | Anode voltage | 500 | 550 | 250 | 500 | V |
| $\phi_C$ | Cathode voltage | 0 | 0 | 0 | 0 | V |
| $T_{w,A}$ | Anode Wall Temperature | 600 | 600 | 600 | 600 | V |
| $T_{w,C}$ | Cathode Wall Temperature | 3000-4000 | 3000-4000 | 3500-4000 | 3500-4000 | K |
| $\delta$ | Plasma sheet thickness | 20 | 20 | 14 | 14 | [mm] |
| $u_{ze}$ | Axial velocity | 63 | 63 | 51 | 51 | [km/s] |
| $a_{iz}$ | Ionization degree | 1 | 1 | 1 | 1 | |
| $Z$ | Effective ion charge | 1 | 1 | 1 | 1 | |

Table 13: Externally determined input variables for test cases of the CSCX experiments[16].

All plasmas are assumed to be fully ionized ($a_{iz} = 1$) and the effective ionization rate $Z$ is assumed to be one for the following analyses. Spectroscopic measurements by Markusic et al. showed that singly ionized species were dominant in the plasma while the amount of higher level ionization was negligible. [16, p. 87].

| Externally Set Parameters | | test set D 1 & 2 | test set Ar 1 & 2 | unit |
|---|---|---|---|---|
| $I_{peak}$ | Peak current | 63 | 67 | KA |
| $I_{average}$ | Average current | 56.5 | 62 | KA |
| J | Current density | 28.3-31.5 | 44.2-47.9 | MA/m$^2$ |

Table 14: Expected output for the CSCX test cases[16]. Current density is estimated by the author.

### 5.4.1 Solutions procedure.

The model is highly non-linear and very sensitive to the initial guess. For simulations that did not include the effect of thermionic emissions, the initial guess method described in section 3.4.7 was sufficient to produce results. However when introducing thermionic emissions and setting the cathode temperature to the expected temperature range ($\geq 3000$) for arc discharges, the solver was unable to resolve. This is likely due to the complex non linear relationship between the thermionic emissions, the electric field and the cathode potential drop. To illustrate this relationship, let's take the model equations and neglect the effect of emissions on $E_W$ as well as the secondary and field electron emissions. Take the particle conservation equation 77:

$$n_{e0}\sqrt{\hat{T}_e/m_i} = \frac{-g^\star_{e,A} + g_{e,A} - g^\star_{e,C} + g_{e,C}}{2} \tag{110}$$

It is a linear combination of TEE and the Boltzmann equation. The Boltzmann equation has an exponential dependency on the potential drop $\varphi$:

$$g_{e,A} = n_{e0}\sqrt{\frac{\hat{T}_e}{2\pi m_e}}\exp(\varphi) \tag{111}$$

While the TEE equation which has an exponential dependency on the square root of $E_W$ which in turn depends on a square root of a linear combination of exponentials of $\varphi$.

$$g^{\star}_{e,C} = \frac{A_G}{e} T^2_{w,C} \exp\left( - \frac{W - \sqrt{e^3 E_{w,C}/(4\pi\varepsilon_0)}}{K_b T_{w,C}} \right) \tag{112}$$

$$\begin{aligned} \frac{1}{2}\Big(\frac{d\varphi_{w,C}}{dx}\Big)^2\Big|_{w,C} &= \exp(\varphi_{w,C}) - 1 + M^2_{i0}\Big[\Big(1 - 2\frac{\varphi_{w,C}}{M^2_{i0}}\Big)^{1/2} - 1\Big)\Big] \\ E_{w,C} &= \sqrt{\frac{2n_{e0}\hat{T}_e}{\varepsilon_0}\frac{d\varphi_{w,C}}{dx}\Big|_w} \end{aligned} \tag{113}$$

In essence the momentum balance equation is a linear combination of exponential and square roots of exponentials of $\varphi$. Javidi et al. also reported difficulties in ensuring the solver converged for a similar set of equations [14]. In their work the anode-plasma coupling was neglected. On the other hand they incorporated an energy balance which coupled wall temperature, electron temperature and sheath potential drop. This constrained the solution space but also increased the numerical complexity. Javidi resolved this by applying an "outer loop" for certain equations and variables using the secant method.

For the current work it was opted to do something similar. An initial calculation was done where the Schottky decrease $\Delta W = \sqrt{e^3 E_{w,C}/(4\pi\varepsilon_0)}$ was neglected. The output of this iteration was used as an initial guess for the next calculation. The Schottky decrease was set to a static value during this inner loop. After each inner loop, the output was used to determine a new set of initial guesses and fixed Schottky decrease values for the next loop. This would continue until the electric field output did not change between loops. Then calculations are done with an unconstrained Schottky decrease.[18] This method is imperfect as the range of selected wall temperatures, whereby the solver converges, are limited. Hence a search was done for stable solutions by iterating over a range of cathode wall temperatures and investigating where the residuals of the equation were minimal.

### 5.4.2 Results

| Variable | | test set D 1 | test set D2 | Unit |
|---|---|---|---|---|
| $V_C$ | Cathode sheath potential drop | -334.12 | -382.83 | V |
| $V_A$ | Anode sheath potential drop | -5.74 | -5.73 | V |
| $g^{\star}_{e,C}$ | Cathode emissions | $1.47{\cdot}10^{25}$ | $1.59{\cdot}10^{25}$ | $m^{-3}s^{-1}$ |
| $g^{\star}_{e,A}$ | Anode emissions | $7.89{\cdot}10^{24}$ | $7.89{\cdot}10^{24}$ | $m^{-3}s^{-1}$ |
| $E_{w,C}$ | Cathode E-field | $1.13{\cdot}10^{8}$ | $1.16{\cdot}10^{8}$ | V/m |
| $E_{w,A}$ | Anode E-field | $2.08{\cdot}10^{7}$ | $2.07{\cdot}10^{7}$ | V/m |
| $u_{xe}$ | electron bulk velocity | -6.09 | -6.14 | km/s |
| $\overline{B}_y$ | Magnetic Field | -245 | -247 | mT |
| $J$ | Current density | $1.95{\cdot}10^{7}$ | $1.97\ {\cdot}10^{7}$ | $A/m^2$ |
| $I_{tot}$ | Total Current | $3.91{\cdot}10^{4}$ | 39.3 | KA |
| $T_{w,C}$ | Wall temperature | 3023.5 | 3040 | K |

Table 15: Test set D 1: Deuterium propellant, pressure is 75 mTorr and voltage drop is 500 V, test D 2: Voltage drop is 550 V

**Test set D 1 and D 2:** For test set D 1, solutions can be found within the range of $T_{w,C}$ = 3015 K to 3060 K. Table 15 displays the results for $T = 3023.5K$, where the residuals of the equation are at a local minimum. The produced current values are lower than expected. The calculated total current is around 39 KA, while experiments had measured 56 KA as an average. For test case 2, the plasma voltage is slightly higher but total current is not significantly. One observes that $T_{w,c}$ is marginally higher at 3040 K. The range of temperatures within which solutions are found are slightly higher at a maximum of 3073 K. One observes that the magnetic field strength is lower than the expected value of 0.3 T. This is likely the result of lower current levels.

[18] This method was suggested by the supervisors. It is essentially Netwon-Raphson's method applied to the the outer loop.

| Variable | | test set Ar | Unit |
|---|---|---|---|
| $V_C$ | Cathode sheath potential drop | -204.44 | V |
| $V_A$ | Anode sheath potential drop | -9.13 | V |
| $g^{\star}_{e,C}$ | Cathode emissions | $9.01{\cdot}10^{24}$ | $m^{-3}s^{-1}$ |
| $g^{\star}_{e,A}$ | Anode emissions | $3.24{\cdot}10^{24}$ | $m^{-3}s^{-1}$ |
| $E_{w,C}$ | Cathode E-field | $1.10{\cdot}10^{8}$ | V/m |
| $E_{w,A}$ | Anode E-field | $3.22{\cdot}10^{7}$ | V/m |
| $u_{xe}$ | electron bulk velocity | -1.56 | km/s |
| $\overline{B}_y$ | Magnetic Field | -55 | mT |
| $J$ | Current density | $6.25{\cdot}10^{6}$ | $A/m^2$ |
| $I_{tot}$ | Total Current | 8.75 | KA |
| $T_{w,C}$ | Wall temperature | 3000 | K |

Table 16: Taste set Ar 1: Argon propellant, pressure is 75 mTorr and voltage drop is 250 V. No results for test set AR 2

**Test set Ar 1 and Ar 2:** Calculated current is significantly lower than with deuterium case. Magnetic field values are severely underestimated. Current as well as magnetic field are an order 6-7 lower than expected. For test case 4 the solver was unable to resolve. Apparently increasing the ion mass has a significant impact on the solver's ability to resolve. There are several plausible reasons for the underestimation of current in test set Ar 2, which are probably related to the issue with test case 4. The current is determined by the equations of states 3, 4 and 7. EoS 3 and 4 can be rewritten in terms of J and added.

$$0 = \frac{g^{\star}_{e,A} - g_{bolz}(V_A) - g^{\star}_{e,C} + g_{bolz}(V_C)}{2n_{e0}} - u_{xe} \tag{114}$$

$$0 = \frac{-g^{\star}_{e,A} + g_{bolz}(V_A) - g^{\star}_{e,C} + g_{bolz}(V_C)}{2n_{e0}} - \sqrt{\hat{T}_e/m_i} \tag{115}$$

$$0 = \frac{g^{\star}_{e,A} - g_{bolz}(V_A) - g^{\star}_{e,C} + g_{bolz}(V_C)}{2n_{e0}} - u_{xe} + \frac{-g^{\star}_{e,A} + g_{bolz}(V_A) - g^{\star}_{e,C} + g_{bolz}(V_C)}{2n_{e0}} - \sqrt{\hat{T}_e/m_i} \tag{116}$$

$$u_{xe}n_{e0} = -g^{\star}_{e,C} + g_{bolz}(V_C) - n_{e0}\sqrt{\hat{T}_e/m_i} = -\frac{J}{e} \tag{117}$$

The electron flux from the bulk to the cathode is negligible:

$$\frac{J}{e} = g^{\star}_{e,C} + n_{e0}\sqrt{\hat{T}_e/m_i} \tag{118}$$

In the model employed in this work, the current is thus dominated by ion sheath flux term ($n_{e0}\sqrt{\hat{T}_e/m_i}$). A larger ion mass, decreases Bohm velocity which significantly influences this flux. From a physics point of view other factors may also influence this. Thermal arcs may have an inversed sheath at the anode that accelerate approaching electrons while repelling incoming ions[52]. Another physical phenomenon not currently accounted for is canting, whereby the anode attachment travels more rapidly along the anode then along the cathode. Higher electron densities have been measured on the cathode side than on the anode. In the current model the electron density is assumed to be constant within the bulk region. This makes the spatial resolution very coarse. A more granular model would be needed that allows for varying electron densities in the cathode to anode direction.

### 5.4.3 Summary

The CSCX data was particularly useful as the voltage reported excludes the magnetic (induction) load. The magnetic field term was does neglected from the model and calculated a posteriori. In the case of test set D1 and test set D2, the estimated magnetic field shows good correspondence to the experimental values. For test set Ar 1 it is significantly lower. A similar trend is observed with the current density, which is closer to the experimental case for Deuterium. It appears that the model is more accurate for low Z materials.

## 5.5 Test Case 3: ADD-Simplex

The ADD-Simplex experiment is a parallel PPT just as CSCX but there are some significant differences. ADD Simplex is a smaller device with a length of 7 cm and a width of 2 cm. It has electrodes that flare outwards at an angle of 20 degrees. The electrodes are triangular instead of the common rectangular shape. The shape and flaring has a positive effect on the specific impulse [83]. On the other hand the infinitely wide electrode approximation for calculating the inductance used in equation 23 is no longer valid [83].

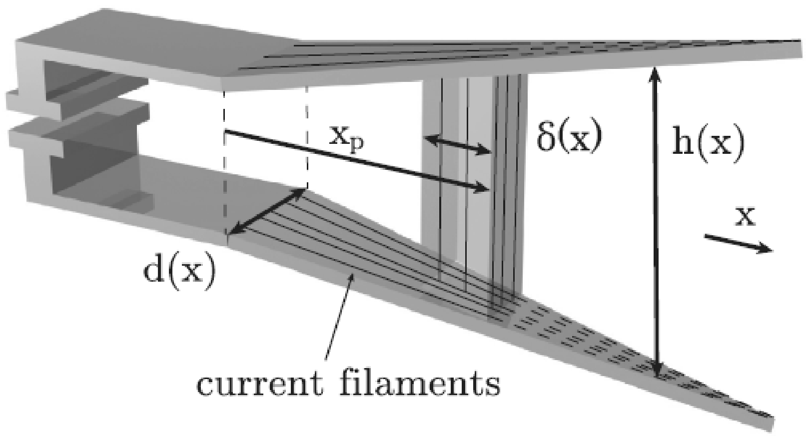


Figure 35: Visualisation of plasma sheet with thickness $\delta(x)$ moving downstream between the flared electrodes of ADD Simplex[17].

In contrast to the mono-atomic fluids of the ADD-Simplex experiments, the Teflon plasma is a multi-atomic mix. To simulate this with a mono-atomic plasma, a test particle is used whose properties are a weighted average (one part C, two parts F) of the elemental properties of Teflon $(C_2F_4)_n$.

| Design Parameters | | ADD Simplex | unit |
|---|---|---|---|
| $L$ | Length of electrodes | 0.07 | m |
| $m_i$ | Ion mass (C) | 12 | $m_p$ |
| $m_i$ | Ion mass (F) | 17 | $m_p$ |
| $m_i$ | Ion mass test particle | 15.33 | $m_p$ |
| $\mathcal{E}_i$ | Ionization energy (C) | 11.26 | eV |
| $\mathcal{E}_i$ | Ionization energy (F) | 17.4 | eV |
| $\mathcal{E}_i$ | Ionization energy test particle | 15.36 | eV |

Table 17: Design and material parameters for the ADD Simplex experiments. Ion mass is expressed in terms of proton mass $m_p$ or $1.672 \cdot 10^{-27}$ kg

Schönherr et al. had performed density and temperature measurements at three points on the downstream axis of the PPT [42]. Two data points where chosen from [42] to validate the presented model's ability to simulate Teflon propellant thrusters. These are listed in table 18. The first set of parameters are measurements taken at 10 mm from the propellant surface, the second at 40 mm. The distance between the electrodes is 25 mm at the first measurement point and has increased to 35 mm at the second point. The second measurement has been taken 2 $\mu s$ later than the first measurement. The electron density increases as more propellant has ablated while the temperature has decreased slightly as the propellant expands downstream.

Both measurements were taken at an initial discharge voltage of 1300 V and capacitance of 80 $\mu F$. The magnetic field attained values of 0.82 T during the discharge [4]. Optical Emissions Spectroscopy measurements as well as Mach-Zehnder Interferometry measurements indicated downstream velocities in the range of 40 to 45 km/s for carbon and fluorine ions. While the measurements have demonstrated that there are higher charge particles ($C^{++}$, $F^{++}$, $C^{+++}$...) present in the plasma, it is commonly assumed that single charge ions (($C^{+}$, $F^{+}$) dominate the plasma [42][30]. Numerical simulations of ion densities indicate that the density of higher charge particles is at least two orders lower than single charge ions [84]. Hence the effective ionisation charge is assumed to have a value of 1 in this work ($Z = 1$). Schönherr measured a plasma thickness of 34.5 mm using photographic observations [42].

| Externally Set Parameters | | test set 1 | test set 2 | unit |
|---|---|---|---|---|
| t | time | 1 | 3 | $\mu s$ |
| $l$ | axial distance | 10 | 40 | mm |
| $h$ | distance between electrodes | 25 | 35 | mm |
| $T_e$ | Bulk electron temperature | 2.5 | 2.25 | eV |
| $n_e$ | electron density | 3 | 8 | $10^{22} m^{-3}$ |
| $\overline{B}_y$ | Magnetic field (bulk) | 0-0.82 | 0-0.82 | T |
| | Discharge voltage | 1300 | 1300 | V |
| $\phi_A$ | Anode voltage | 1200 | 1000 | V |
| $\phi_C$ | Cathode voltage | 0 | 0 | V |
| $T_{w,A}$ | Anode Wall Temperature | 600 | 600 | V |
| $T_{w,C}$ | Cathode Wall Temperature | 3000-4000 | 3000-4000 | K |
| $\delta$ | Plasma sheet thickness | $\leq$ 34.5 | 34.5 | [mm] |
| $u_{ze}$ | Axial velocity | 40-45 | 40-45 | [km/s] |
| $a_{iz}$ | Ionization degree | 1 | 1 | |
| $Z$ | Effective ion charge | 1 | 1 | |

Table 18: Externally determined input variables for test cases of the ADD Simplex experiments.

### 5.5.1 Results

| Variable | | test set 4 | Unit |
|---|---|---|---|
| $V_C$ | Cathode sheath potential drop | -14.7 | V |
| $V_A$ | Anode sheath potential drop | -7.71 | V |
| $g^{\star}_{e,C}$ | Cathode emissions | $2.58 \cdot 10^{25}$ | $m^{-3}s^{-1}$ |
| $g^{\star}_{e,A}$ | Anode emissions | $1.53 \cdot 10^{25}$ | $m^{-3}s^{-1}$ |
| $E_{w,C}$ | Cathode E-field | $7.55 \cdot 10^{7}$ | V/m |
| $E_{w,A}$ | Anode E-field | $5.21 \cdot 10^{7}$ | V/m |
| $u_{xe}$ | electron bulk velocity | -2.01 | km/s |
| $\overline{B}_y$ | Magnetic Field | -0.56 | T |
| $J$ | Current density | $2.58 \cdot 10^{7}$ | $A/m^2$ |
| $I_{tot}$ | Total Current | 8.91 | KA |
| $T_{w,C}$ | Wall temperature | 3150 | K |

Table 19: Results

The solver did not resolve for the first test set. However the solver did resolve for the second set of values at x = 40 mm. The most significant difference between the sets of inputs is the larger distance between the electrodes. As the electrodes diverge, the electric field strength in the bulk plasma becomes smaller [19], given that the externally applied potential and the sheath potential drops do not appear to change significantly. A solution was found for a cathode temperature of 3150 K. The magnetic field was estimated to be 0.56 T which is within the order of magnitude of what would be expected. Total current was 8.9 KA. Based on [85] one would expect a current in the range of 20-25 KA at. Hence the current value is under predicted. There are a few possible explanation for this underestimation. For one the current 1-D model assumes the plasma slab to

[19] $E_p \approx \frac{\phi_A - V_A - (\phi_C - V_C)}{h}$, with $E_p$ representing the average electric field strength in the bulk plasma

have a homogeneous density. Measurements by Schönherr indicate that the electron density is higher at the cathode than at the anode[42]. Another assumption made in the model was that the width is significantly larger than the height, thus edge effects could be ignored. However the tapered design of ADD-Simplex actually enhances the edge effects. Hence the approximation equation, described in section 5.1, may fail to predict the magnetic field in this case. Leading to an overestimation of the inductive load. Finally it should be noted that the value of the plasma sheet thickness was measured by photographic measurements, which is essentially a subjective measurement. Furthermore the plasma thickness could vary as the plasma sheet travels downstream.

### 5.5.2 Summary

The literature data for ADD-Simplex gives values for the discharge voltage which includes the magnetic load in contrast to the CSCX data. Hence the magnetic field term was calculated a priori for this simulation. However it is noted that the infinitely wide electrode approximation used to calculate the magnetic field in this model has limited validity for the ADD-Simplex because the thruster has thin triangular electrodes. Teflon propellant is used which ablates to form a plasma consisting of carbon and fluorine atoms. A test particle was used to simulate this plasma. Its atomic mass was a weighted average of the atomic masses of carbon and fluorine.

Two data sets are chosen to be used as test cases. Test set 1 represents the conditions at the start of the discharge $1\mu s$ after the discharge. The data for test set 2 is collected at $3\mu s$ after the discharge when the plasma slab has moved halfway downstream (40 mm from the propellant block). The solver doesn't converge for the first set because the distance between the electrodes is smaller than 2 cm. It does converge for the second set as the electrodes diverge downstream. For the second set, the solver gives a reasonable estimate for the magnetic field however the current is underestimate by a factor of 2-3. This is due to the magnetic field approximation not being valid for ADD-Simplex' design.

## 5.6 Discussion

The validation process has demonstrated that in most aspects the model predicts similar trends as experimental results albeit with certain limitations. For one the model did not converge the case of GTAW simulations which have low total voltage ($\leq$ 15 V) or for small inter electrode distances ($\leq 2cm$) in PPTs or GTAW. The central question answered by the validation process is what cathode wall temperature is reasonable to assume for the simulation. The cathode wall temperature has significant influence on the output of the model as thermionic emissions are the dominant mechanism providing current in a thermal arc discharge. The field electron emissions on the other hand are negligible. The cathode temperature levels required for this mode of discharge exceed the vaporization temperature of copper, which is the most common material used. Hence the formation of cathode spots which are not included in this model.

The current model is able to predict current levels within an order of magnitude of the experimental values. Experimental current values were between 1.5 and 7 times higher. In the case of argon propellant, with atomic mass 40, the divergence was most severe. This is the result of the equation used for current balance. Here it is assumed that the total electron flux (summing over the two sheaths) is equal to the sum of the Bohm ion flux at the anode and cathode, to conserve charge. A classical sheath is assumed at the cathode and anode whereby plasma ions are accelerated electrostatically to the walls and thermal electrons are repulsed by the space charge. However it is likely that the ions are repelled at the anode while the electrons are accelerated, by an inversed sheath. Furthermore canting leads to differences in electron density at the anode and cathode[16]. The canting angle is strongly influenced by the atomic mass of the propellant[53]. Higher atomic mass tend to lead to higher canting angles (e.g. 10% for hydrogen and 60-70% for Argon). The phenomenological mechanisms behind canting is complex, not fully understood and beyond the scope of the thesis. It does however explain why the predictions for lower atomic masses where closer to experimental values. A lower canting angle deviates less from an the idealized monolithic plasma slab, that remains perpendicular to the electrodes, assumed in the current model.

Another aspect of the model that affects the current calculation is the magnetic field as this causes an inductive load. For a self induced magnetic field this is proportional to the current. For the future fully coupled model, this would be calculated by integrating the Lorentz force equation over the plasma cross section. To allow calculations using the isolated transversal model, a work-around was used. An estimated relation based on the self-inductance of perpendicular electrodes of infinite width was used as is common for PPT models[9]. However this assumption is not valid for the ADD-Simplex due to its particular geometry. Which could partially explain the difference in results.

# 6 Further Analysis and Results

Now that the validity and limitations of this model have been assessed, one can further investigate the model outputs with a larger degree of freedom. The validation process described in the previous section already describes some analyses of trends in the models output (e.g.: the effect of electrode distance and potential discussed in section 5.1). The validation process took a data point by data point approach. For the analyses presented in the current section, the input parameters were varied over an expected range to examine their influence on the output. The input parameters that are of particular interest are the electrode temperature, electron density, electrode distance, anode voltage and cathode temperature. Table 20 describes the ranges over which these parameters were varied. These are based on the typical PPT measurements described in table 2:

| Externally Set Parameters | | min | max | unit |
|---|---|---|---|---|
| $h$ | distance between electrodes | 10 | 50 | mm |
| $T_e$ | Bulk electron temperature | 1 | 3 | eV |
| $n_e$ | electron density | 0.1 | 10 | $10^{22} m^{-3}$ |
| $\phi_A$ | Anode voltage | 10 | 1000 | V |
| $T_{w,C}$ | Cathode Wall Temperature | 1000 | 4000 | K |

Table 20: Input variable ranges

For the other parameters, the following default values where chosen:

| Design Parameters | | value | unit |
|---|---|---|---|
| $m_i$ | Ion mass (H) | 1 | $m_p$ |
| $\mathcal{E}_F$ | Fermi (Cu) | 7 | eV |
| $W$ | Work function (Cu) | 4.4 | eV |
| $\mathcal{E}_i$ | Ionization energy (H) | 13.6 | eV |
| $A_G$ | Material Schottky constant | 80 | $10^4 \mathrm{Am}^{-2}\mathrm{K}^{-2}$ |
| Externally Set Parameters | | | |
| Z | Effective ionization number | 1 | |
| $a_{iz}$ | ionization degree | 1 | |
| $\phi_C$ | Cathode voltage | 0 | V |
| $T_{w,A}$ | Anode Wall Temperature | 600 | K |
| $\delta$ | Plasma sheet thickness | 20 | mm |
| $u_{ze}$ | Axial velocity | 63 | [km/s] |

Table 21: Input parameters that were held constant during this analyses.

For the analyses hydrogen was chosen as the propellant. During the validation phase it became evident that the model results showed better correspondence to experimental results for lower mass propellants. The CSCX test case with a deuterium propellant had the best predictive match. Hence hydrogen is best suited for the following analyses.

Given that the model does not always resolve when TEE was included, an initial analyses is done neglecting TEE (section 6.1). This demonstrated the influence of electron temperature and density on the electron current. Later analyses included the thermionic emissions but consisted of less data points because the solver did not always converge for all input parameters. This is due to the highly non-linear nature of the equation as has been discussed earlier. Nevertheless interesting observations can still be made. These are discussed in section 6.2. More analyses has been on the effect of the the distance between electrodes $h$ on current density while including the influence of TEE, which is discussed in section 6.3. FEE is neglected in all cases as it had been shown to be negligible compared to SEE (and by extent ion TEE) for electron densities lower than $10^{23}$ m$^{-3}$.

## 6.1 Initial Analyses (excluding thermionic emissions)

The analyses presented here discusses the effect of electron density and temperature on the current and magnetic field. First the results are presented without including the effect of the magnetic field. An upper and lower saturation regime were identified as can be seen in figure 36. One observes an apparent maximum electron density of $7.5 \cdot 10^{22}\mathrm{m}^{-3}$ for these conditions. The magnetic field strength was set to zero for the initial calculations. In figure 36a one observes upper and lower limits to the electron bulk velocity. Higher densities lead to lower velocities due to inter-particle friction. In figure 36b this upper current saturation limit is more clearly visible.

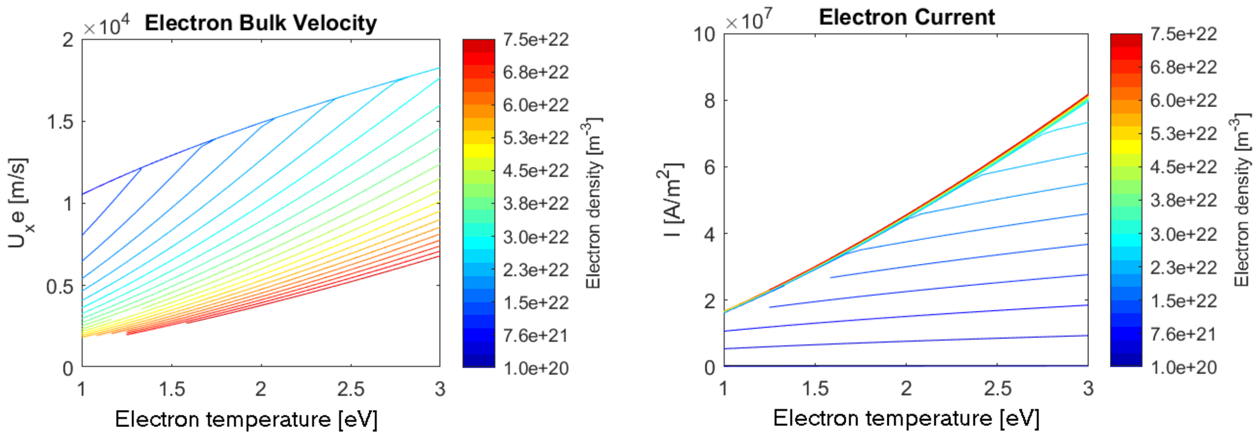


(a) Electron bulk velocity

(b) Transverse current density

Figure 36: Simulations for test set 1 without magnetic field. Potential is 1000 V.

The explanation for what appears as upper and lower saturation curves for the transverse electron velocity is quite simple. At lower densities/higher temperatures, the bulk resistance is low and thus the cathode sheath "eats" the whole potential difference. Furthermore at lower densities, the back diffusion flux is relatively significant. A high cathode potential drop prevents a large diffusion of thermal electrons back to the cathode. At higher densities, the resistance takes up most of the potential difference between the electrodes, this resistance can't be higher than the externally applied potential. The higher density also leads to higher current.

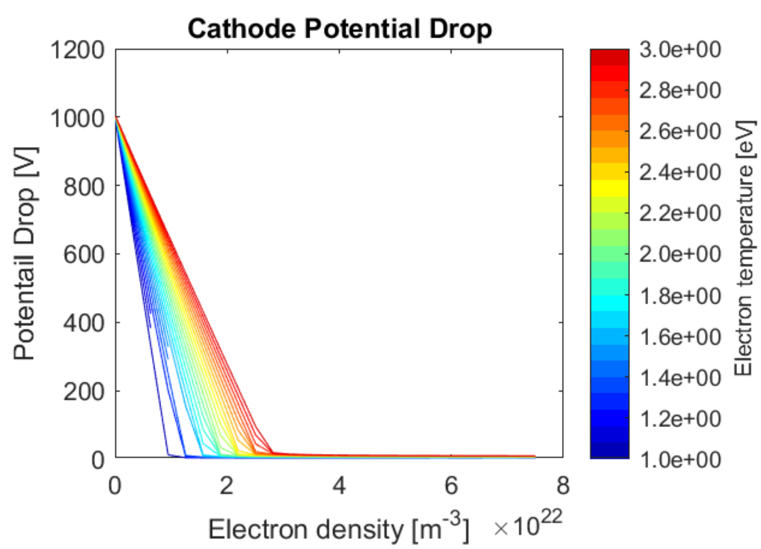


Figure 37: The potential drop in the cathode sheath at an applied voltage of 1000 V.

It can be seen in figure 37 that as the density increases, plasma resistivity increases and the cathode sheath potential drop is displaced by the bulk resistance After a certain density the resistance saturates as internal resistance cannot be larger than applied voltage. For lower temperatures this occurs at lower densities. This explains the saturation mechanism seen in figure 36b.

Adding a magnetic field term, using the estimation method proposed in section 5.1, changes the shape of the curves slightly. A plasma sheet thickness $\delta$ of 20 mm was assumed. The current is lower as the magnetic field operates as an extra friction force. The magnetic field achieves the expected magnitude of 0.7 T in figure 38b. Subsequent analyses in sections 6.2 and 6.3 also include the magnetic field term.

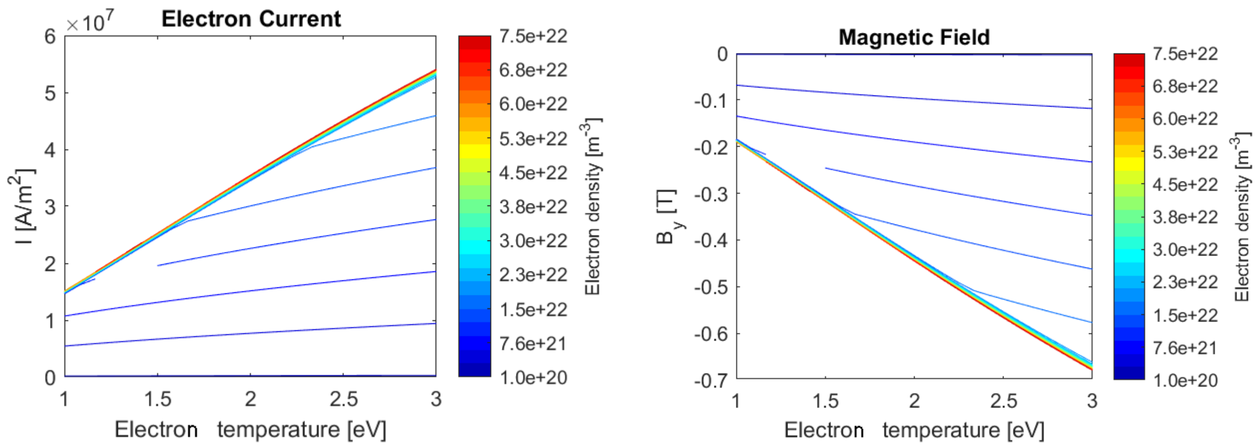


(a) Current density. Magnetic field estimated using equation 108

(b) Magnetic field.

Figure 38: Simulations with magnetic field

## 6.2 Cathode Temperature

Now that the effect of electron temperature and density on current density has been examined, it is time to investigate the influence of the cathode temperature. The following simulations compare the potential-current (I-V) characteristic for cathode temperatures in the range of 2500 to 3500 K. The electron density is set to $10^{22}$ m$^{-3}$, which is a representative density for a PPT plasma. Different values were attempted for electron temperature and inter-electrode distance. The input values that were the most stable during grid search, are presented here. Electron temperature is set to $T_e = 2.5$ eV, which is on the higher range of temperatures expected in a PPT. As seen in figure 36b, a higher electron temperature leads to higher current levels because of the inverse relationship between electron temperature and resistance [5]. The inter-electrode distance was set to 0.04 cm. The I-V characteristic of these simulations is presented in figure 39.

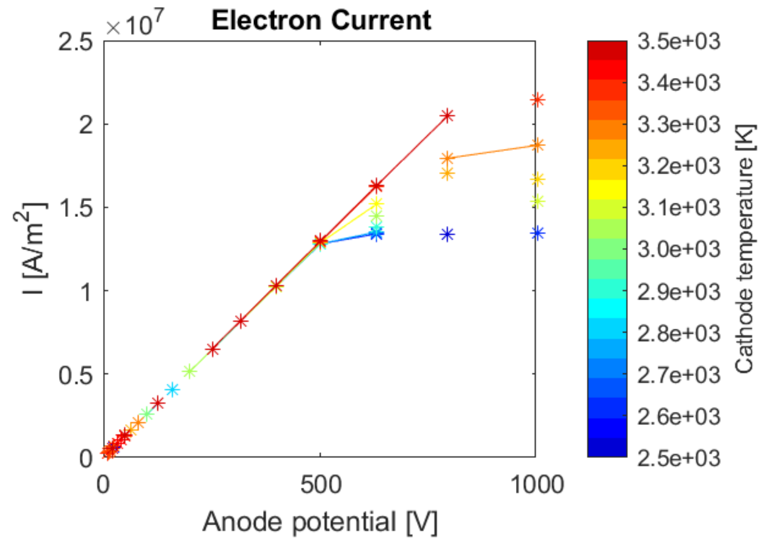


Figure 39: Current density - potential characteristics for different cathode temperatures in the range of 2500 to 3500 K. n= $10^{22}$ m$^{-3}$, $T_e$ = 2.5 eV, h = 0.04 cm

At sufficiently high cathode temperature, the current density demonstrates a linear relationship with anode potential, as can be observed in figure 39. In this plot, simulations for different values of cathode temperature are overlaid. At the lower temperatures around 2500 K, thermionic emissions are negligible (can be seen in figure 42b) . The current density value plateaus around 500 V. For higher cathode temperature values the current density values continue to increase weakly after 500 V. At 3500 K the I-V characteristic approaches a more linear relationship over the entire potential range (0-1000 V). To understand the cause of the "plateau-effect" the sheath potential drop at the anode and cathode; and the proportions of thermionic and back diffusion flux, are examined. At lower cathode temperature temperatures, a higher electric field at the cathode surface is needed to provide for a certain amount of thermionic flux than at higher temperatures (fig. 40a). Hence a higher cathode potential drop is needed to repel plasma electrons diffusing towards the cathode and promote balance out the emissions and promote thermionic emissions (fig. 40b).

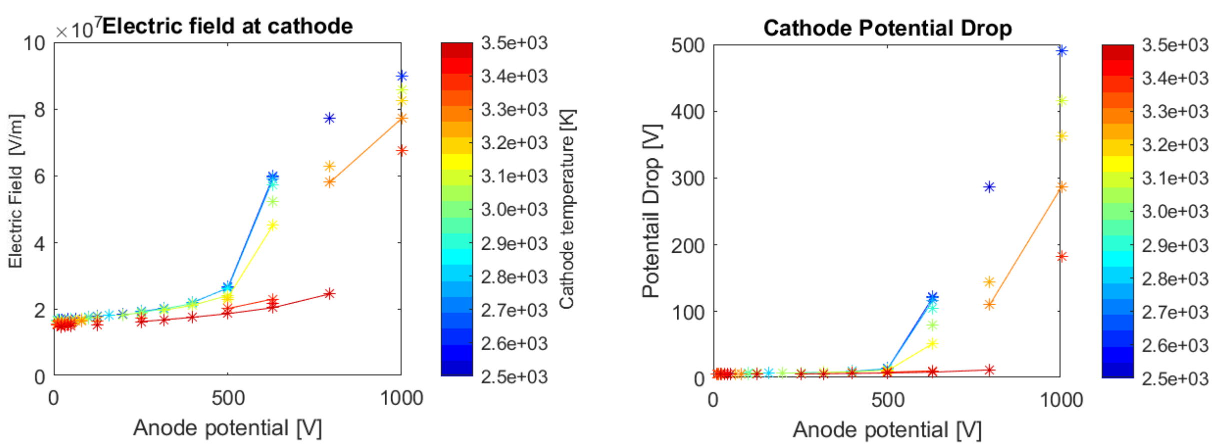


(a) (b)

Figure 40: Cathode conditions for cathode temperatures in the range of 2500 to 3500 K. n= $10^{22}$ m$^{-3}$, $T_e$ = 2.5 eV, h = 0.04 cm

The cathode sheath potential drop starts at a value in the range of 6.2 to 7 V for an externally applied voltage of 10 V (The higher value corresponds to 2500 K while the lower value corresponds to 3500 K).

It steadily increases towards the range of 8.2 to 14.1 V for 500 V. After this, the sheath potential drop strongly diverges for different temperatures. For higher temperatures the cathode sheath potential drop stays in the order of 10 V while for lower temperatures it increases towards 200-300 V. The anode sheath potential drop is also influenced by the cathode temperature for $\Phi_A$ higher than 500 V (fig. 41). Initially $V_A$ decreases from 6.9 ($\Phi_A = 10V$) to 5 V ($\Phi_A = 500V$). After this, the results are different depending on cathode temperature. For higher temperatures, the sheath potential continues to decrease towards 4.5 V while for lower temperatures the sheath potential drop "plateaus" around 5V. A sample of sheath potential drop values is summarized in table 22.

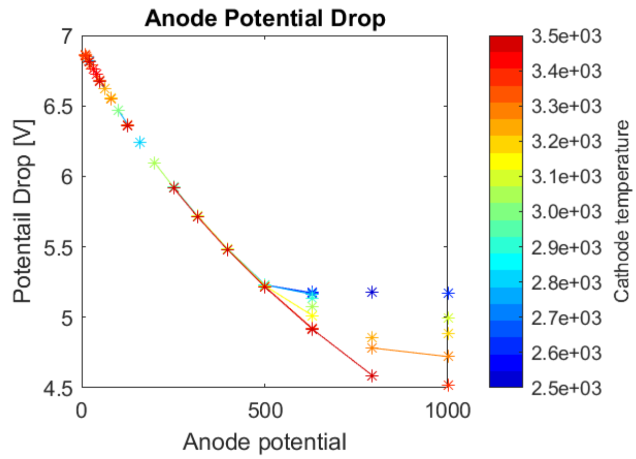


Figure 41: Anode sheath Potential drop for an anode temperature of 600 K and cathode temperatures in the range of 2500 to 3500 K. n= $10^{22}$ m$^{-3}$, $T_e = 2.5$ eV, h = 0.04 cm.

| | $T_{w_C} = 2500$ | | $T_{w_C} = 3300$ | | $T_{w_C} = 3500$ | |
|---|---|---|---|---|---|---|
| | $V_C$ [V] | $V_A$ [V] | $V_C$ [V] | $V_A$ [V] | $V_C$ [V] | $V_A$ [V] |
| $\Phi_A = 10$ | 7 | 6.9 | 6.4 | 6.9 | 6.2 | 6.9 |
| $\Phi_A = 500$ | 14.1 | 5.2 | 10 | 5.2 | 8.2 | 5.2 |
| $\Phi_A = 800$ | 286 | 5.2 | 110.6 | 4.8 | 12.1 | 4.5 |
| $\Phi_A = 1000$ | 490 | 5.2 | 286.6 | 4.7 | - | 4.5 |

Table 22: Sample of potential drop values at three different temperatures and four external potential levels.

The back diffusion of thermal electrons through the sheath towards electrodes ($g_A$, $g_C$) is a function of sheath potential drop (eq. 10). A larger sheath potential drop causes repels electrons causing lower flux levels. In figure 42a, the back diffusion flux at the anode and cathode side are shown. For the low temperature case, $g_C$ is $1.4 \cdot 10^7$ A/m$^2$ and decreases linearly with the increasing applied voltage. For higher temperatures $g_C$ starts at a higher value ($2 \cdot 10^7$ A/m$^2$). On the other hand $g_A$ starts at $1.4 \cdot 10^7$ A/m$^2$, regardless of cathode temperature and then increase linearly. At 500 V the curves diverge for different temperatures. The anode sheath flux plateaus for lower temperature values but increases for higher temperatures. The thermionic emissions fluxes, shown in figure 42b, increases with cathode temperatures but shows relatively weak increases with higher anode potentials. SEE (flat red line) is not influenced by potential or cathode temperature. At a temperature of around 3100 K, TEE and SEE are comparable. For higher temperatures, TEE dominates over SEE.

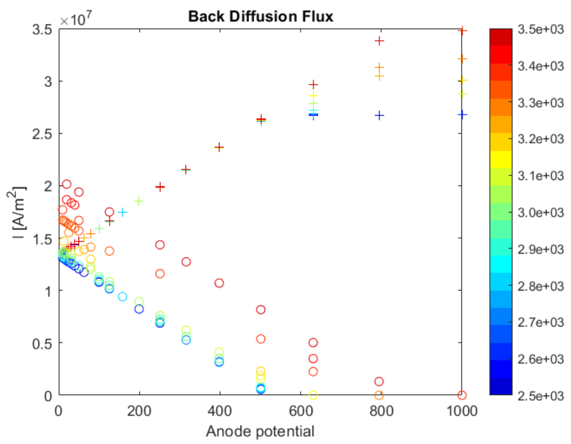


(a) Back diffusion flux at the cathode (∘) and anode (+).

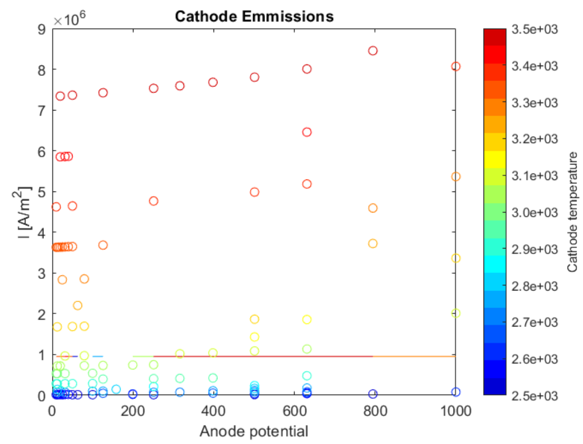


(b) Thermionic emissions (∘), the sheath electron emissions are represented by the solid line.

Figure 42

It should also be noted that the increase for TEE with higher cathode temperatures is approximately the same as the increase of $g_C$. Furthermore the decrease of $g_C$ with applied potential is approximately the same as the increase of $g_A$. This is because of the charge conservation (equation 77):

$$n_{e0}\sqrt{\hat{T}_e/m_i} = \frac{g_C + g_A - g_C^\star - g_A^\star}{2} \tag{119}$$

Where the emissions fluxes ($g_C^\star$, $g_A^\star$) are the sum of TEE and SEE at the electrode.[20] SEE is the same at both anode and cathode. TEE at the anode side is negligible. Hence charge conservation can be rewritten as:

$$n_{e0}\sqrt{\hat{T}_e/m_i} = \frac{g_C + g_A - TEE_C}{2} - SEE_{C/A} \tag{120}$$

The sum of the electron fluxes equals the ion sheath flux ($n_{e0}\sqrt{\hat{T}_e/m_i}$). Rewriting this shows that higher thermionic emissions raise the sum of back diffusion emissions:

$$n_{e0}\sqrt{\hat{T}_e/m_i} + SEE_{A/C} + TEE_C/2 = (g_C + g_A)/2 \tag{121}$$

SEE is constant throughout the simulation and therefore bears no influence on these dynamics. The evolution of the back diffusion on the anode and cathode counter balance each other for rising current levels. In other words, when J goes up, $g_C$ goes down and $g_A$ goes up. Take the total current density equation (eq: 74:)

$$en_eu_{xe} = e\frac{g_A^\star - g_A - g_C^\star + g_C}{2} \tag{122}$$

Using the logic as for the continuity equation, the current density equation simplifies to:

$$J = e\frac{g_A + TEE_C - g_C}{2} \tag{123}$$

SEE from the anode and cathode balance each other out in this equation. It is seen here that $g_A$ has a positive contribution to current while $g_C$ has a negative contribution. $TEE_C$ allows the difference $g_A - g_C$ to be smaller, as can be seen in figure 43. The contribution of $TEE_C$ is almost exclusively taken up by a higher $g_C$ because this allows for a smaller $V_C$. This is also reflected in table 22 as higher TEE is linked with higher cathode temperatures. A smaller cathode sheath potential drop "eats" less of the total potential and allows for more current. In figure 43 it is evident that the the net contribution of back diffusion flux to

[20] FEE was shown to be negligible in sections 5.2 and 5.3

current ($g_{e,A} - g_{e,C}$) is far larger than thermionic emissions. The thermionic emissions play a balancing role and mitigate the "plateau" effect described earlier.

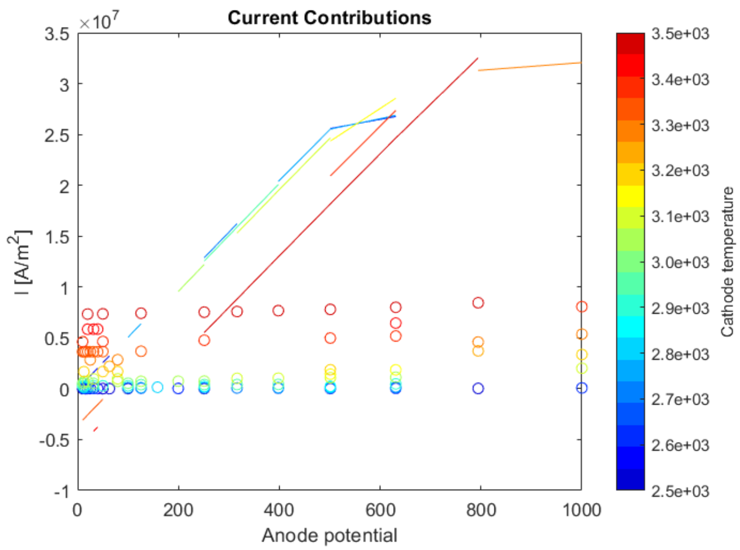


Figure 43: The net back diffusion flux (anode back-diffusion - cathode back diffusion) is represented by the solid lines. The cathode emissions are represented by (◦)

.

## 6.3 Influence of Inter-electrode Distance

In section 5.1, it had been discussed that smaller inter-electrode distances increase the current to potential ratio. This same trend can be seen in figure 44. The current increases more rapidly when the distance is smaller. This is because in the current model, electron density and temperature have been assumed to be constant in the plasma slab. As such the plasma sensitivity should also be constant throughout. A smaller distance between the electrodes means less plasma volume for the current to traverse. Hence the constant electric field throughout the plasma bulk is a function of the external voltage, electrode distance and electron temperature and distance.

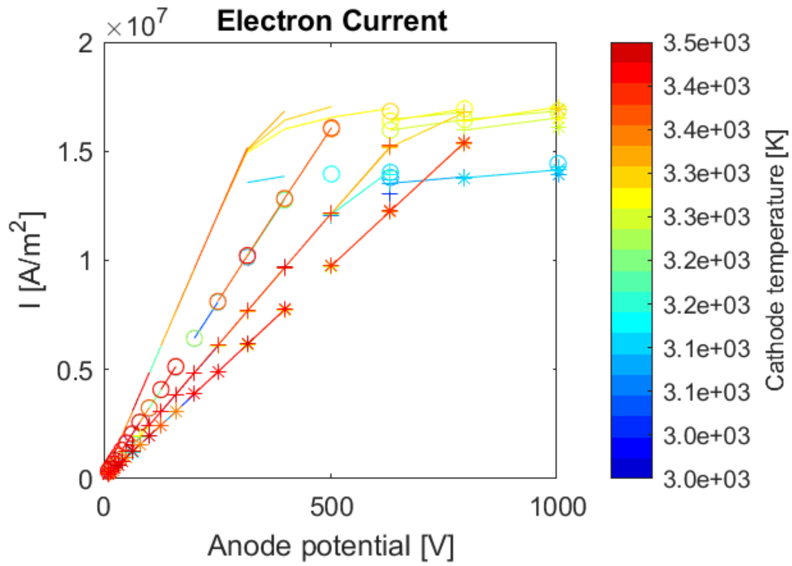


Figure 44: Current potential characteristics for cathode temperatures in the range of 3000 to 3500 K, n= $10^{22}$ m$^{-3}$, $T_e = 2$ eV and different inter electrode distances. $\circ$ : $h = 0.02$ cm, $+$ : $h = 0.03$ cm, $*$ : $h = 0.04$ cm, -: $h = 0.05$ cm

## 6.4 Discussion

The analyses in this section expanded upon the conclusions drawn during the model validation. The electron temperature dictates the plasma electrical resistivity ($\eta$)[73][5]. This is reflected by the electron bulk velocity curves in 36a.

$$\eta \propto T_e^{-3/2} \tag{124}$$

The electric field in the plasma is the applied potential divided by the inter-electrode distance in the current model (eq. 79). This in turn is related to current density and resistivity [73]:

$$\frac{\phi_A - V_A - (\phi_B - V_B)}{h} = E = \eta J \tag{125}$$

In figure 36b, lower current levels are attested for low electron densities. As explained in section 6.1, this is the result of higher cathode potential drops at lower densities needed to prevent thermal electron diffusion.

When including the thermionic emissions in the model this effect is alleviated because the thermionic flux emitted by the cathode presents a counter balance to the thermal electron flux diffusing back from the bulk plasma, as discussed in section 6.2. This requires the cathode temperature to be higher than a certain value (approximately 3000 K). The solver converges for a wide range of temperatures (3000-3500 K) but no correlation is found between temperature and current. The only effect observed within the current model setup is that the cathode temperatures causes an upper limit on current density. The lower the cathode temperature is, the lower the upper limit of current density as observed in figures 39 and 44. It should be noted that the current analyses is limited due to the lack of energy balance equations. Such equations that account for energy transfer between the electrode, sheath and plasma; would couple the cathode temperature, sheath potential drop and bulk plasma temperature [14].

The results in section 6.3 showed steeper current increases for shorter inter electrode distances. This is because the assumption of homogeneous density in the model. For a larger inter-electrode distance, the current has to traverse more plasma volume, leading to higher resistance. Future versions of this model that allow for variations in local temperature and density along the transverse axis, could have different results.

# 7 Applications in Fusion Research

As discussed in sections 1.1 and 1.5, there is potential for synergy between research for plasma thrusters and fusion reactors even if the physical conditions may vary strongly. The research presented in this thesis has been focused on plasma-wall interactions in the PPT and its implications for simulations. The PROMETEO project has a relevant sub-objective[40]:

> Plasma-wall interaction, materials, propellants. A fraction of the plasma, both in Electric Space Propulsion (ESP) and Magnetic Confinement Fusion (MCF), eventually escapes magnetic confinement and reaches the walls, generating sputtering and releasing impurities and cold particles, which again significantly reduces the efficiencies of the ESP and MCF devices. Combining theory and experiment, we search for magnetic topologies, materials, and propellant mixtures that minimize wall effects. Given the low density of the plasma and the secondary electron emission at the walls, a kinetic analysis becomes necessary to assess the electron distribution function and the fluxes to the walls correctly.

Next to synergies in plasma-wall interaction research, PROMETEO also has interesting objective when it comes to the versatility of simulation codes[40]:

> Multi-thruster simulation platform. The solution of the above problems will enable the inclusion of those phenomena in an integral plasma thruster simulator capable of dealing with different thruster types. This is a key milestone, firstly, to understand the combined effects of those phenomena, and secondly, for technology transfer in ESP.

A simulation platform that could be applicable to a collection electric thruster types, with various magnetic geometries and propulsion mechanisms, can also be amended for simulation of dynamics in a tokamak. The following section will compare the physics and magnetic geometry of PPTs and magnetic confinement reactors, with a particular focus on the divertor.

## 7.1 Magnetic confinement reactors PPT comparison

As discussed in section 1.5, the conditions in a MCF reactor can vary greatly. The core of a reactor has a temperature of 15 keV and density of $10^{20}m^{-3}$[8] while the divertor region has a temperature in the 1-5 eV range and a density of $10^{21}m^{-3}$[39]. The electron densities expected in an APPT are in the range of $10^{22}m^{-3}$[42] and the electron temperature is in the 1 - 3 eV. Hence the divertor region provides more opportunities for synergistic research. The PPT plasma is categorized as non-magnetized because collision frequency is higher than the gyrofrequency [54]. The hall parameter, the ratio of the gyrofrequency to collision frequency, of a PPT is around 0.1[51]. This plays a role in the canting effect that was discussed in section 5.6. On the other hand, weak magnetization means that the PPT plasma does not tend to confine itself along magnetic field lines as a tokamak plasma.

Figure 45: Tungsten divertor plates in the Joint European Torus at the Culham Centre for Fusion Energy in Oxfordshire, Uk. Photographs from EFDA (European Fusion Development Agreement)[18]

The magnetic field in a MCF reactor runs in helical lines around the toroid. In the divertor region these magnetic field lines approach the surface at a very small near-parallel angle. Eventually the gyrating particles intersect the surface and enter the sheath. Ions gyrate with a larger radius then electrons and thus are more likely to strike wall than diffuse along the field lines[86]. Depending on the angle of incidence, the sheath potential may be affected by the ratio between particle collision rates and gyrofrequency[19]. This is called the "Chodura" regime. At intersection angles larger than 5 degrees (for ITER-like conditions) the sheath potential drop is on the same order as a non-magnetized sheath[87]. While the magnetic field is perfectly parallel to the electrode surface in a PPT, the low magnetization of the PPT plasma precludes the aforementioned Chodura effect.

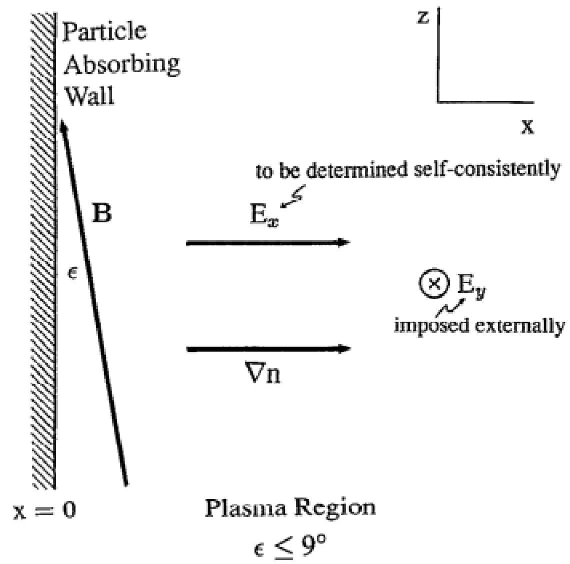


Figure 46: The geometry of a plasma sheath region with a magnetic field at low angle. Taken from Holland et al's simulations of magnetized sheath structures[19].

## 7.2 Magnum PSI

The plasma is generated by a "cascaded arc source". A cathode and anode are separated by 5 cascaded plates that are electrically insulated from on another. Gas flows in from an inlet behind the cathode, is ionized by the arc going from cathode to anode, before flowing out the anode nozzle. It is then expanded in a magnetic field that is parallel to the flow direction. The magnetic field in Magnum PSI can achieve magnetic fields of up to 2.5 T[39]. The plasma is considered strongly magnetized. As a result, the heat flux and particle fluxes of this plasma are anisotropic. I.e. these are lower in the radial direction of this plasma, than in the downstream axial direction (parallel to the magnetic field)[18].

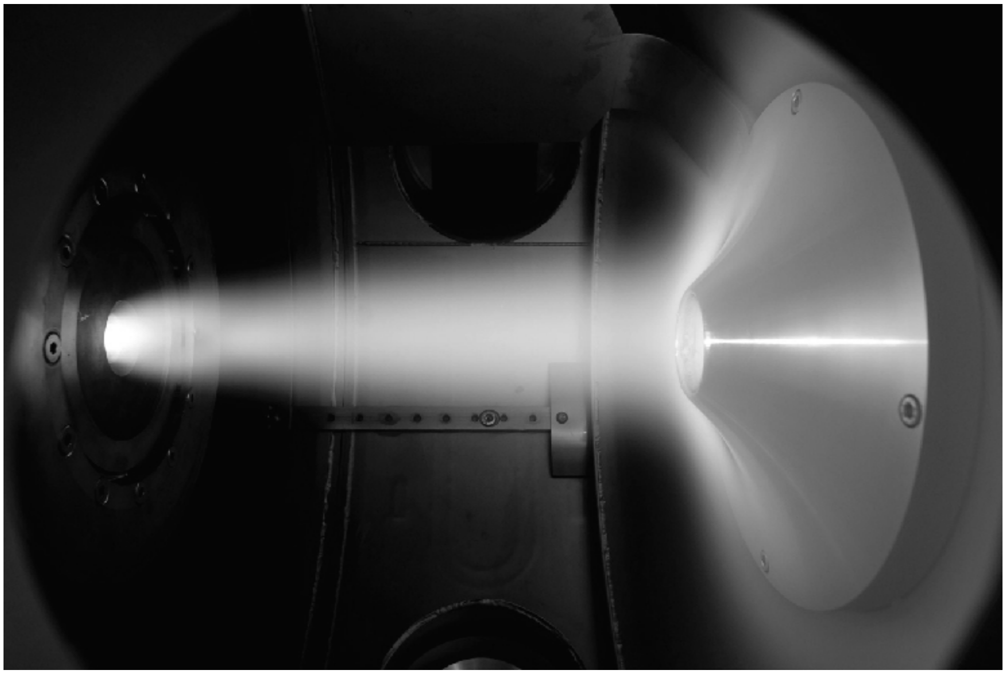

Figure 47: Argon Plasma jet in magnum PSI[18]. Left is the cascaded arc source, at the right is the target plate used to study the plasma wall interaction. Magnetic field lines run parallel to the plasma flow.

The magnetic fields that are attested in a PPT are some what lower (0.3 - 1 T) than Magnum PSI [4, 42, 53]. It is also perpendicular to plasma flow instead of parallel. While the PPT plasma flow is primarily driven by the Lorentz force, it is largely driven by thermal expansion in the Magnum PSI. A higher magnetic field in Magnum PSI decreases the radius of the plasma jet[18]. Shock waves, that are caused by the supersonic thermal expansion, are pushed to more upstream positions under the influence of stronger magnetic field. These shock waves are also weakened by the stronger magnetic field.

The plasma beam rotates due to Lorentz forces acting on the expanding beam[18]. A similar rotating dynamic is seen in an MPDT[88]. As discussed in section 1, MPDTs and PPTs are both categories of Lorentz-force thrusters, with the former being axisymmetric and intended to operate in steady state. For the PPT however, this rotational dynamic is not relevant. On the other hand the cascaded arc source has some similar conditions to a PPT as the current is generated by thermionic emissions for a large part. The code developped for the current project could be used to simulate flow in the arc source if the magnetic field term is dropped.

### 7.3 Strongly emitting surfaces in Divertors

There are efforts to model the effect of thermionic emissions in fusion reactor. Campanell has been researching the influence of strongly emitting divertor surfaces on the plasma [89][7][20], and had proposed an inverse sheath mode for arc discharges (figure 6). In the inverse mode, the electrodes have a higher potential than the bulk plasma[7]. This has potential to innovate operation of the divertor[20]. The divertor is a region that faces extreme conditions such as high particle (up to $10^{24} m^{-2} s^{-1}$) and heat flux ($\geq$10 MW/$m^2$) [39]. The heat loads on the divertor surface may damage the structural integrity of the plates[90][91]. To mitigate this it is often proposed to seed the divertor region with impurities. Neutrals particles, such as nitrogen, are injected near the divertor[90]. These emit strong radiation as they ionize[91]. The radiation spreads the heat power over a larger region, thereby decreasing the maximum heat flux received by the divertor surface. The impurities also collide with ions coming into the divertor region, there by decreasing density. The aim of this procedure is to create a significant pressure and heat power drop in the divertor plasma before it reaches the surface. Such a regime is called "detachment"[91]. The downside of using neutral injections to achieve detachment is that such impurities may compromise the core plasma[20]. Collisions between fuel particles (deuterium and helium) and heavier impurities, transfer momentum and thermal energy which would be a loss for the fusion reactor. Hence Campanell's inversed sheath mode presents an interesting alternative method to achieve divertor detachment[20].

For one a reversed sheath repels ions instead of accelerating them. The impact energy of ions are reduced which minimizes sputtering[20]. It also reduces the incoming ion flux, thereby mitigating another heating mechanism, recombination heat flux. When an ion strikes the surface it deposits its kinetic and recombination energy on the surface. Recombination is when an ion neutralizes by picking up an electron from the surface. It thereby looses the energy (13.6 eV) that it needed to ionize. Reducing the incoming ion fluxes also reduces the occurrence of recombination.

Electron emissions themselves also have an impact on the heat balance in the plasma. Figure 48 is a qualitative sketch comparing the classical, SCL and inverse sheath regime. For the classical and SCL sheath, the velocity distribution of electrons at the sheath edge is near Gaussian, which represents thermal diffusion of particles. The emitted thermionic electrons are electrostatically accelerated through the sheath and represented by the beam in the EVDF. For the inverse regime the distribution consists of two temperatures. On one hand there are hotter plasma electrons that are accelerated towards the wall and there by decrease in density. On the other hand there are colder thermionic electrons that are decelerated as they leave towards the plasma and thereby increase in density. The interaction between these to populations decreases the electron temperature at the sheath edge. The sheath layer is very thin, but this effects would set a low temperature boundary to the divertor plasma. Hence making a certain length of the plasma colder[20].

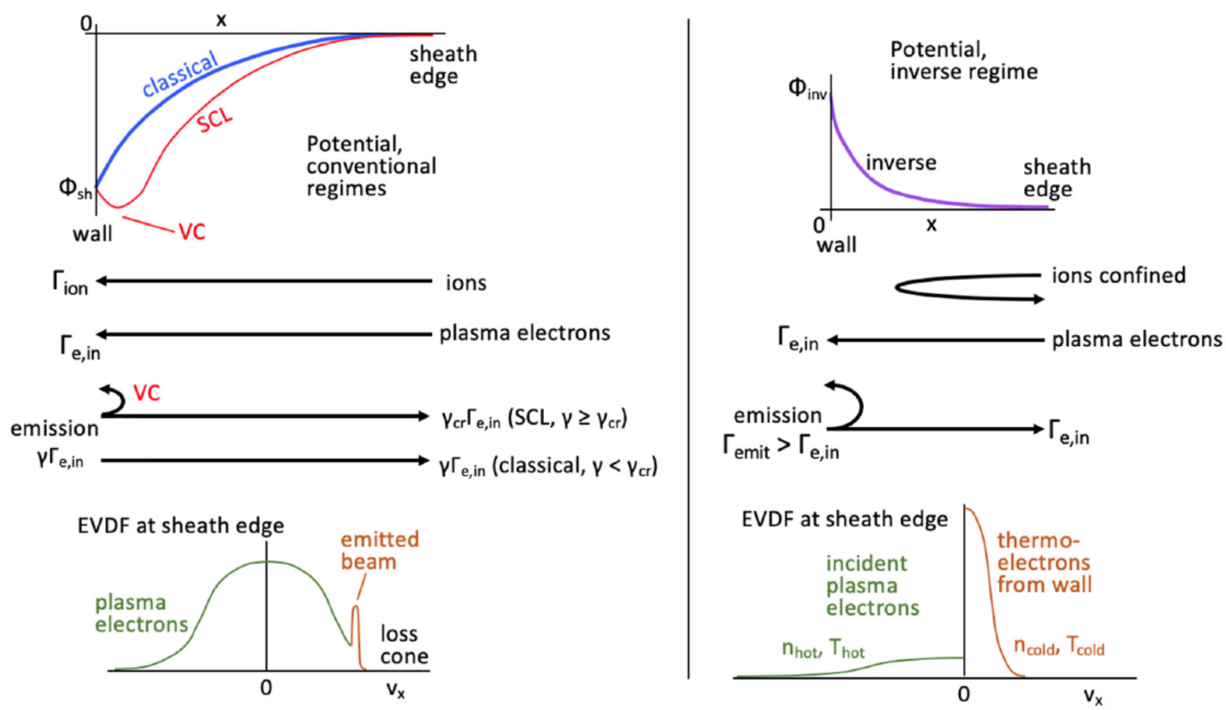


Figure 48: Diagram representing the sheath potential distributions, particle flux balance and edge Electron Velocity Distribution (EVDF) for the three sheath regimes[20]. $\Gamma$ represents flux and $\gamma$ represents the ration between emitted electrons and in incident electrons. When $\gamma \geq \gamma_{cr}$ the sheath transitions to SCL.

Strongly emitting divertor surfaces hence promises to be a very interesting application of the code developed in this project. Two adaptations would be needed. For one the code currently only simulates classical sheaths. It needs to be adapted to allow for inverse sheath mode and regime transition. Vallis Shaw had mentioned that inversed sheath was a distinct possibility at the anode of a PPT[28]. Being able to model an inversed anode sheath would thereby present benefits for PPT research as well. Secondly, energy transfer equations will be needed to simulate the cooling effects that were discussed in Campenell's work[20].

## 7.4 Discussion

The importance of geometry depends on the aspects being modelled. For example, magnetic geometry is relevant when investigating the sputtering and redeposition of tungsten atoms in the divertor. The Chodura sheath caused by the low magnetic field line angle affects the ionization paths of Tungsten atoms [92]. On the other hand, when investigation is only focused on the average heat and ion flux to the divertor plate, a one dimensional simulation may suffice. To this end, Magnum PSI is able to emulate the heat and particle flux levels within the divertor[39] even though it is a linear accelerator with a magnetic field perpendicular to the target surface[18]. The choice of dimensions depends on the direction of gradients that are considered. Whereby the gradient electron density is perpendicular to the divertor plate[19]. In the current work, the density gradient was also considered to be perpendicular to the electrode as the plasma slab was assumed to be homogeneous in other dimensions. This assumption renders reasonable performance predictions[1][38]. However, if one is investigating the canting effect, the density gradient parallel to the electrode surface also needs to be considered[47].

In the long term vision of the PROMETEO project, a multi thruster simulation platform is envisioned. Mesh-grids representing different magnetic geometries could be generated and used in the platform. The build up of such a platform would need to be modular. The model in the current project can prove module to determine the electron emission fluxes. Calculating the emission fluxes and the plasma properties in the mesh-grid should be done in a sequential manner due to the non-linear nature[14]. Expanding the code to allow inversed sheaths further broadens its applicability.

# 8 Conclusions and Recommendations

## 8.1 Conclusions

The primary research question of this thesis was:

**What are the dominant physical mechanisms in the plasma discharge?**

The physical processes that were investigated in particular were the self-inducing magnetic field, particle collisions, and the different electron mechanisms (SEE, TEE and FEE). It was shown in sections 5.1 and 5.4 that a proper calculation of the magnetic field is needed to give realist results for current density as the self-induced magnetic field acts as an inductive load. The resistive load is almost entirely dependant on ion-electron collisions (section 4.1). The presence of neutrals has a negligible influence on plasma resistivity. Ion-electron collisions cause far more friction than electron neutral collisions due to long ranging coulomb forces. Only when the ionization degree was lower than 0.001 did the collision rate by neutrals become of similar order to ion-electron friction. In section 3.4.2 it was shown that the FEE are negligible for the conditions in expected in the PPT.

The role that SEE and TEE play in current are somewhat complex and nuanced. From literature (section 1.4.2), it is known that the PPT arc discharge is categorized as a thermal arc discharge, and hence TEE must dominate over SEE. Based on the validation results (section 5), the cathode wall temperature has to surpass a temperature of 3000 K or cathode spots form to allow thermionic electron emissions to dominate over sheath electron emissions. For materials that have a boiling point lower than 3000 K, the dominant mechanism of electron emissions is expected to be cathode spots. Whereby small spots of evaporating material on cathode provide thermionic electrons to the plasma discharge.

Section 6.2 revealed that TEE is not the largest contributor to current. The flux of electrons diffusing from the bulk plasma to the electrodes is larger than TEE. However TEE still plays a crucial role in the current voltage characteristic. Higher thermionic emissions allows for a lower sheath potential drop at the cathode. The cathode sheath then takes up less of the applied voltage, eventually allowing for higher current levels. If TEE was not sufficiently high, the current level would fail to increase with voltage beyond a certain point. As a result of the dominant role of thermionic emissions, the model is highly sensitive to the cathode wall temperature. This relationship is highly non-linear. The model was only able to resolve for certain ranges of assumed cathode wall temperature. Hence the cathode wall temperature may not necessarily be an independent variable as was assumed in this model. It should be clear however that the cathode temperature is a function of the current density and not vice versa, as demonstrated in sections 5.5, 5.4 and 6.

The sheath potential drop also played a significant role in the analyses of electron temperature and electron density (section6.1. Increasing the electron temperature decreases plasma resistivity and hence increases the current density. Increasing the plasma density also increases the current up to a certain limit as seen in figure 36. This is because at lower resistance levels, most of the externally applied current is taken up by the plasma sheath. At increased density levels, the resistivity and thus the electron current increase. This goes on until all of the bulk plasma drop is taken up by resistance.

In section 6.3 it was shown that increasing the distance between electrodes, increases the slope of the current potential characteristic. Due to the assumptions made in this model (homogeneous plasma), the bulk electric field increases relative to the plasma resistivity. The electric field in the bulk is defined by the ratio of the plasma voltage to the electrode distance, in the current model.

In section 5.6, it was noted that the model showed better correspondence to data experiments performed with propellants that have a low atomic weight. This is due to the canting effect where by the plasma sheet looses orthogonality with the electrodes. This is accompanied by a difference in electron density near the regions near the anode and the cathode. The various phenomena that cause canting are thus relevant for better simulating PPTs with higher atomic mass propellants.

In section 7, synergy with fusion research was explored:

**Which crossover applications do PPT modelling and Fusion have?**

It was evident that the divertor region was the part of the fusion reactor that was most similar to PPT conditions in terms of electron temperature and electron density. The plasma in a fusion reactor is strongly magnetized in contrast to the PPT reactor. But this doesn't necessarily need to an issue. Depending on the research question, certain aspects of plasma and magnetic geometry can be neglected. This is evidenced by Magnum PSI, which has a magnetic field that is perpendicular to the target surface, but is able to emulate the high heat fluxes of a divertor region. The most interesting research synergy investigated was strongly emitting divertor surfaces. Such surfaces could mitigate heat loads to the divertor. To investigate such sheaths, the model in this project needs to be amended to allow inverse sheath mode and include heat balance equations.

## 8.2 Recommendations

This project can be seen as an initial exploration of the arc discharge properties of a PPT. The results of this project have mapped out electrical current density for a certain parameter space of electron density, temperature and potential drop. At times it appeared that certain regions of the parameter space are mathematically forbidden as the solver would not resolve for certain combinations of input parameters.The highly non-linear nature of the equations involved was a salient issue for this code. While a work around was developed (discussed in section 5.4.1) it was not sufficient to provide a wide range of stable solutions. Future iterations of this project need to develop an iterative solution scheme that converges within expected ranges.

The results have also indicated that certain combinations of input parameters are strongly related. To give a more complete picture of these relationships it would be necessary to expand the model to include ablation models, thermal energy balance equations and ionization equilibrium models to predict. Ablation models would provide information on the initial density and temperature of the in flowing plasma. While ionization equilibrium models can provide the ratio between the different species densities (ion, electron and neutrals) for different electron temperatures.

When it comes to the sheath model, a few additions to the model can be made to improve emulation of literature data. For one, arc discharges generally have an inverted anode potential fall. In other words the potential at the anode sheath edge $V_B$ is lower than the externally applied anode potential $V_A$. This also means that the ion flux towards the anode is largely repulsed by the inverted sheath. This decreases the sheath electron emissions as well as cathode heating, which in turn decreases the thermal electron emissions. Before a sheath transitions into inversed mode, it can also pass by space charge limited mode. The three types of sheath modes (classical, SCL and inversed) can be seen in figure 6. A future iteration of the transverse model should allow for the possibility of a SCL and or inversed sheath. It would be interesting to see how the transition to such modes affect the analyses. The inclusion of alternative sheath modes in combination with energy balance equation into the model would also benefit fusion research. As such alternative sheath modes are being investigated as a way to cool the plasma in the divertor region and mitigate ion bombardment.

### 8.2.1 Cathode Spots and Erosion

Finally another effect that wasn't yet take into account was the release of heavy particles from the electrode, due to ion impact or cathode spots. Upon release, these heavy particles absorb thermal energy from the plasma. This could potentially decrease the overall efficiency of the thruster. Energy balance equations in the bulk plasma can help estimate the effect of these impurities on the plasma thermal energy. To prevent cathode erosion, it could be beneficial to use a tungsten cathode instead of copper, as tungsten melts at a higher temperature (listed in table 9). A comparison with a spot emissions model would be needed to investigate which material releases more electrons. One can use an empirical spot formation model for copper, as utilized by Shaw [28]. Experimentally it had been measured that the current per observed spot is between 80 and 220 A and their radius to be approximately 1-2 mm. The evaporating material from these spots would ionize and contribute to the propellant[28]. The current density within the spot is thus in the range of range of $10^6 - 10^8 A/m^2$.

### 8.2.2 Thermal Balance Equations

In sections 4, 6 and 7, it became evident that thermal balance equations are necessary. These would allow the prediction of the electron temperature evolution during the discharge. It should include a coupling to the electrode wall temperature. A thermal element model could be implemented to predict the wall temperatures. The cathode temperature should be considered a free variable instead of a user defined input. A better estimate of the cathode temperature would thus improve the prediction of thermionic emissions. The energy exchange between the cathode wall through emissions and particle absorption could possibly affect the sheath potential and bulk plasma temperature. Hence one could better estimate the sheath potential.

One example of a heat balance equation is the heat flux balance a the cathode surface. Javidi Shirvan does this by equating the energy flux from the cathode sheath towards the cathode surface ($q^{s \rightarrow c}$) and the energy flux from the cathode surface towards the sheath[79]:

$$q^{s \rightarrow c} = -q^{em}_{rad} + q^{re}_{rad} + q_i + q_{bd} - q_{TEE} - q_{SEE} \tag{126}$$

The first term is the radiation heat flux emitted by the cathode surface ($q^{em}_{rad}$) through gray body radiation while the second term is the radiation heat flux received by the cathode from the plasma ($q^{re}_{rad}$). These were deemed negligible in previous studies by Javidi[13] and Edamitsu[63]. The energy brought to the cathode surface by the incident sheath ions $q_i$ is the following[12]:

$$q_i = g_i\big(\frac{1}{2}ZK_bT_e^{p/ps} + eZV_c + E_i - ZeW_{eff}\big) \tag{127}$$

where the first term represents the kinetic energy of one ion moving at thermal speed towards the cathode. $Z$ is the ion charge and $T_e^{p/ps}$ is the electron temperature at the pre-sheath/sheath boundary. The second term is the electrostatic acceleration an ion experiences due to potential drop $V_C$ in the sheath region. The third term is the average energy of ion recombination at the cathode surface $E_i$. The final term is the energy required to release electrons from the surface, where $W_{eff}$ is the effective work function after taking the Schottky correction ($\Delta W$) into account[12]:

$$W_{eff} = W - \Delta W = W - \sqrt{e^3E_{w,C}/(4\pi\varepsilon_0)} \qquad [J] \tag{128}$$

The emission and back-diffusion flux are respectively:

$$-q_{TEE} - q_{SEE} = -(g_{TEE} + g_{SEE})(W_{eff} + 2K_BT_{w,C}) \tag{129}$$

$$q_{bd} = g_{bd}(W_{eff} + 2K_BT^{p/ps}) \tag{130}$$

The emissions heat fluxes are a heat loss mechanism for the cathode while the back diffusion flux is a heat gain mechanism. The emissions have the same temperature as the cathode surface while the electrons diffusing back through the sheath have the temperature of the plasma to plasma sheath boundary (which is higher than the wall temperature). The quantities in these equations and their position are described the diagram of figure 28. In a similar fashion a heat balance equation can be drawn up between the pre-sheath and sheath layers, or between the pre-sheath and the plasma bulk. Furthermore the temperature within the bulk is not necessarily homogeneous and finite elements methods can be used to calculate the temperature at various points within the plasma. All in all these equations demonstrated how the different temperatures ($T_{w,C}$ and $T_e$) interact through convection terms.

# References


[1] R. L. Burton and P. J. Turchi, "Pulsed plasma thruster," *Journal of Propulsion and Power*, vol. 14, no. 5, pp. 716–735, 1998.

[2] S. Mazouffre, "Electric propulsion for satellites and spacecraft: established technologies and novel approaches," *Plasma Sources Science and Technology*, vol. 25, p. 033002, 6 2016.

[3] J. K. Ziemer and E. Y. Choueiri, "Scaling laws for electromagnetic pulsed plasma thrusters," *Plasma Sources Science and Technology*, vol. 10, no. 3, pp. 395–405, 2001.

[4] M. Lau, S. Manna, G. Herdrich, T. Schönherr, and K. Komurasaki, "Investigation of the plasma current density of a pulsed plasma thruster," in *Journal of Propulsion and Power*, vol. 30, pp. 1459–'1470, American Institute of Aeronautics and Astronautics Inc., 11 2014.

[5] M. A. Lieberman and A. J. Lichtenberg, *Principles of Plasma Discharges and Materials Processing*. Hoboken, New Jersey: Wiley, 2 ed., 2005.

[6] R. J. Roth, *Industrial plasma engineering vol 1*, vol. 1. Institute of Physics Publishing, 1995.

[7] M. D. Campanell, "Alternative model of space-charge-limited thermionic current flow through a plasma," *Physical Review E*, vol. 97, 4 2018.

[8] J. P. Freidberg, *Plasma Physics and Fusion Energy*. New York: Cambridge University Press, 2007.

[9] R. G. Jahn, *Physics of Electric Propulsion*. MacGraw Hill, 1968.

[10] F. Guarducci, F. Graziani, and G. Paccani, *Design and Testing of a Micro PPT for Cubesat Applications*. PhD thesis, Sapienza Universita di Roma, 2007.

[11] P. G. Mikellides and P. J. Turchi, "Modeling of late-time ablation in teflon pulsed plasma thrusters," in *32nd Joint Propulsion Conference and Exhibit*, American Institute of Aeronautics and Astronautics Inc, AIAA, 1996.

[12] A. Javidi Shirvan, I. Choquet, H. Nilsson, and H. Jasak, "Coupling boundary condition for high-intensity electric arc attached on a non-homogeneous refractory cathode," *Computer Physics Communications*, vol. 222, pp. 31–45, 1 2018.

[13] A. Javidi Shirvan, *Modelling of cathode-plasma interaction in short high-intensity electric arc Application to Gas Tungsten Arc Welding*. PhD thesis, Chalmers University of Technology, Gothenburg, Sweden, 2016.

[14] A. Javidi Shirvan, *Modelling of Electric Arc Welding: arc-electrode coupling*. PhD thesis, Chalmers University of Technology, Gothenburg, Sweden, 2013.

[15] M. S. Benilov, L. G. Benilova, H. P. Li, and G. Q. Wu, "Sheath and arc-column voltages in high-pressure arc discharges," *Journal of Physics D: Applied Physics*, vol. 45, 9 2012.

[16] T. E. Markusic, *Current Sheet Canting in Pulsed Electromagnetic Accelerators*. PhD thesis, Princeton University, 2002.

[17] T. Schönherr, K. Komurasaki, and G. Herdrich, "Propellant utilization efficiency in a pulsed plasma thruster," *Journal of Propulsion and Power*, vol. 29, pp. 1478–1487, 11 2013.

[18] K. S. C. Peereboom, *Modeling of Magnetized Expanding Plasmas*. PhD thesis, Eindhoven University of Technology, 2012.

[19] D. L. Holland, B. D. Fried, and G. J. Morales, "Sheath structure in a magnetized plasma," *Physics of Fluids B: Plasma Physics*, vol. 5, p. 1723, 1993.

[20] M. D. Campanell, "Possible mitigation of tokamak plasma-surface interactions using thermionic divertor plates with inverse sheaths," *Physics of Plasmas*, vol. 27, 4 2020.

[21] A. Anders, *Cathodic Arcs*, vol. 50 of *Springer Series on Atomic, Optical, and Plasma Physics*. New York, NY: Springer New York, 2008.

[22] A. Javidi Shirvan and I. Choquet, "A review of cathode-arc coupling modeling in GTAW," *Welding in the World*, vol. 60, pp. 821–835, 7 2016.

[23] J. R. Wertz and W. J. Larson, *Space mission analysis and design*. Microcosm, 1999.

[24] E. Ahedo, "Plasmas for space propulsion," *Plasma Physics and Controlled Fusion*, vol. 53, 12 2011.

[25] M. Andrenucci, R. Blockley, and W. W. Shyy, *Encyclopedia of aerospace engineering*. Wiley, 2010.

[26] M. Martinez-Sanchez and J. E. Pollard, "Spacecraft Electric Propulsion-An Overview," *Journal of Propulsion and Power*, vol. 14, no. 5.

[27] A. Nawaz, M. Lau, G. Herdrich, and M. Auweter-Kurtz, "Investigation of the Magnetic Field in a Pulsed Plasma Thruster," *AIAA Journal*, vol. 46, pp. 2881–2889, 11 2008.

[28] P. Vallis Shaw, "Pulsed Plasma Thrusters for Small Satellites," tech. rep., University of Surrey, 2011.

[29] E. M. Henrikson and P. G. Mikellides, "Modeling of Ablation-Fed Pulsed Plasma Thruster Operation Using a New Approach to the Ablation Process," in *44th AIAA/ASME/SAE/ASEE Joint Propulsion Conference & Exhibit*, 2008.

[30] M. G. Cho and H. G. Sung, "Numerical Modeling of Pulsed Plasma Thruster Performance with Teflon Ablation and Ionization," *International Journal of Aeronautical and Space Sciences*, vol. 20, pp. 415–422, 6 2019.

[31] J. Neudorfer, T. Stindl, R. Schneider, S. Roller, C.-D. Munz, and M. Auweter-Kurtz, "Three-dimensional Particle-In-Cell Simulation of a Pulsed Plasma Thruster: Modeling and Challenges," in *32nd International Electric Propulsion Conference*, 2011.

[32] S. Barquero, M. Merino, and J. N. Cavalí, "Design of an Experimental Ablative Pulsed Plasma Thruster for Micropropulsion," in *Space Propulsion Conference*, (Paris, France), Association Aéronautique et Astronautique de France, 2021.

[33] P. G. Mikellides, P. J. Turchi, and N. F. Roderick, "Applied-field magnetoplasmadynamic thrusters, Part 1: numerical simulations using the MACH2 code," *Journal of Propulsion and Power*, vol. 16, no. 5, pp. 887–893, 2000.

[34] J. Heiermann and M. Auweter-Kurtz, "Numerical Simulation of High Power Steady State MPD Thrusters," in *27th International Electric Propulsion Conference*, 2001.

[35] J. Li, Y. Zhang, J. Wu, Y. Cheng, and X. Du, "Particle simulation model for self-field magnetoplasmadynamic thruster," *Energies*, vol. 12, 4 2019.

[36] C. M. Xisto, J. C. Páscoa, and P. J. Oliveira, "Numerical analysis of real gas MHD flow on two-dimensional self-field MPD thrusters," *Acta Astronautica*, vol. 112, pp. 89–101, 7 2015.

[37] Q. Liu, L. Yang, Y. Huang, X. Zhao, and Z. Zheng, "PIC simulation of plasma properties in the discharge channel of a pulsed plasma thruster with flared electrodes," *Plasma Science and Technology*, vol. 21, 4 2019.

[38] P. G. Mikellides, E. M. Henrikson, and S. S. Rajagopalan, "Theoretical formulation for the performance of rectangular, breech-fed pulsed plasma thrusters," *Journal of Propulsion and Power*, vol. 35, no. 4, pp. 811–818, 2019.

[39] G. De Temmerman, M. A. Van Den Berg, J. Scholten, A. Lof, H. J. Van Der Meiden, H. J. Van Eck, T. W. Morgan, T. M. De Kruijf, P. A. Zeijlmans Van Emmichoven, and J. J. Zielinski, "High heat flux capabilities of the Magnum-PSI linear plasma device," *Fusion Engineering and Design*, vol. 88, no. 6-8, pp. 483–487, 2013.

[40] "PROMETEO project," 2018.

[41] H. Koizumi, R. Noji, K. Komurasaki, and Y. Arakawa, "Plasma acceleration processes in an ablative pulsed plasma thruster," *Physics of Plasmas*, vol. 14, no. 3, 2007.

[42] T. Schönherr, F. Nees, Y. Arakawa, K. Komurasaki, and G. Herdrich, "Characteristics of plasma properties in an ablative pulsed plasma thruster," *Physics of Plasmas*, vol. 20, 3 2013.

[43] E. J. Pencil, H. Kamhawi, L. A. Arrington, and W. Blaise Warren, "Evaluation of Alternate Propellants for Pulsed Plasma Thrusters," in *27th International Electric Propulsion Conference*, 2001.

[44] J. K. Ziemer, E. Y. Choueiri, and D. Birx, "Comparing the Performance of Co-Axial and Parallel-Plate Gas-Fed PPTs," in *26th International Electric Propulsion Conference*, (Kitakyushu, Japan), 1999.

[45] A. Rezaeiha and T. Schönherr, "Analysis of effective parameters on ablative PPT performance," *Aircraft Engineering and Aerospace Technology*, vol. 84, no. 4, pp. 231–243, 2012.

[46] Y. S. le Grand, "Literature Review: Modelling the Plasma ow in Pulsed Plasma Thrusters and Magnetoplasmadynamic Thrusters," tech. rep., TU Delft, 2020.

[47] E. Choueiri, T. Markusic, J. Berkery, and J. Cooley, "Physics and Dynamics of Current Sheets in Pulsed Plasma Thrusters Final report to the US Air Force Office of Scientific Research," tech. rep., Electric Propulsion and Plasma Dynamics Laboratory, Princeton, 2001.

[48] A. Nawaz, R. Albertoni, and M. Auweter-Kurtz, "Thrust efficiency optimization of the pulsed plasma thruster SIMP-LEX," *Acta Astronautica*, vol. 67, pp. 440–448, 8 2010.

[49] Y. Zhou, N. Wang, X. Liu, W. Y. L. Ling, K. Xie, and Z. Wu, "Experimental investigation on the evolution of plasma properties in the discharge channel of a pulsed plasma thruster," *Plasma Science and Technology*, vol. 22, p. 065504, 4 2020.

[50] Z. Zhang, W. Yeong, L. Ling, J. Ren, H. Tang, J. Cao, X. Lin, and T. M. York, "The plasma morphology of an asymmetric electrode ablative pulsed plasma thruster," *Plasma Sources Sci. Technol*, vol. 28, p. 25008, 2019.

[51] T. E. Markusic and E. Y. Choueiri, "Visualization of Current Sheet Canting in a Pulsed Plasma Accelerator," in *26th International Electric Propulsion Conference*, 1999.

[52] A. Fridman and L. Kennedy, *Plasma Physics and Engineering*. Boca Raton, Florida: CRC Press, 2nd ed., 2011.

[53] T. E. Markusic, E. Y. Choueiri, and J. W. Berkery, "Measurements of current sheet canting in a pulsed electromagnetic accelerator," *Physics of Plasmas*, vol. 11, pp. 4847–4858, 10 2004.

[54] T. E. Markusic and E. Y. Choueiri, "Phenomenological Model of Current Sheet Canting in Pulsed Electromagnetic Accelerators," in *28th International Electectric Propulsion Conference*, (Toulouse France), 2003.

[55] J. Westerhout, W. R. Koppers, W. A. Vijvers, R. S. Al, S. Brezinsek, S. Brons, H. J. Van Eck, R. Engeln, B. De Groot, R. Koch, H. J. Van Der Meiden, M. P. Nuijten, V. Philipps, M. J. Van De Pol, P. R. Prins, U. Samm, J. Scholten, D. C. Schram, B. Schweer, P. H. Smeets, D. G. Whyte, E. Zoethout, A. W. Kleyn, W. J. Goedheer, N. J. Cardozo, and G. J. Van Rooij, "PSI research in the ITER divertor parameter range at the FOM PSI-lab," in *Physica Scripta T*, vol. T128, pp. 18–22, 2007.

[56] A. W. Leonard, "Plasma Physics and Controlled Fusion Plasma detachment in divertor tokamaks Recent citations Plasma detachment in divertor tokamaks," *Plasma Phys. Control. Fusion*, vol. 60, p. 44001, 2018.

[57] M. Coletti, F. Guarducci, and S. B. Gabriel, "A micro PPT for Cubesat application: Design and preliminary experimental results," *Acta Astronautica*, vol. 69, pp. 200–208, 8 2011.

[58] M. J. Zucrow and J. D. Hoffman, *Gas Dynamics Volume 1*. Wiley, 1976.

[59] A. Solbes and R. J. Vondra, "Performance Study of a Solid Fuel-Pulsed Electric Microthruster," *Journal of Spacecrafts and Rockets*, vol. 10, pp. 406–410, 5 1973.

[60] D. J. Palumbo and W. J. Guman, "Effects of propellant and electrode geometry on pulsed ablative plasma thruster performance," *Journal of Spacecraft and Rockets*, vol. 13, no. 3, pp. 163–167, 1976.

[61] S. J. Pottinger and C. A. Scharlemann, "Micro Pulsed Plasma Thruster Development," in *International Electric Propulsion Conference*, 2007.

[62] M. Keidar, I. D. Boyd, and I. I. Beilis, "Model of an electrothermal pulsed plasma thruster," *Journal of Propulsion and Power*, vol. 19, no. 3, pp. 424–430, 2003.

[63] T. Edamitsu and H. Tahara, "Performance Measurement and Flowfield Calculation of an Electrothermal Pulsed Plasma Thruster with a Propellant Feeding Mechanism," in *IEPC*, (Princeton University), 2005.

[64] "Solve system of nonlinear equations - MATLAB fsolve - MathWorks Benelux."

[65] J. D. Huba, *NRL PLASMA FORMULARY Supported by The Office of Naval Research*. Washington, DC: Naval Research Laboratory, 2016.

[66] G. D. Hobbs and J. A. Wesson, "Heat flow through a Langmuir sheath in the presence of electron emission," *Plasma Physics*, vol. 9, no. 1, pp. 85–87, 1967.

[67] J. P. Sheehan, I. D. Kaganovich, H. Wang, D. Sydorenko, Y. Raitses, and N. Hershkowitz, "Effects of emitted electron temperature on the plasma sheath," *Physics of Plasmas*, vol. 21, p. 063502, 6 2014.

[68] O. Richardson, "On the negative radiation from hot platinum," *Proceedings of the Cambridge Philosophical Society*, vol. 11, no. May, pp. 286–295, 1902.

[69] C. R. Crowell, "The Richardson constant for thermionic emission in Schottky barrier diodes," *Solid State Electronics*, vol. 8, pp. 395–399, 4 1965.

[70] S. Lichtenberg, L. Dabringhausen, O. Langenscheidt, and J. Mentel, "The plasma boundary layer of HID-cathodes: Modelling and numerical results," *Journal of Physics D: Applied Physics*, vol. 38, pp. 3112–3127, 9 2005.

[71] R. G. Forbes, "Physics of generalized Fowler-Nordheim-type equations," *Journal of Vacuum Science & Technology B: Microelectronics and Nanometer Structures*, vol. 26, p. 788, 4 2008.

[72] R. G. Forbes, "Simple good approximations for the special elliptic functions in standard Fowler-Nordheim tunneling theory for a Schottky-Nordheim barrier," *Applied Physics Letters*, vol. 89, p. 113122, 9 2006.

[73] R. J. Goldston and P. H. P. H. Rutherford, *Introduction to plasma physics*. Institute of Physics Pub, 1995.

[74] W. Fundamenski and O. E. Garcia, "Comparison of Coulomb Collision Rates in the Plasma Physics and Magnetically Confined Fusion Literature," tech. rep., European Fusion Development Agency, 2007.

[75] W. L. Oberkampf and T. G. Trucano, "Verification and validation in computational fluid dynamics," tech. rep., 2002.

[76] L. Swanson and G. Schwind, *Handbook of Charged Particle Optics.* Boca Raton: CRC Press, second ed., 2009.

[77] E. L. Murphy and R. H. Good, "Thermionic Emission, Field Emission, and the Transition Region," *Physical Review*, vol. 102, pp. 1464–1473, 6 1956.

[78] K.-U. Riemann, "The Bohm criterion and sheath 1 formation," *J. Phys. D: Appl. Phys*, vol. 24, pp. 492–518, 1991.

[79] A. Javidi Shirvan, I. Choquet, and H. Nilsson, "Effect of cathode model on arc attachment for short high-intensity arc on a refractory cathode," *Journal of Physics D: Applied Physics*, vol. 49, p. 485201, 11 2016.

[80] L. Sansonnens, J. Haidar, and J. J. Lowke, "Prediction of properties of free burning arcs including effects of ambipolar diffusion," *Journal of Physics D: Applied Physics*, vol. 33, pp. 148–157, 1 2000.

[81] M. Baeva, M. S. Benilov, N. A. Almeida, and D. Uhrlandt, "Novel non-equilibrium modelling of a DC electric arc in argon," *Journal of Physics D: Applied Physics*, vol. 49, p. 245205, 5 2016.

[82] J. Haider and A. J. Farmer, "Temperature measurements for high-current free-burning arcs in nitrogen," *Journal of Physics D: Applied Physics*, vol. 26, pp. 1224–1229, 8 1993.

[83] T. Schönherr, A. Nawaz, G. Herdrich, H.-P. Röser, and M. Auweter-Kurtz, "Influence of Electrode Shape on Performance of Pulsed Magnetoplasmadynamic Thruster SIMP-LEX," *Journal of Propulsion and Power*, 2008.

[84] L. Yang, Y. Huang, H. Tang, and X. Liu, "Ablation and Ionization Phenomenon in a Teflon Pulsed Plasma Thruster," in *30th International Electric Propulsion Conference*, 2015.

[85] T. Schönherr, K. Komurasaki, R. Kawashima, Y. Arakawa, and G. Herdrich, "Evaluation of discharge behavior of the pulsed plasma thruster SIMP-LEX AIAA 2010-6530,"

[86] R. Chodura, "Plasma–wall transition in an oblique magnetic field," *The Physics of Fluids*, vol. 25, p. 1628, 6 1998.

[87] D. Coulette and G. Manfredi, "Kinetic simulations of the Chodura and Debye sheaths for magnetic fields with grazing incidence," *Plasma Physics and Controlled Fusion*, vol. 58, p. 025008, 1 2016.

[88] R. Albertoni, F. Paganucci, and M. Andrenucci, "A phenomenological performance model for applied-field MPD thrusters," *Acta Astronautica*, vol. 107, pp. 177–186, 2015.

[89] M. D. Campanell and M. V. Umansky, "Strongly Emitting Surfaces Unable to Float below Plasma Potential," *Physical Review Letters*, vol. 116, 2 2016.

[90] R. A. Pitts, X. Bonnin, F. Escourbiac, H. Frerichs, J. P. Gunn, T. Hirai, A. S. Kukushkin, E. Kaveeva, M. A. Miller, D. Moulton, V. Rozhansky, I. Senichenkov, E. Sytova, O. Schmitz, P. C. Stangeby, G. De Temmerman, I. Veselova, and S. Wiesen, "Physics basis for the first ITER tungsten divertor," *Nuclear Materials and Energy*, vol. 20, p. 100696, 8 2019.

[91] A. Perek, T. Ravensbergen, M. van Berkel, C. Galperti, B. P. Duval, O. Février, R. J. van Kampen, F. Felici, J. T. Lammers, C. Theiler, J. Schoukens, B. Linehan, M. Komm, S. Henderson, D. Brida, and M. R. de Baar, "Real-time feedback control of the impurity emission front in tokamak divertor plasmas," *Nature Communications 2021 12:1*, vol. 12, pp. 1–9, 2 2021.

[92] J. Guterl, C. Johnson, D. Ennis, S. Loche, and P. Snyder, "Effects of the Chodura sheath on tungsten ionization and emission in tokamak divertors," *Contributions to Plasma Physics*, vol. 60, p. e201900140, 6 2020.

# A Appendix: Verification

This section discusses portions of the verification process that were relatively trivial compared to the matter discussed in the report. Verification in the context of sub-functions refers to checking whether the functions implemented in the Matlab model display the behavior one would expect from a physics perspective. This entails plotting functions and comparing them with literature examples. Another possibility is to plot several curves for different inputs and inspect whether the output behaves as expected.

This section discusses the verification of the sub functions for; the plasma electron wall flux flux to equation and the secondary electron emissions, implemented in the Matlab code of this model. These equations are relatively trivial because they are either linear or simple exponential equations.

## A.1 Boltzmann Electron Wall Flux

The electron flux at the wall ($g_e$) is calculated using the Boltzmann relation[5, p. 168, 172]:

$$g_e = n_{e0}\sqrt{\frac{\hat{T}_e}{2\pi m_e}}\exp\left(\frac{-eV}{\hat{T}_e}\right) \tag{131}$$

where $n_{e0}$ is the electron density at the plasma sheath edge, $\hat{T}_e$ is the electron temperature in J, $e$ is the elementary charge in coulomb and $m_e$ is the electron mass in kg. The absolute value of the potential drop is noted as $V$. In the model used in this paper it is assumed that both sheaths are classical. In other words the electric potential at the conducting wall is lower than the plasma bulk because of the ambipolar field at the wall.[21] Hence a minus is placed in front of the $V$ term here. In this section "increasing $V$" refers to the magnitude of the absolute value of the potential drop.

To verify the proper implementation of this function in Matlab, the function is plotted for a range of electron temperatures and density to asses if the characteristic curves meets expectations. Two such expectations are that the equation will exponentially decrease for increasing V. For different densities at fixed temperature these values converge faster (fig. 49a) than for different temperatures at a fixed density (fig. 49b).

To further verify the equation, one can investigate if the numerical derivative behaves according to the analytical derivative. The derivative of this equation with respect to V is:

$$g_e = n_{e0}\frac{-e}{\sqrt{\hat{T}_e 2\pi m_e}}\exp\left(\frac{-eV}{\hat{T}_e}\right) \tag{132}$$

In the case of the derivative it decreases linearly with $ne_0$. For $V = 0$ it will be smaller for higher temperatures. For larger values of $V$, the lower temperatures have a smaller derivatives. These predictions are confirmed by plots in figures 49d and 49c, hence this function has been properly implemented in the Matlab code.

[21] At initial contact of a plasma with a conducting wall, electrons diffuse at a larger rate than ions due to their lower mass. A negative space charge develops which repulses a portion of further incoming electrons. This is called the ambipolar field[5].

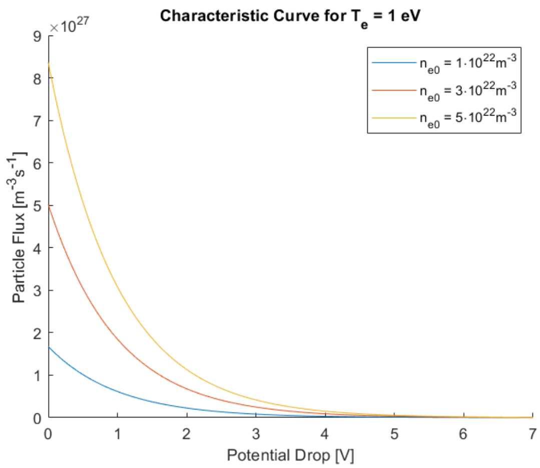


(a) The flux increases linearly for density and decreases exponentially with potential

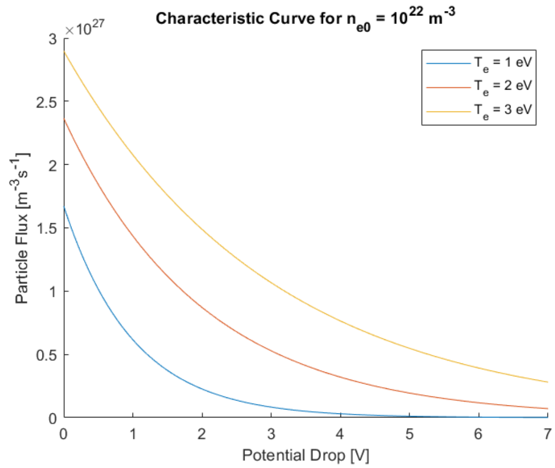


(b) The flux increases with the square root of temperature and decreases exponentially with potential

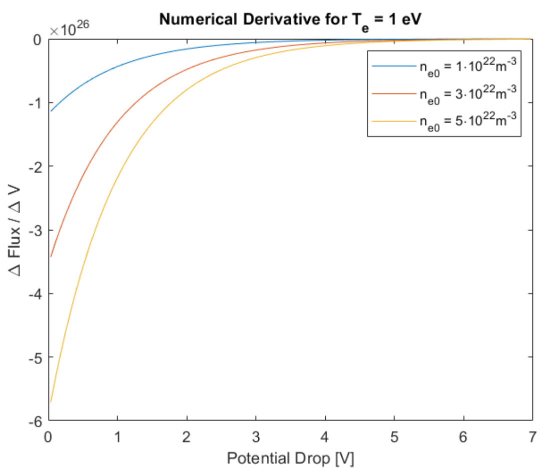


(c) A first order numerical differentiation of the flux-potential curve for different densities.

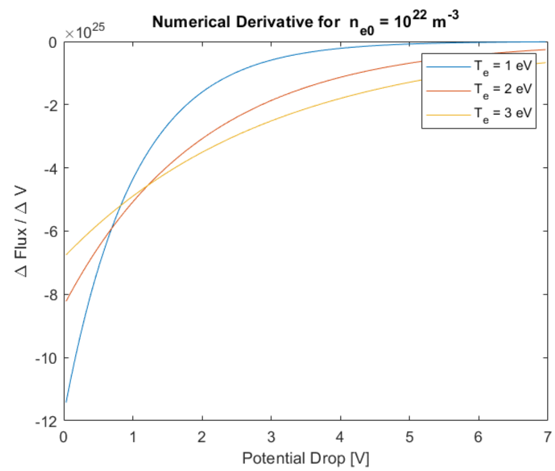


(d) A first order numerical differentiation of the flux-potential curve for different densities.

Figure 49: Boltzmann verification tests

## A.2 Secondary Electron Emissions

Ions striking the electron wall can nudge out electron, this secondary electron emissions flux (SEE) is determined by multiplying the incident ion flux $g_i$ with $\gamma_{se}$:

$$SEE = \gamma_{se} g_i \approx 0.016(\mathcal{E}_i - 2W) n_{i0} \sqrt{\hat{T}e/m_i} \tag{133}$$

Where $\mathcal{E}_i$ is the ionization energy, $W$ the work function of the material, $m_i$ the ion ion mass and $n_{i0}$ is the ion density at sheath edge.

$\gamma_{se}$ is semi-empirical parameter valid for ions of a lower impact energy than 1 KeV.

$$\gamma = 0.016(I - 2W) \tag{134}$$

For an Ar+ discharge, the experimental $\gamma_{SEE}$ for a tungsten surface is approximately 0.1[52, p. 514]. Given that the ionisation energy of Argon is 15.76 eV and the work function of tungsten is 4.5 eV, a $\gamma \approx 0.11$ is estimated by sub-function in Matlab.

$\mathcal{E}_i$, $W$ and $m_i$ are essentially fixed by the choice electrode materials and propellant. SEE is linear in proportion to density for a certain electron temperature. This can be seen in figure 50.

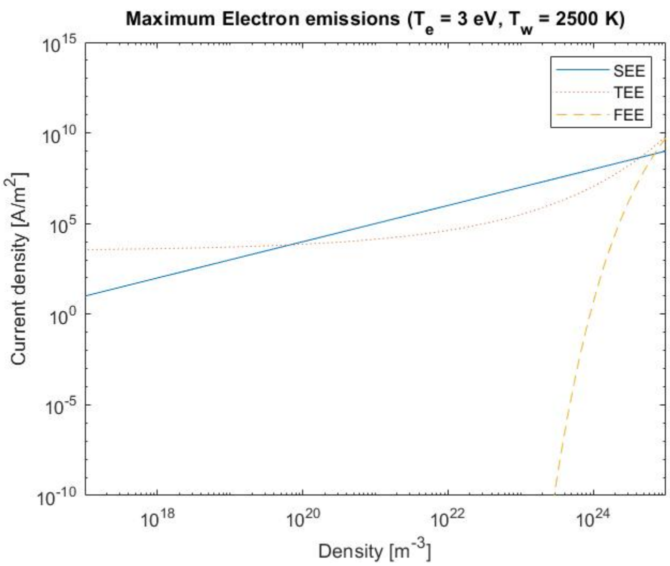


Figure 50: Comparisons of emissions of copper surface adjacent to an hydrogen plasma. SEE represents secondary electron Emissions while TEE and FEE represent thermionic electron emissions and field electron emissions respectively

# B Appendix: Transverse Model Equations (Long Form)

The original set of equation developped for this model consisted of: a charge continuity equation; particle conservation equation; momentum conservation equation; two sets of equations to determine the electric field and electrode emissions at the anode and cathode.

The independent variables in this system are: the electric fields ($E_{w,C}$,$E_{w,A}$), the sheath potential drop ($V_C$,$V_A$) and electron emissions ($g^\star_{e,C}$,$g^\star_{e,A}$) at the anode and cathodes respectively; and finally the transverse electron velocity $u_{xe}$.

**Electric field at cathode wall**

$$0 = -E_{w,C} + f_1(g^\star_{e,C}, V_C) \tag{135}$$

**Electron emissions at cathode wall**

$$0 = -g^\star_{e,C} + TEE(E_{W,C}) + FEE_C(E_{W,C}) + SEE \tag{136}$$

**Particle Conservation**

$$0 = \frac{g^\star_{e,A} - g_{bolz}(V_A) - g^\star_{e,C} + g_{bolz}(V_C)}{2n_{e0}} - u_{xe} \tag{137}$$

**Charge Continuity**

$$0 = \frac{-g^\star_{e,A} + g_{bolz}(V_A) - g^\star_{e,C} + g_{bolz}(V_C)}{2n_{e0}} - \sqrt{\hat{T}_e/m_i} \tag{138}$$

**Electron emissions at anode wall**

$$0 = -g^\star_{e,A} + TEE(E_{W,A}) + FEE_C(E_{W,A}) + SEE \tag{139}$$

**Electric field at anode wall**

$$0 = -E_{w,A} + f_1(g^\star_{e,A}, V_A) \tag{140}$$

**Momentum Balance**

$$0 = -en_e \frac{\phi_A - V_A - (\phi_C - V_C)}{h} + en_e u_{zi} B_y - u_{xe} m_e n_e v_{th,e}(n_i\sigma_{ei} + n_n\sigma_{en}) \tag{141}$$

## B.1 Extended formulation

$$\begin{gathered} \frac{1}{2}\Big(\frac{d\varphi_{w,C}}{dx}\Big)^2\Big|_{w,C} = \exp(\varphi_{w,C}) - 1 + \frac{g^\star_{e,C}}{n_{e0}c_{e0}}\sqrt{\frac{\hat{T}_w}{\hat{T}_e}}\Big[1 - \Big(1 - 2\frac{\varphi_{w,C}}{\hat{T}_w/\hat{T}_e}\Big)^{1/2}\Big] + M_{i0}^2\Big[\Big(1 - 2\frac{\varphi_{w,C}}{M_{i0}^2}\Big)^{1/2} - 1)\Big] \\ 0 = -E_{w,C} + \sqrt{\frac{n_{e0}\hat{T}_e}{\varepsilon_0}}\frac{d\varphi_{w,C}}{dx}\Big|_w \end{gathered} \tag{142}$$

$$0 = -g^\star_{e,C} + \frac{A_G}{e}T^2_{w,C}\exp\left(-\frac{W - \sqrt{e^3E_{w,C}/(4\pi\varepsilon_0)}}{K_bT_{w,C}}\right) + 0.016(\mathcal{E}_i - 2W)g_i + \frac{e}{4\pi^2\hbar}\frac{1}{W + \mathcal{E}_F}\exp\left(-\frac{4\sqrt{2m_e}W^{3/2}\xi}{3e\hbar E_{w,C}}\right) \tag{143}$$

$$0 = \frac{g^\star_{e,A} - g_{e,A} - g^\star_{e,C} + g_{e,C}}{2n_{e0}} - u_{xe} \tag{144}$$

$$0 = \frac{-g^\star_{e,A} + g_{e,A} - g^\star_{e,C} + g_{e,C}}{2n_{e0}} - \sqrt{\hat{T}_e/m_i} \tag{145}$$

$$0=-g_{e,A}^{\star}+\frac{A_G}{e}T_{w,A}^2\exp\left(-\frac{W-\sqrt{e^3E_{w,A}/(4\pi\varepsilon_0)}}{K_bT_{w,A}}\right)+0.016(\mathcal{E}_i-2W)g_i+\frac{e}{4\pi^2\hbar}\frac{1}{W+\mathcal{E}_F}\exp\left(-\frac{4\sqrt{2m_e}W^{3/2}\xi}{3e\hbar E_{w,A}}\right) \tag{146}$$

$$\frac{1}{2}\Big(\frac{d\varphi_{w,A}}{dx}\Big)^2\Big|_w=\exp(\varphi_{w,A})-1+\frac{g_{e,A}^{\star}}{n_{e0}c_{e0}}\sqrt{\frac{\hat{T_w}}{\hat{T_e}}}\Big[1-\Big(1-2\frac{\varphi_{w,A}}{\hat{T_w}/\hat{T_e}}\Big)^{1/2}\Big]+M_{i0}^2\Big[\Big(1-2\frac{\varphi_{w,A}}{M_{i0}^2}\Big)^{1/2}-1)\Big]$$

$$0=-E_{w,A}+\sqrt{\frac{n_{e0}\hat{T}_e}{\varepsilon_0}}\frac{d\varphi_{w,A}}{dx}\Big|_{w,A} \tag{147}$$

$$0=-en_e\frac{\phi_A-V_A-(\phi_C-V_C)}{h}+en_eu_{zi}B_y-u_{xe}m_en_e^2\Big(\frac{2^{1/2}Ze^4\ln(\Lambda)}{12\pi^{3/2}\varepsilon_0^2m_e^{1/2}\hat{T}_e^{3/2}}+\frac{1-\alpha}{\alpha Z_i}\sqrt{\frac{\hat{T}_e}{m_e}}\cdot 10^{-20}\Big) \tag{148}$$

## B.2 Second iteration:

These equations have been simplified. The effect of electron emissions on the electric field at the wall is negligible.

$$0=-E_{w,C}+f_1(V_C) \tag{149}$$

$$0=-g_{e,C}^{\star}+TEE(E_{W,C})+SEE \tag{150}$$

$$0=\frac{g_{e,A}^{\star}-g_{bolz}(V_A)-g_{e,C}^{\star}+g_{bolz}(V_C)}{2n_{e0}}-u_{xe} \tag{151}$$

$$0=\frac{-g_{e,A}^{\star}+g_{bolz}(V_A)-g_{e,C}^{\star}+g_{bolz}(V_C)}{2n_{e0}}-\sqrt{\hat{T}_e/m_i} \tag{152}$$

$$0=-g_{e,A}^{\star}+TEE(E_{W,A})+SEE \tag{153}$$

$$0=-E_{w,A}+f_1(V_A) \tag{154}$$

$$0=-en_e\frac{\phi_A-V_A-(\phi_C-V_C)}{h}+en_eu_{zi}B_y-u_{xe}m_en_ev_{th,e}(n_i\sigma_{ei}) \tag{155}$$

$$g_{bolz}(V_C)=n_{e0}\sqrt{\frac{\hat{T}_e}{2\pi m_e}}\exp(\varphi_{w,A})=n_{e0}c_e\exp(\varphi_{w,A}) \tag{156}$$

In long form the model can be described as:

$$0 = -E_{w,C} + \sqrt{\frac{2n_{e0}\hat{T}_e}{\varepsilon_0}}\Big[\exp(\varphi_{w,C}) - 1 + M_{i0}^2\big[\Big(1 - 2\frac{\varphi_{w,C}}{M_{i0}^2}\Big)^{1/2} - 1)\big]\Big]^{1/2} \tag{157}$$

$$0 = -g_{e,C}^{\star} + \frac{A_G}{e}T_{w,C}^2 \exp\left(-\frac{W - \sqrt{e^3 E_{w,C}/(4\pi\varepsilon_0)}}{K_b T_{w,C}}\right) + 0.016(\mathcal{E}_i - 2W)g_i \tag{158}$$

$$0 = \frac{g_{e,A}^{\star} - n_{e0}c_e \exp(\varphi_{w,A}) - g_{e,C}^{\star} + n_{e0}c_e \exp(\varphi_{w,C})}{2n_{e0}} - u_{xe} \tag{159}$$

$$0 = \frac{-g_{e,A}^{\star} + n_{e0}c_e \exp(\varphi_{w,A}) - g_{e,C}^{\star} + n_{e0}c_e \exp(\varphi_{w,C})}{2n_{e0}} - \sqrt{\hat{T}_e/m_i} \tag{160}$$

$$0 = -g_{e,A}^{\star} + \frac{A_G}{e}T_{w,A}^2 \exp\left(-\frac{W - \sqrt{e^3 E_{w,A}/(4\pi\varepsilon_0)}}{K_b T_{w,A}}\right) + 0.016(\mathcal{E}_i - 2W)g_i \tag{161}$$

$$0 = -E_{w,A} + \sqrt{\frac{2n_{e0}\hat{T}_e}{\varepsilon_0}}\Big[\exp(\varphi_{w,A}) - 1 + M_{i0}^2\big[\Big(1 - 2\frac{\varphi_{w,A}}{M_{i0}^2}\Big)^{1/2} - 1)\big]\Big]^{1/2} \tag{162}$$

$$0 = -en_e\frac{\phi_A - (\varphi_{w,A}\cdot\hat{T}_e/e) - (\phi_C - (\varphi_{w,C}\cdot\hat{T}_e/e))}{h} + en_e u_{zi}B_y - u_{xe}m_e n_e^2\Big(\frac{2^{1/2}Ze^4\ln(\Lambda)}{12\pi^{3/2}\varepsilon_0^2 m_e^{1/2}\hat{T}_e^{3/2}}\Big) \tag{163}$$